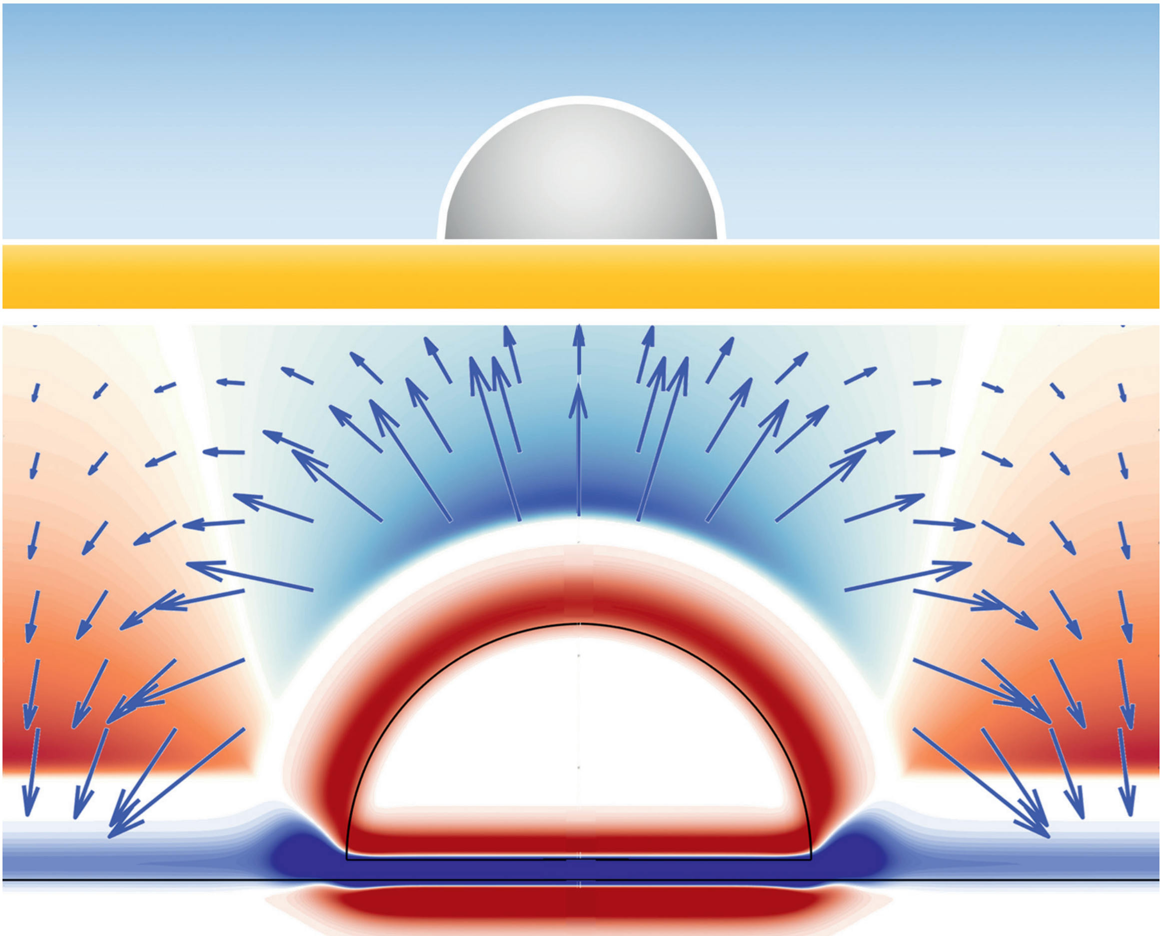

Theory of Electronic and Ionic Perturbations at Supported Electrocatalyst Nanoparticles

Yufan Zhang

Energie & Umwelt / Energy & Environment
Band / Volume 697
ISBN 978-3-95806-896-4

Mitglied der Helmholtz-Gemeinschaft

JÜLICH
Forschungszentrum

Schriften des Forschungszentrums Jülich
Reihe Energie & Umwelt / Energy & Environment Band / Volume 697

Forschungszentrum Jülich GmbH
Institute of Energy Technologies (IET)
Theorie und computergestützte Modellierung von Materialien
in der Energietechnik (IET-3)

Theory of Electronic and Ionic Perturbations at Supported Electrocatalyst Nanoparticles

Yufan Zhang

Schriften des Forschungszentrums Jülich
Reihe Energie & Umwelt / Energy & Environment Band / Volume 697

ISSN 1866-1793 ISBN 978-3-95806-896-4

Bibliografische Information der Deutschen Nationalbibliothek.
Die Deutsche Nationalbibliothek verzeichnet diese Publikation in der
Deutschen Nationalbibliografie; detaillierte Bibliografische Daten
sind im Internet über http://dnb.d-nb.de abrufbar.

Herausgeber und Vertrieb: Forschungszentrum Jülich GmbH
Zentralbibliothek, Verlag
52425 Jülich
Tel.: +49 2461 61-5368
Fax: +49 2461 61-6103
zb-publikation@fz-juelich.de
www.fz-juelich.de/zb

Umschlaggestaltung: Grafische Medien, Forschungszentrum Jülich GmbH

Druck: Grafische Medien, Forschungszentrum Jülich GmbH

Schriften des Forschungszentrums Jülich
Reihe Energie & Umwelt / Energy & Environment, Band / Volume 697

D 82 (Diss. RWTH Aachen University, 2025)

ISSN 1866-1793
ISBN 978-3-95806-896-4

Vollständig frei verfügbar über das Publikationsportal des Forschungszentrums Jülich (JuSER)
unter www.fz-juelich.de/zb/openaccess.

Abstract

The shift toward a defossilized economy and sustainable society depends on the development of high-performance and cost-effective energy storage and conversion technologies, such as fuel cells and electrolyzers. Electrochemical processes in these devices generally require the use of electrocatalysts to accelerate reactions towards certain products, yet current materials require improvements in activity, selectivity, and stability while remaining sufficiently cheap. Achieving these advancements necessitates rational design and knowledge-based optimization, which hinge on a fundamental understanding of the underlying physical and chemical processes.

Theory and computation offer a strong complement of experimental studies, allowing for in-depth understanding of catalytic mechanisms and structure–property relationships. Since electrocatalytic reactions occur at the electrical double layer (EDL) at the interface between a solid electrode and a liquid electrolyte, extensive simulation studies have focused on the structure and dynamics of the EDL. However, most of these studies have been limited to idealized homogeneous planar electrodes, whereas real electrocatalysts typically consist of nanoparticles (NPs) dispersed on support materials to maximize active surface area and thereby minimize loading. Though insights from planar electrodes provide a basic understanding, they overlook key features of supported NP electrocatalysts, including nanoscopic heterogeneities in composition and structure. At the NP–support interface, electron redistribution equilibrates Fermi levels, while at the NP–electrolyte and support–electrolyte interfaces, two EDLs overlap and codetermine the electric potential and ion distribution. Notably, the intricate interplay between electronic interactions and ionic interactions introduces complexities beyond the capabilities of existing methodologies.

This thesis addresses these challenges by developing a semiclassical continuum model within the framework of density–potential functional theory. The model captures correlated electronic and ionic equilibration across NPs, support, and electrolyte, and allows highly efficient simulations under both constant-charge and constant-potential conditions. Due to the availability of reliable experimental data on the differential capacitance of gold (Au) and silver (Ag) electrodes, they are chosen as the model system, with Ag NPs supported on an Au surface. Simulation results reveal that Fermi-level equilibration induces electron redistribution not only at the NP–support interface but also at their respective external surfaces in contact with the electrolyte. The electric field in electrolyte surrounding the supported NP leads to ionic charge separation. This peculiar behavior of external-surface charging and ionic separation seen in supported NP electrodes, validated through first-principles calculations, can be no longer described by the classical concept of the potential of zero charge (PZC) for planar electrodes. To address this, I define a global and two local characteristic electrode potential. The global PZC characterizes the overall charge-neutral state of the supported NP, while at the local level, support-induced perturbations in electronic and ionic charge densities at the NP's active surface give rise to two new characteristic potentials: the potential of zero local electronic charge (PZLeC) and the potential of zero local ionic charge (PZLiC). PZLeC and PZLiC differ by more than 0.5 V in dilute electrolytes but converge to the PZC in concentrated solution. Furthermore, I demonstrate that the differential capacitance curve can exhibit either one minimum or multiple minima, depending on the NP size.

Local ion concentration, pH, electric potential and field, subsumed as local reaction conditions, or local reaction environment, are crucial to catalyst activity, selectivity and stability. To better rationalize the local reaction conditions in supported NP electrodes, I introduce a descriptor, the effective reactant concentration, defined as the average reactant concentration over the reaction plane around supported NPs. Using Au-supported Ag NPs as a model system, I investigate how support material, NP size, NP coverage on support, bulk ion concentration and electrode potential affect this descriptor.

The methodology presented in this thesis enables accurate modelling of local reaction conditions at mesoscopic electrochemical interfaces at low computational cost. By providing a continuum-level description, this framework captures essential features of heterogeneous, multicomponent mesostructures while avoiding the complexity and computational cost of atomistic simulations. The insights gained contribute to the development of enhanced supported electrocatalyst systems and offer general relevance for understanding electrochemical properties in such systems. Follow-up collaborative work with experimentalists aims to visually demonstrate our simulation results on charge redistribution using electron holography. However, open questions remain regarding how to integrate actual catalytic processes into this framework, particularly chemical bonding phenomena that require atomistic-level descriptions. Future work will focus on bridging the gap between continuum modeling and atomistic simulations to achieve a more comprehensive understanding of the interplay between mesoscopic reaction conditions and molecular-scale catalytic mechanisms.

Zusammenfassung

Der Übergang zu einer defossilisierten Wirtschaft und einer nachhaltigen Gesellschaft hängt von der Entwicklung leistungsstarker und kosteneffizienter Energiespeicher und -umwandlungstechnologien wie Brennstoffzellen und Elektrolyseuren ab. Elektrochemische Prozesse in diesen Geräten erfordern in der Regel den Einsatz von Elektrokatalysatoren, um Reaktionen zu bestimmten Produkten zu beschleunigen. Dennoch müssen die derzeitigen Katalysatormaterialien in Bezug auf Aktivität, Selektivität und Stabilität weiter verbessert werden, jedoch gleichzeitig kostengünstig bleiben. Solche Verbesserungen erfordern ein rationales Design und eine wissensbasierte Optimierung, die auf einem grundlegenden Verständnis der zugrunde liegenden physikalischen und chemischen Prozesse beruhen.

Theorie und Simulationen ergänzen experimentelle Studien und ermöglichen ein tieferes Verständnis katalytischer Mechanismen sowie die Formulierung von Struktur-Eigenschafts-Beziehungen. Da elektrokatalytische Reaktionen in der elektrischen Doppelschicht (EDL) an der Grenzfläche zwischen einer festen Elektrode und einem flüssigen Elektrolyten stattfinden, haben zahlreiche theoretische und rechnergestützte Untersuchungen die Struktur und Dynamik der EDL untersucht. Die meisten dieser Studien beschränken sich jedoch auf idealisierte homogene planare Elektroden, während reale Elektrokatalysatoren typischerweise in der Form von Nanopartikeln (NP) vorliegen, die auf Trägermaterialien dispergiert werden, um die aktive Oberfläche zu maximieren und die Materialkosten zu minimieren. Obwohl Untersuchungen an planaren Elektroden ein grundlegendes Verständnis liefern, lassen sie entscheidende Merkmale von geträgerten NP-Elektrokatalysatoren außer Acht, darunter nanoskopische Heterogenitäten in Zusammensetzung und Struktur. An der NP–Träger-Grenzfläche erfolgt eine Elektronenumverteilung zur Angleichung der Fermi-Niveaus, während sich an den NP–Elektrolyt- und Träger–Elektrolyt-Grenzflächen zwei elektrische Doppelschichten überlappen und gemeinsam das elektrische Potential sowie die Ionenkonzentration bestimmen. Die komplexe Wechselwirkung zwischen elektronischen und ionischen Effekten führt zu Herausforderungen in der theoretischen Modellierung, die mit bestehenden Methoden nicht bewältigt werden können.

Diese Dissertation adressiert diese Herausforderungen durch die Entwicklung eines semiklassischen Modells, das die gekoppelte elektronische und ionische Gleichgewichtseinstellung zwischen NP, Träger und Elektrolyt beschreibt. Das Modell ermöglicht hocheffiziente Simulationen unter konstanten Ladungs- und konstanten Potentialbedingungen. Unsere Ergebnisse zeigen eine besondere Ladungsverteilung an der äußeren Oberfläche der geträgerten Ag-NP, die durch grundlegende quantenmechanische Rechnungen bestätigt wurde. Das klassische Konzept des Potentials der Nullladung (PZC) für planare Elektroden reicht nicht aus, um das Ladeverhalten geträgerter NP-Elektroden zu beschreiben. Stattdessen müssen ein globales und zwei lokale Varianten definiert werden. Das globale PZC beschreibt den ladungsneutralen Zustand der gesamten geträgerten NP-Elektrode, während auf lokaler Ebene durch trägerinduzierte Störungen der elektronischen und ionischen Ladungsdichten an der aktiven NP-Oberfläche zwei neue charakteristische Potentiale entstehen: das Potential der lokalen elektronischen Nullladung (PZLeC) und das Potential der lokalen ionischen Nullladung (PZLiC). In verdünnten Elektrolyten unterscheiden sich PZLeC und PZLiC um mehr als 0,5 V, während sie sich in konzentrierten Lösungen einem gemeinsamen Wert annähern. Darüber hinaus zeigen wir, dass die differentielle Kapazitätskurve je nach NP-Größe entweder ein einzelnes Minimum oder mehrere Minima aufweisen kann.

Um die lokalen Reaktionsbedingungen an geträgerten NP-Elektroden besser zu charakterisieren, führen wir einen Deskriptor ein: die effektive Reaktandenkonzentration, definiert als die mittlere Konzentration der Reaktanden in der Reaktionsebene um die geträgerten NPs. Anhand eines Modellsystems aus Ag-NPs auf Au-Träger untersuchen wir, wie Trägermaterial, NP-größe, NP-Bedeckung, Ionenstärke der Elektrolytlösung, sowie das Elektrodenpotential diesen Deskriptor beeinflussen.

Die in dieser Arbeit entwickelte Methodik ermöglicht eine präzise Modellierung lokaler Reaktionsbedingungen an mesoskopischen elektrochemischen Grenzflächen bei geringer Rechenkomplexität. Die gewonnenen Erkenntnisse tragen nicht nur zur Entwicklung verbesserter Elektrokatalysatormaterialien bei, sondern sind auch für das allgemeine Verständnis der elektrochemischen Eigenschaften heterogener, mehrkomponentiger mesoskopischer Strukturen von Bedeutung.

Acknowledgements

First and foremost, I want to express my deep gratitude to Prof. Dr. Michael Eikeling, my *Doktorvater*, who believed in my potential as an undergraduate and brought me to Germany for doctoral studies without a Master‘s degree. Michael, you are a wise and humorous man, approachable and kind in person yet rigorous and critical in science. I will always remember your words: “It is good to challenge yourself and challenge each other—sometimes you have to be stubborn, then be accommodating and flexible again.” Thank you for giving me the freedom to choose research topics, trusting me with the most difficult ones, and encouraging me to participate in the HITEC Communication Award and the Lindau Nobel Laureate Meeting. I’ve kept all the printed manuscripts you revised and marked in red in my folder, and I can proudly say I’m now able to decipher over 99% of your handwriting.

This doctoral journey will not be possible without Prof. Dr. Jun Huang. I remember seeking your advice when choosing between electronics and materials as my major in my freshman year. Just returned from Vancouver, you asked me: “Do you want to optimize within existing rules, or discover new laws and build your own edifice from the ground up?” Stepping out of the cafeteria, I had an answer in mind. Seven years before, you led me into theoretical research—something I once feared because of the equations and coding. But with your mentorship, I overcame my weaknesses. Half a year after I arrived in Jülich, fate brought us back together here. We’ve shared nearly five years side by side. You have been a source of care, guidance, and inspiration during the most difficult moments of my PhD. The theoretical framework at the heart of this thesis—density–potential functional theory—was pioneered by you. It is my privilege to be among the first to apply and extend it. Your commitment to academics as a lifelong pursuit, and your belief that a paper is a timeless endeavor, have carved out a place of purity in my heart.

Dr. Tobias Binninger, your arrival marked the second and most exciting half of my PhD. This thesis is deeply inspired by your earlier works. Your physical intuition, sharp mind, and clarity of thought constantly amazed me. I am thankful for the frequent and intense two-to-three-hour discussions in 2023, the fine-tuning of my presentation for the HITEC Communication Award competition, and the manuscript revision that elevates the work to another level. Not everyone in this world has the opportunity to receive this level of mentorship. I will also remember the *Spätzle*, Armagnac, and reggae music. Thank you for recognizing what was unique in me. *“We push the science to a place where everyone is crying and running away.”*

Special thanks to Prof. Dr. Alexei Kornyshev. My summer research in your group at Imperial College London, modeling electrical double layers, was a critical point. That experience showed me the elegance of theory, solidifying my decision to pursue theoretical research.

To Dr. Xinwei Zhu, my office-mate: we’ve shared every office throughout our PhD. You’re three years elder and wiser, and I’ve learned a lot from you. From mutual support through the pandemic and heartbreaks to encouragement as life got back on track—thank you for being there. As we both graduate, I wish us a future filled with excellent academic work.

Dr. Dechun Si, you picked me up at the airport when I first arrived in Germany and supported me ever since. I remember the crabs in the Netherlands, our chats in the office, and those delicious meals in Aachen. Much appreciated.

Dr. Wolfgang Obrich, my German brother. As you said, we are both *conceptual thinkers*. Though we only met at most twice a year, our connection was deep. After the HITEC Award in 2020, you played German songs with guitar while I served Martini. I visited you twice—once during the *Bundestagswahl* and once for your 30th birthday. Even when apart, we stay close via video calls. As you prepared for your defense in Aachen and I for my postdoc interviews in Lausanne, you told me: *“I don’t believe in fate; however, I cannot unsee the beauty of this coincidence. Time for us to be the scientists we always wanted to be.”*

Dr. Oskar Cheong, I’ll never forget the first time I heard you speak Chinese in *Seecasino*. During the pandemic, we taught each other DFT and microkinetics over Zoom. I remember the three bottles of wine at the reception, and our gym sessions in Leiden and Berlin.

Many thanks to the colleagueas in IEK-13 and IET-3: Dr. Rebekka Tesch, Binny Davis, Lukas Lübben, Felix Schmidt, Nils Bruch, Fabian Tipp, Andre Colliard, Zengming Zhang, Chenkun Li, Lulu Zhang, Kangjun Duan, Sandra Müller, Matthias Ross, Hania Azzam, Johanna Weidelt, Katarina Kretschmer, Dr. Dustin Vivod, Dr. Conor Price, Dr. Zhengda He, Dr. Weiqiang Tang, Dr. Thomas Kadyk, Dr. Piotr Kowalski, and Dr. Kourosh Malek—for generous help and invaluable support.

To my housemates over the years—Dr. Yuankai Yang and Dr. Zhi Jiang—you were like big brothers for me when I just arrived in Jülich at the age of 22. Thank you for your care, patience and the joyful moments we shared: the handmade noodles in my 23 birthday and the unforgettable trip in Portugal. Special thanks also to Ruoqian He, Haoran Jiang, Zhiwei Feng, Zhaohui Chen, Dr. Zhifeng Zheng, Zhen Yang, Xuan Zhou, Wenhao Shi, Dr. Hao Wang, Dr. Jie Chen, Dr. Xiao Li, Dr. Fuzhen Shen and Dr. Yuquan Qu—cooking together, drinking together, and sharing life stories have made Marktplatz 2 a real home.

To my football brothers—Chengdong Zhao, Songyao Bai, Chen Zhang, Jiajun Xu, Yuanwei Zhai, Mingzhao Liu, Wentao Fan, Bingzi, Hao Li, Han Zhou, Mengchen He and others. I didn’t started playing seriously until the age of 25, and I am grateful to meet you guys thereafter. The brotherhood we built through matches, summer parties, away games in Cologne, dinners, drinks, and karaoke are my happiest moments in Jülich.

I would also like to thank Mrs. Lu and my dance class friends. Every Saturday, we listen to the piano and practicing tendu and fondu. Walking out of the dance studio, I would look up at the blue sky and say to myself: what a wonderful day! Performing in front of IET-3 the Mongolia dance “Wild geese” and Tibetan dance “Zhuoma” were truly highlights of the year.

To my parents, Prof. Dr. Jianbo Zhang and Dr. Hong Li: my journey is a continuation of yours. Mom worked on catalysis in supercritical water and dad on fuel cells. I was six when I first visited mom’s lab at the University of Tokyo. *“These are all high-tech!”* I was amazed, with eyes wide open. From an early age, I was taken to science museums, art centers, and various exhibitions during visits to my parents in Japan. Our home was filled with books—science, history, and the humanities. I grew up watching my father sit straight at his desk, learning or working. I’m deeply grateful for the values I inherited. I am also in debt of my grandparents who raised me up at Yungang, a little town similar to Jülich. Your kindness shaped my inner self. When my parents were in Japan, my aunt and uncle were like my mom and dad—you drove me to school, brought me to the hospital when I got sick, travelled and played in vacations. Though my aunt passed away during my PhD, I know you are always there for me. I am also thankful to my grandparents in Kaifeng who gave me tremendous love and unwavering support.

Lastly, my heartfelt thanks to my girlfriend, Ms. Xiaoyue Wang. You’ve been with me through the darkest hours and the brightest days. You allow me to be myself. I remember biking through forests and fields after work, showing you the sunset while you were just going to bed in Beijing. After an intense workday, talking to you was like clearing a computer's full memory cache—suddenly, everything felt light again. You were there, in person or virtually, for every important milestone—my HITEC talk, PRL publication, Oxford interview, Lindau Meeting. You can empathize with my joys and sorrows. We have been to Roma, Sardegna, Paris, Istanbul, Cappadocia, Zürich, Luzerne, Interlaken, Spitz, Zermatt, St. Moritz. Let's stand side by side, hand in hand, and face the future together.

All of you have shaped not only this thesis, but also a part of who I am—both as a researcher and as a man.

My PhD has been a journey into the soul. It is good to remember what the path taken has been like. The way ahead? As Michael encouraged me using a quote from Steven Weinberg—I will continue seeking out the rough water.

Contents

1. Introduction

1.1. The role of electrochemistry in the energy transition

“Der Weg auf welchem diese größte aller technischen Fragen, die Beschaffung billiger Energie, zu lösen ist, dieser Weg muß von der Elektrochemie gefunden werden.” [1] In 1894, Wilhelm Ostwald stated that the path toward the procurement of cheap energy must be found by electrochemistry. More than a century after this prediction, his words are proving remarkably relevant in the 21st century. As the world faces the urgent challenges of climate change and energy sustainability, electrochemistry stands at the forefront and drives advancements in energy conversion, storage, and sustainable chemical production.

Since 1850, around 455 billion tons of carbon dioxide (CO_2) have been released into the atmosphere from fossil sources [2]. The Paris agreement emphasizes the urgency of limiting global warming to 1.5 °C above pre-industrial levels to avoid irreversible biodiversity loss and extreme weather events. Until 2024, the average global temperature has already risen by 1.3 degrees, leaving only 0.2 degrees on our budget [3]. Clearly, accelerated action needs to be implemented. The IPCC claims that only stopping emission of CO_2 is not sufficient, we must remove CO_2 from air and oceans to stop global warming [4,5]. Various carbon capture, separation and conversion technologies are being developed. For atmospheric CO_2 separation, techniques include ambient temperature pH swing and direct redox processes [6]. Methods for CO_2 capture and conversion from ocean water utilize systems such as direct-coupled bipolar membrane electrodialysis cells and vapor-fed CO_2 reduction cells [7].

Achieving net-zero emissions requires transforming into defossilised energy systems. Both ammonia (NH_3) and hydrogen (H_2) have the possibility to be low-carbon-intensity or carbon-free fuels that can lower the carbon footprint, if they are generated by renewables. For example, H_2 can be used for vehicles, drones and small aircraft [8,9], and NH_3 is under consideration as a fuel for the maritime industry [10]. Beyond transportation, they are also being considered as promising solutions for long-term, grid-scale energy storage [11]. By mitigating the temporal fluctuations of renewable energy sources such as wind and solar power, these energy carriers can enhance grid stability and facilitate deeper decarbonization. To realize this vision, electrolyzers for green hydrogen and ammonia production, along with fuel cells for energy conversion, are key technologies [12–14]. Additionally, battery technologies play a crucial role in the energy transition, with lithium-ion batteries being widely used for short-term energy storage, electromobility and grid stabilization [15], while solid-state batteries offer the potential for higher energy density and improved safety [16].

The strategies mentioned above, which encompass CO_2 capture and utilization, as well as hydrogen and ammonia production, storage and conversion, all involve electrochemical processes. As such, electrochemistry offers viable solutions for the energy transition by enabling clean energy production, efficient storage, and sustainable utilization across various sectors.

1.2. Electrocatalysis at electrified solid–liquid interfaces

In 1895, Ostwald put forward the definition of catalysis: “Catalysts are substances which change the velocity of a reaction without modification of the energy factors of the reaction.” [17] Since then, catalysts have transformed the world. Currently, over 80% of all industrial chemical processes utilize heterogeneous catalysts to accelerate the breaking or formation of chemical bonds at solid-gas or solid-liquid interfaces [18,19]. Most of the heterogeneous catalysts belong to thermal catalysts that operate under conditions of high temperatures and/or pressures, such as Raney nickel for the hydrogenation reaction, copper-based catalysts for the alcohol oxidation reaction, and platinum-group metals for vehicle exhaust treatment [19].

To reduce energy consumption and enable distributed chemical processes, catalysts that operate at lower temperatures and pressures are needed. The most advanced of these technologies utilize the electrochemical potential as the primary driving force in a process known as electrocatalysis, in which the catalysts are referred to as electrocatalysts. Notable examples of electrocatalysts include carbon-supported platinum nanoparticles (NPs) in hydrogen fuel cells, oxide-supported iridium-based NPs in water-splitting devices, and coinage metals in CO_2 electrolyzers [20–22].

There are three key metrics for electrocatalysts: catalytic activity, selectivity, and stability. Catalytic activity indicates the rate or turnover frequency at which a reaction can occur with the help of the catalyst. Selectivity measures the percentages of the products belonging to desired one. Stability refers to the duration of time over which a catalyst maintains its structure integrity and functionality. There is, usually, a trade-off between the key metrics and the cost—well performing catalysts are generally made of noble metals that are scarce in our planet and of high monetary value. To make the use of catalyst economically viable, researchers have been trying to either minimize the amount of catalyst used or come up with new catalyst with nonprecious materials.

Catalysts aid in breaking and formation of chemical bonds during adsorption of reactants, generation of intermediate species, and desorption of products. The Sabatier principle of heterogeneous catalysis states that the interaction between a catalyst surface and adsorbed reaction intermediates should be neither too weak nor too strong [23]. If the interaction is too weak, then the reactant will not adsorb onto the catalyst surface, limiting the catalyst’s influence on the reaction. On the opposite, if the interaction is too strong, the adsorbed species will be very difficult to convert further or desorb from the surface, hindering the reaction progress. The interaction is often quantified by the binding energies of reaction intermediates on a catalyst surface.

Scaling relations describe intrinsic correlations between binding energies of different reaction intermediates on a catalyst surface, meaning that optimizing one step often affects others in a predictable manner that can be captured in linear relations. These relations give rise to the volcano plot, which displays the catalytic activity as a function of the binding energy of a key reaction intermediate [24]. The plot typically exhibits a peak, indicating an optimal balance between adsorption strength and reaction turnover, with catalysts on either side being limited by either too weak or too strong binding.

In the 1950s, Parsons and Gerischer derived a volcano-shape curve for the hydrogen evolution reaction (HER) [25,26]. In the 1970s, Trasatti compiled the first experiment-based volcano plot for the HER which employed the hydrogen adsorption enthalpy extracted earlier by Krishtalik from experimental data [27,28]. Recently, the dependence of the volcano curve on electrode potential has been extensively discussed [29–32].

Unlike thermal catalysis, which occurs at the solid–gas interface, electrocatalysis takes place at the solid–liquid interface, also known as the electrode–electrolyte interface.

By externally controlling the electrode potential, the electrode surface can carry excess positive or negative charge, which is balanced by a charge of equal magnitude and opposite sign on the solution side of the interface. The resulting charge distribution, consisting of two regions with equal and opposite charges, is known as the electrical double layer (EDL). In a highly schematized view, the EDL can be considered as a capacitor with a small effective plate separation. At a specific electrode potential, the electrode surface holds no excess charge, and thus, no ion accumulation occurs in the electrolyte. This specific potential is known as the potential of zero charge (PZC), as illustrated in Figure 1 [33].

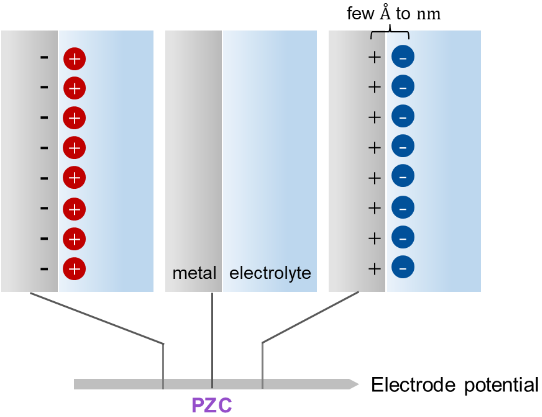

Figure 1. Schematic of electrode–electrolyte interface at different electrode potential.

By comparing the electrode potential with the PZC, one can determine whether the electrode surface carries a positive or negative excess charge. The magnitude of the excess charge also depends on the differential capacitance of the solid–liquid interface, which is defined as

$$C_{\mathrm{d}} = \frac{\mathrm{d}\sigma}{\mathrm{d}E}, \tag{1}$$

where σ is the surface charge density and E is the electrode potential.

The differential capacitance at solid–liquid interfaces, neglecting contributions from specific adsorption, typically ranges from 10 to 60 μF/cm². It can be experimentally determined using techniques such as electrocapillarity measurements, electrochemical impedance spectroscopy, or cyclic voltammetry [34,35]. In addition to experimental approaches, the capacitance can also be calculated from theoretical models.

The differential capacitance exhibits a strong dependence on the electrode potential, and the shape of the C_d vs. E curve serves as a fingerprint of the interfacial structure of the EDL. The curve entails, in a highly condensed form, information about the concentration, valence, and size of electrolyte ions, the dielectric constant of solvent molecules, and the PZC [36]. The capacitance can be divided into several contributions from different regions in the solid–liquid interface. These comprise of the quantum capacitance arising from the electronic structure of the electrode, adsorbate layer, gap region between the electrode and electrolyte, as well as solvent and ionic layers. Due to its physical relevance, the differential capacitance is often used as a benchmark for validating theoretical and computational models of electrochemical interfaces.

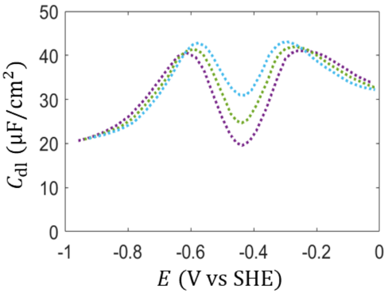

Figure 2. Differential double layer capacitance curves of Ag(111) electrode in KPF_6 solution, measured in 10 mM (purple), 20 mM (green) and 40 mM (blue). [37]

Interfacial reaction conditions in the vicinity of the electrocatalyst surface, namely the local concentration of reactants, the local pH, the electric field and electric potential distribution, constitute the so-called local reaction environment (LRE). The LRE is significantly affected by the surface charges on the electrode surface, which, in turn, depend on the difference between applied electrode potential and PZC, as well as the differential capacitance. The performance of electrocatalytic processes depends primarily on both the electronic structure of electrocatalysts and the LRE. Over the past few decades, significant efforts have been made to design new catalysts, including single-atom catalysts [38,39], single-atom-alloy catalysts [40], tandem structures [41,42], and core–shell NPs [43]. These advancements focus on modifying electronic structure and chemical properties to enhance catalytic activity. Recent studies highlight the crucial role of optimizing the LRE in order to enhance electrocatalytic activities. For instance, nanostructured Pt electrocatalysts exhibit superior activity for the hydrogen evolution reaction (HER) in alkaline electrolytes compared to their bulk Pt counterparts [44]. A deep understanding of the LRE is essential for advancing electrocatalytic performance.

In summary, electrocatalysis research mainly focuses on two areas: the intrinsic electronic properties of catalyst surfaces, governed by short-range electronic interactions, and the LRE in the catalyst–solution interfacial region, in which long-range electrostatic interactions dominate. In this thesis, I aim for a theoretical understanding of the LRE, which is a prerequisite for knowledge-based catalyst optimization and design.

1.3. From planar electrodes to supported NPs

Noble metal catalysts have the problems of high cost and scarcity, which severely hinder their widespread application [12,45]. In order to overcome these issues, many studies explore strategies for minimizing the catalyst loading without sacrificing on the catalytic performance. One plausible way to achieve this is to use a support material that increases the dispersion of catalyst NPs and the active surface area, thereby increasing the utilization of the electrocatalyst [46]. Supported NP catalysts have a larger proportion of catalyst atoms exposed at the surface, *i.e.*, a higher surface-to-volume ratio, to participate in catalyzing electrochemical reactions.

An ideal support material for electrocatalyst NPs must fulfill several requirements. It should possess a high surface area and a porosity tailored to maximize the dispersion of active sites while ensuring optimal mass transport of reactants and products. Additionally, the support material should exhibit excellent chemical and electrochemical stability to withstand harsh reaction conditions, and high electrical conductivity to facilitate electron transfer. In general, carbon materials are used to support electrocatalyst NPs. Examples include supported Au NPs for carbon dioxide reduction in CO_2 electrolysis cells [44], supported Pt NPs for ORR in proton exchange membrane fuel cells [48]. However, in highly corrosive environments—such as those involving high potentials during the oxygen evolution under acidic or alkaline conditions—electrochemical carbon corrosion is significantly accelerated, leading to the degradation of catalytic activity. Consequently, alternative corrosion-resistant support materials, including graphitized carbon [49], metal carbides [50], metal nitrides [51], and conductive metal oxides [52], have been developed and used in electrocatalyst systems.

Optimization of the supported catalyst performance in terms of activity, selectivity and stability will not be possible without a theoretical understanding into how support and NP interact with each other and how these interactions modulate the catalytic activity.

Compared to homogeneous planar electrodes, supported electrocatalyst electrodes feature heterogeneities in both composition and structure. The electronic structures of catalyst and support give rise to distinct electronic and electrochemical properties including work function and adsorption energy of reactants. Moreover, their different interactions with solvent and electrolyte influence the PZC and capacitive response, thus determining the local reaction conditions. The nanosized geometry of the catalyst NPs deviates the electrochemical and catalytic properties from those of planar extended electrodes.

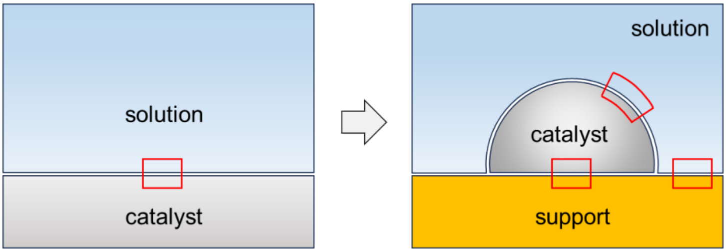

Figure 3. Schematic of a planar electrode and a supported electrocatalyst electrode.

Contact of catalyst and support, and immersion in a solution environment, further complicate the system. Compared to the simple catalyst–solution interface at planar electrodes, there are three interfaces at supported catalyst electrodes, namely the catalyst–support interface, the catalyst–solution interface and the support–solution interface (see Figure 3). A deep understanding of the interactions and simultaneous equilibration occurring at these three interfaces and the emerging phenomena are crucial for the rational design and optimization of supported NP systems.

It has been reported in the literature that the catalytic performance in supported NP systems is influenced by several factors, including NP size, NP proximity (interparticle distance), or the purported metal–support interactions (MSI), among others. The following sections explore these factors with representative examples.

Change of NP size can affect NP shape and the proportion of the exposed facets. For example, carbon-supported Pt catalysts with an average particle size of 1.8 to 5.4 nm and metal loading of 20 wt% were prepared by wet synthesis. The decrease in the particle size results in a change in the particle shape and an increasing fraction of the less active (111) surface facets [53]. Another study investigated Pt NPs with diameters ranging from 2 to roughly 11 nm, fabricated by the gas aggregation technique, mass-selected, and deposited directly onto planar glassy carbon supports under ultrahigh vacuum. The ORR activity approximately correlates with the fraction of the terrace sites [54]. It is also postulated that edge and corner atoms have an even lower coordination and bind foreign atoms and molecules more tightly [55].

As the NP size decreases, quantum confinement effects become significant. Specifically, the continuous valence band of bulk metals begins to split into discrete energy states, resembling the electronic structure of semiconducting oxides. According to the Kubo criterion, the NP loses its metallic properties when the band gap surpasses the thermal energy $k_\mathrm{B}T$ (where k_B is the Boltzmann constant and T is the temperature), altering its electronic behavior and catalytic performance [56].

When the NP size is fixed but the interparticle distance is varied, the surface specific activity normalized to the electrochemical surface area of Pt increases at shorter interparticle distances, a phenomenon known as the NP proximity effect. Investigations by Nesselberger et al. and Huang et al. gave first hints that EDL effects (spanning 1–100 nm) contribute to the particle proximity effect of Pt/C catalysts [57,58]. At 0.9 $\mathrm{V_{RHE}}$, the Pt surface is negatively charged due to oxide layer formation, whereas the C surface is positively charged. Therefore, the proton concentration will be higher in the EDL of the Pt surface than in the EDL of the C surface. If Pt NPs locate closer to each other, the EDLs of neighouring NPs will overlap, increasing the proton concentration and thereby the rate of ORR [58].

Supports are typically not inert and the interactions with NPs give rise to new interface phenomena. These phenomena, often sweepingly subsumed under metal–support interactions (MSI), may have a profound impact on the electrocatalytic performance of the metal NPs [59]. Typical phenomena relate to electron redistribution, intermediates spillover, NP morphology, chemical composition and strong metal–support interaction (see an excellent review article ref. [60]). These phenomena are often entangled and some will have a stronger influence than others, depending on the specific system and the reaction of interest.

Electron redistribution at the metal–support interface, driven by differences in the Fermi levels of the metal and support, ultimately leads to equilibration of these Fermi levels. This phenomenon known as electronic metal–support interactions (EMSI) [61]. Atoms at the perimeter favor the accumulation or depletion of electrons, which regulate adsorption and reactions of molecules therein [62]. This rearrangement of electrons can modify oxidation states of the metal atoms and thereby alter adsorption properties. The extent of EMSI depends on the difference in Fermi levels, which in turn is affected by factors such as NP size and the work function of the exposed crystal planes. The conductivity of the support influences the efficiency of electron transfer at the metal–support interface, thereby affecting the extent of EMSI. Additionally, the reducibility of the support modulates its ability to exchange electrons with the metal NPs, further tuning the electronic interactions at the interface.

Another process that is possible at the interfacial perimeter is reactant spillover. It begins with the activation of a reactant on one surface, typically the metal NP, followed by its transfer to the support. The most extensively studied spillover involves hydrogen, while oxygen and other molecules like CO and $-OCH_3$ are also relevant, albeit to a lesser extent [63,64].

The shape of supported NPs can be affected by the adhesion energy at the metal–support interface [65]. The equilibrium shape of a metal NP is typically determined by minimizing its total surface free energy. Interaction with the support can reduce the surface energy of specific NP facets, in favor of certain shapes. Additionally, lattice mismatch between the support and the NP can induce strain, altering the NP's morphology [66].

Another highly relevant interaction is strong metal–support interaction (SMSI), where under reducing conditions, mobile suboxide species from the support partially encapsulate the NP [67]. Prominent examples include NP/support combinations of Pt/TiO_2, Pt/Fe_3O_4, Pd/TiO_2, Ni/TiO_2 and Au/ZnO [68–71]. While excessive coverage can block active sites, moderate SMSI can suppress NP sintering and aggregation, improving the stability of supported NPs. In addition, SMSI modifies the electronic structure of the NP, introducing Lewis acidity, and, ultimately enhancing its performance.

In general, the impact of MSI rapidly decays with increasing particle size and the highest enhancements were obtained for particles smaller than 4 nm [60].

Compared to planar electrodes, supported NP electrodes are more representative of practical catalytic systems. Although they exhibit greater structural and compositional complexity, this complexity also opens up more avenues for tuning and optimization. A critical prerequisite for rational design is a mechanistic understanding of the various interactions occurring within supported NP systems. Rather than relying solely on experimental studies, a more efficient strategy is to gain insight through modeling. In the following section, I will introduce various modelling approaches for electrochemical interfaces.

1.4. Modelling of electrochemical interfaces

Theoretical studies of electrochemical interfaces can generally be categorized into two broad classes: energy-minimization approaches and statistical-sampling approaches. Energy-minimization approaches aim to describe the EDL structure under the assumption of thermodynamic equilibrium. These include i) classical continuum models [26,46–54], and ii) hybrid quantum–classical approaches [72–83]. In contrast, statistical-sampling approaches such as molecular dynamics and Monte Carlo do not rely on equilibrium assumptions, but instead provide atomistic insight by sampling the phase space directly. In this section, the focus will be on the first class of models, while the second will be briefly mentioned for completeness.

Classical continuum models assume a homogeneous layer of surface charges on the electrode and treats the electrolyte using various continuum solvation models. The continuum solvation models can be further divided into mean-field models, which approximate interactions by averaging over all particles, and classical density functional theory models, which explicitly accounts for spatial correlations beyond the mean field approximation. Meanwhile, mean-field models have been augmented by correction terms for electrostatic correlations beyond the mean-field level [84–87].

The quantum–classical hybrid models combine a quantum-mechanical representation of the electronic structure of the electrode, with classical solvation models for the electrolyte. Compared with classical continuum models, the quantum–classical hybrid models provide a more detailed description for the electrode part, which comes at the expense of higher computational cost.

In the following, I will first review the development of classical continuum models over the past century, followed by a brief introduction of different quantum-classical hybrid approaches.

Modelling of electrochemical interfaces can be traced back to Helmholtz who viewed the EDL as a parallel plate capacitor consisting of one layer of charges on the metal electrode and one rigid layer of charged species on the electrolyte side (see Figure 1) [88]. Gouy and Chapman replaced the rigid layer of ions by a diffuse layer of point charges placed in a dielectric continuum. The applicability of the Gouy–Chapman model is limited to low electrolyte concentrations and low interface charges, because otherwise the ion concentration at the EDL becomes unphysically high. Stern [41] addressed this problem by combining the Helmholtz model with the Gouy–Chapman model: a first rigid layer of ions is set at a predefined distance to the surface of closest approach for the ions (called Helmholtz plane), adjacent to a Gouy−Chapman diffuse layer [89–91]. The Gouy−Chapman−Stern (GCS) model treats the electrolyte region as continuum medium and describes the metal as a featureless boundary with controlled surface charge density or electrode potential.

The model was later improved by Grahame who divided the Helmholtz plane into an inner Helmholtz plane (IHP) and an outer Helmholtz plane (OHP). The IHP consists of the first layer of adsorbed solvent molecules together with specifically adsorbed ions while the OHP corresponds to the closest approach of solvated ions. Bockris et al. further incorporated solvent effects by considering the orientation of solvent molecules at the interface in response to surface charge [92]. Solvent polarization and orientation also exert notable effects on the interfacial dielectric constant.

For concentrated electrolyte, the excluded volume of solution species plays a crucial role in determining the ion distributions and EDL capacitance. The steric effects can be incorporated into the PB equation by using lattice-gas models, as first proposed by Bikermann and further developed by Orland, Kornyshev and Bazant, resulting in the so-called modified Possion-Boltzmann (MPB) models [36,93–96].

Compared with alternative approaches, one major advantage of mean-field methods is their simplicity and efficiency in capturing the main features of EDL. Additionally, they facilitate the development of analytical solutions and provide physical insights that may be difficult to obtain through molecular simulations or more complex theoretical frameworks.

However, the mean-field models suffer from the disregard of the molecular nature of ions and solvents. Besides, they accounts only for the Coulomb interactions in a uniform dielectric medium at the mean-field level. Since electrostatic correlation effects are not considered, they are not able to reproduce the oscillating behaviors of ion density profiles seen in experiments and particle-based simulation methods such as Monte-Carlo and molecular dynamics simulations [97,98].

To address these limitations, additional correction terms have been introduced into the mean-field framework to account for oscillatory electric potential and ion density profiles arising from strong electrostatic correlations and excluded-volume effects. A modified electrostatic energy term is introduced to obtain a fourth-order PB equation in the Bazant–Storey–Kornyshev model [85]. Other refinements include using weighted density approximation [86], incorporating ionic clusters, [87] and modeling ion pairs as neutral particles when their separation distance is below a certain threshold—while treating them as point charges otherwise [84].

Another class of methods employs classical density functional theory (cDFT), which goes beyond the mean-field approximation by including two additional contributions to the free-energy functional: hard-sphere interactions and electrostatic correlations [99]. Accounting for both particle packing and correlation effects, cDFT can capture nonintuitive electrostatic phenomena, such as oscillatory ionic distributions and charge inversion.

cDFT is mathematically rigorous within the context of a specific thermodynamic model. However, approximations are often used to formulate the free-energy functional, including simple mean-field approximations, more advanced weighted density approximations [100], and even more sophisticated methods such as the fundamental measure theory [101,102].

Classical continuum models assume a uniform surface charge density at the electrode surface. However, as early as the 1920s, Frumkin discovered that the uniform surface charge could not explain certain experimental phenomena [103]. In 1928, Rice explicitly considered the electronic structure of the electrode and its response to the electrolyte [104]. It was not until the 1980s, when the electronic structure of electrode surfaces in solution could be experimentally measured, that the electronic structure of electrodes was routinely taken into account in theoretical models. In recent years, due to increasing interest in electrochemical reactions, theoretical studies on the electronic structure of electrodes have gained increased momentum. Upon considering the electronic structure of the electrode, several phenomena can be described, including the emergence of quantum capacitance and pseudocapacitance [105,106].

In the 1980s, so-called Jellium models treated metal electrons as an interacting inhomogeneous electron gas, and metal cationic cores as positive background charges [107,108]. The electrolyte solution is represented by dipoles interacting with metal electrons [80,81] or using the Gouy−Chapman model [79].

Over the past decades, significant advancements have been made in modeling electrochemical interfaces, leading to the development of more sophisticated quantum–classical hybrid models. Notable examples include: DFT+MPB models [72,109], joint DFT (jDFT) models [74], effective screening medium–reference interaction site model (ESM–RISM) [77], quantum mechanics/molecular mechanics (QM/MM) [110], and density–potential functional theory (DPFT) [111]. Based on whether the solvation model uses a continuum or a discrete approach, and whether the electronic structure is treated by orbital-based or orbital-free DFT, these methods can be classified into four groups, as shown in Figure 4.

The distinguishing feature of QM/MM compared to other models is that it represents the electrolyte using an atomistic model, whereas other approaches employ continuum descriptions. For the electrode, QM/MM methods exist in both orbital-based and orbital-free variants. Among continuum models, as displayed at the left column in

Figure 4, ESM–RISM employs integral equations, while DFT+MPB, jDFT, and DPFT rely on density functionals. Located at the bottom-left corner in Figure 4, DPFT sets itself apart by employing orbital-free DFT, whereas DFT+MPB and jDFT adopt orbital-based DFT. In the following paragraphs, I will give a broad overview of each method.

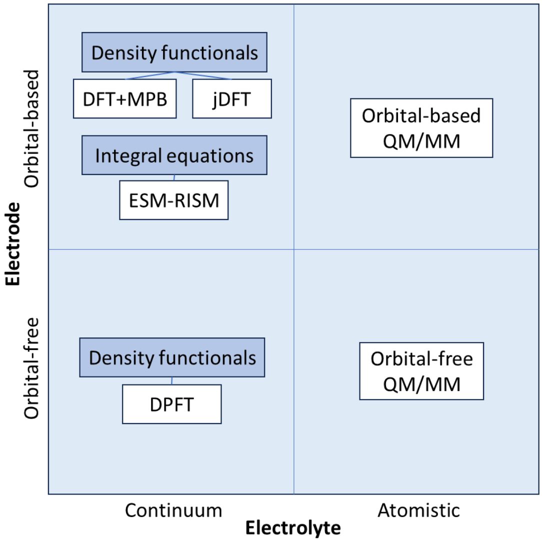

Figure 4. Classification of hybrid quantum–classical models based on the treatment of the electrode and the electrolyte.

The QM/MM approach is a molecular simulation method that combines the strengths of *ab initio* QM calculations (accuracy) and MM (speed) approaches, thus allowing for the study of chemical processes in complex structures, such as enzymes, with the solution environment considered [110]. The QM/MM approach was introduced in the 1976 paper of Warshel and Levitt [112]. Together with Martin Karplus, they won the 2013 Nobel Prize in Chemistry for "the development of multiscale models for complex chemical systems".

The essence of this technique lies in partitioning the system into distinct regions: QM is applied to the central region of interest to accurately compute the energetics, while MM is used for the surrounding environment to efficiently account for electrostatic interactions. Originally developed for structural biology, QM/MM models have increasingly been adopted in heterogeneous catalysis, offering a balance between computational efficiency and accuracy in complex reaction environments [113]. For instance, QM/MM simulations have been employed to study reaction mechanisms within zeolitic systems, adsorption processes in solvents at metallic interfaces, and defect chemistry in ionic solids [110].

MM in its original meaning indicates conducting energy minimization to get an equilibrium conformation, implying static calculations. However, many QM/MM approaches to date are actually performing molecular dynamics instead of molecular mechanics simulations. The term “molecular mechanics” in the QM/MM terminology is retained because of a historical reason. The integration of QM/MM methods naturally evolved from early studies on enzymatic reactions, where MM optimizations were initially used to generate starting structures for subsequent QM calculations [114].

Unlike QM/MM methods which model the solvent structure explicitly in an atomistic level, the other methods summarized in Figure 4 utilize continuum solvation models.

In ESM–RISM, the RISM serves as the solvation model, representing solvent molecules as sets of interacting sites [77]. Instead of treating solvent molecules explicitly, RISM solves integral equations to obtain statistical solvent distributions [115]. Compared to continuum solvation models like the Poisson–Boltzmann (PB) equation, RISM provides more detailed structural information about the solvent, albeit not through an atomistic description but in a statistically averaged manner. This feature allows RISM to capture solvent oscillations, which are often missing in traditional continuum models.

The ESM method implements mixed boundary conditions for DFT calculations of solid–liquid interfaces [116]. It enables the system to be periodic in directions parallel to the surface, while remaining non-periodic in the perpendicular direction, where it is effectively sandwiched between semi-infinite media, such as vacuum, an electrode, or an electrolyte. This setup allows for a more realistic treatment of interfacial phenomena at electrochemical interfaces.

Aside from ESM–RISM, which utilizes integral equations, another broad class of continuum models employ density functionals in their treatment for solvation. According to Arias, these models can be divided into DFT+MPB approaches and jDFT approaches. The DFT+MPB approaches account for both the Debye screening effects of the ions and the dielectric response of the water molecules. *Ab initio* calculations are performed where the electrostatic potential is determined by solving Poisson–Boltzmann-like equations [72,116,117]. While explicitly capturing the most notable electrolyte phenomena, such Poisson–Boltzmann-like approaches do not originate from an exact underlying theory. As a result, they may overlook important physical effects, such as the surface tension associated with formation of the liquid-solid interface, and the nonlocality and nonlinearity of the dielectric response of liquid water [74].

Arias' jDFT establishes a rigorous theoretical foundation for MPB approaches within an exact density functional framework and systematically extends them to incorporate all relevant physical effects in a fully ab initio manner. [74,118] It has been demonstrated that the DFT+MPB approach can be understood as approximations of a more fundamental, rigorous methodology. Within the jDFT framework, the energy functional consists of three key components: a standard Kohn–Sham DFT (KS-DFT) functional describing the electron density of the electrode in isolation, a cDFT functional representing the electrolyte environment independently, and a coupling term that captures interactions between the electrode and the electrolyte. Therefore, jDFT is essentially a hybrid of KS-DFT and cDFT. Despite employing a simplified functional, jDFT enables the exploration of fundamental electrochemical phenomena, such as microscopic variations of the electrostatic potential near electrode surfaces, the structure of the electrochemical double layer, variations in differential capacitance, and the PZC across different metals.

Recently, several multicomponent or grand-canonical DFT methods have been developed by integrating KS-DFT with various formulations of the PB equation [119,120].

While the above quantum–classical hybrid models offer high accuracy and efficiency in capturing electronic properties of the electrode and ionic/dielectric properties of the electrolyte environment, their default canonical framework can only simulate a fixed number of particles, unable to reflect the grand canonical nature of realistic EDL [121]. A significant number of research efforts have been dedicated to achieving grand-canonical ab initio simulations of the EDL [77,119]. The computational costs are, however, extremely high. An EDL model that includes main effects in both the electrode and the electrolyte, enables constant-potential simulations, and retains the computational efficiency of mean-field approaches is still lacking.

The recently developed semi-classical model by Huang represents a physically consistent approach to treat electronic and ionic degrees of freedom [111,122–124] and it addresses the challenge of constant-potential simulations. DPFT employs a functional approach to model mixed quantum–classical open systems. Specifically, metal electrons are described using orbital-free quantum-mechanical DFT, while the electrolyte solution is treated via classical statistical field theory. The resulting grand potential expression for EDLs is formulated as a hybrid functional of electron density and electrostatic potential. Consequently, we refer to this approach as density–potential functional theory (DPFT). Applying variational analysis to the grand potential functional with respect to electron density and electrostatic potential gives two governing equations, which are solved under constant electrochemical potentials of both ions and electrons. DPFT has been successfully applied to describe the EDL at Ag(111)–aqueous solution interfaces in the absence of specific adsorption.

The DPFT framework builds upon the foundational work of Lang and Kohn's jellium models for metal surfaces from the 1970s [107,108], as well as the jellium–dipole models for metal–solution interfaces developed in the 1980s by Schmickler and others [80,81]. These early models were among the first implementations of orbital-free electronic theories. While the jellium–dipole models were formulated under constant-charge conditions, DPFT extends this approach to enable constant-potential simulations, a crucial advancement for electrochemical studies. Additionally, DPFT captures the influence of metal electronic effects and electron–electrolyte interactions on the differential double-layer capacitance. Furthermore, chemisorption of ions can be incorporated into a modified DPFT framework by embedding a model Hamiltonian treatment of electronic interactions between the metal and chemisorbed species [125].

The crucial advancement of our DPFT model lies in its ability to solve the Euler–Lagrange equations for both electron density and electrostatic potential under constant electrochemical potentials, offering a more comprehensive and consistent approach. Unlike earlier models, which relied on trial functions to approximate electron density distributions and were constrained to small charge densities, DPFT provides a rigorous treatment that is not limited by these constraints, enabling more accurate and scalable simulations of electrochemical interfaces.

In addition to enabling constant-potential simulations of EDLs, another key advantage of DPFT is its low computational cost, which allows it to handle larger systems, including EDLs at mesoscopic or even macroscopic scales [126]. This computational efficiency arises from two factors: elimination of the need to calculate electronic orbitals and implicit treatment of the electrolyte solution. Once parameterized using a small set of ab initio calculations, the DPFT approach provides a pragmatic path for simulating EDLs at mesoscopic structures containing millions of atoms, a scale that remains out of reach for ab initio methods for the foreseeable future.

In addition to equilibrium models, simulations such as Molecular Dynamics (MD) and Monte Carlo (MC) can also be used to study electrochemical systems [98,127–129]. MD simulations simulate the time evolution of a system by numerically integrating the equations of motion for each particle. This approach captures the dynamics and interactions of molecules over time, allowing the study of time-dependent behaviors such as diffusion, structural rearrangements, and the evolution of the system under varying conditions.

MC simulations sample configurations probabilistically, providing a statistical framework to explore the phase space of a system. They are particularly useful for studying systems where configurations are sampled based on their probabilities, without explicitly tracking the time evolution of particles.

These simulation methods can serve as valuable benchmarks for theoretical models. Since both MC and MD are atomistic and particle-based approaches, they can accurately capture molecular structures, correlations, and fluctuations, providing detailed insights that are often difficult to obtain from continuum models.

In summary, a wide range of modeling approaches exist for studying electrochemical interfaces, each with its peculiar strengths and limitations. Researchers must carefully choose the method that best suits their specific system and aligns with their research goals—whether the aim is to achieve high accuracy or to perform an initial screening. Practical considerations such as the availability of computational resources should also be taken into account when selecting the appropriate modeling strategy.

1.5. Overarching goal of the thesis

The overarching goal of this PhD thesis is to unravel the charging behaviors and the resulting local reaction environment (LRE) of supported electrocatalyst NPs under electrochemical conditions. While classical electrochemical concepts and models have provided profound insights into planar interfaces, the transition to nanostructured catalysts introduces new complexities that remain insufficiently understood.

To address this, the thesis aims to tackle the following key scientific questions:

1. Are classical charging concepts sufficient for supported NPs?
   Electrochemical properties such as the PZC and differential capacitance are well-defined for planar electrodes and have been extensively studied both experimentally and theoretically. However, it remains unclear whether these concepts fully capture the charging behavior of supported NPs under electrochemical conditions. Are there new features or deviations that arise due to nanoscale curvature or support effects?

2. How does the interplay between electronic MSI and ionic MSI influence charging behaviors of supported NPs?
   MSI have been widely investigated in the context of thermal catalysis, where catalysts operate in the gas phase. In electrocatalysis, however, the presence of an electrolyte environment introduces additional electrostatic and solvation effects at the interface. How does the interplay between electronic MSI and ionic MSI alter the charge distribution within supported NPs? Does this give rise to new charging behaviors and interface phenomena?

3. Can we develop a practical descriptor for the LRE in supported NP systems?
   The LRE at the active sites of electrocatalysts is crucial for reactivity and selectivity. This work seeks to define a descriptor that captures how electrochemical charging alters the LRE in supported NP systems. How does this descriptor respond to parameters such as NP size, NP proximity, support material, electrolyte concentration, and applied potential?

To fill in the gaps, this Ph.D. research has taken a step-by-step procedure. Firstly, it strives to accurately reproduce the electrochemical properties of separate catalyst and support. Especially, accurate PZC values and differential capacitance are crucial for modelling the structure of the EDL and rationalizing LRE. To this end, the effect of metal–solvent specific interactions (Chapter 2) and a three-step calibration workflow for model parameters (Chapter 3) has been developed, which together represent a major advancement of the DPFT methodology. Secondly, with the catalyst and support well-described separately, a simple system consisting of a catalyst slab in contact with a support slab (Chapter 3) has been considered to study electronic perturbations at the metal–metal interface.

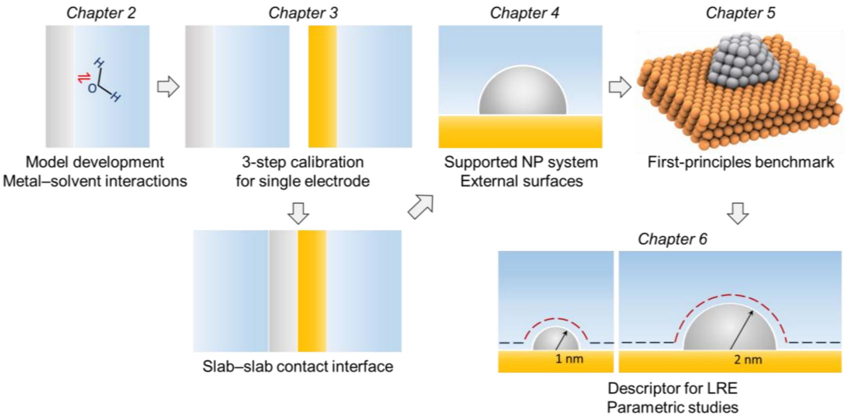

Figure 5. The overall structure of the thesis.

Building on this, the thesis proceeds to model the main object of interest, a supported NP electrode, using the developed DPFT framework (Chapter 4), and benchmark the DPFT results against first-principles quantum mechanical calculations (Chapter 5). Key quantities such as the spatial variation of electronic and ionic charge densities at the external NP–electrolyte interface, the global work function and the global PZC of the combined system, and its overall capacitive response are systematically investigated. These quantities play a critical role in determining the LRE.

Finally, a descriptor tailored for LRE in supported NP systems is proposed: the effective proton concentration around supported NPs (Chapter 6). I analyze how this descriptor and thus LRE depends on key parameters, including NP size, NP proximity, support material, electrolyte concentration, and applied potential.

2. Modelling methods

2.1. Introduction

EDL models based on MPB theory neglect electronic equilibration inside the solid phase [95]. First-principles calculations of electrochemical interfaces face challenges not only in constant-potential simulations [130–133] but also in their considerable computational cost, rendering them unsuitable for systems containing thousands of atoms, such as electrolyte-surrounded supported nanosized particles. Consequently, previous studies of EMSI effects were restricted to the contact interface between a sub-nanometer cluster and its support in vacuum [134,135]. It remains unclear in what way electrons redistribute at the external surface of NPs in contact with electrolyte. As a result, a gap remains in understanding joint effects of electron redistribution at the solid surfaces of the NP and support, along with the overlap of EDLs formed at these distinct components of the heterogeneous surface, on electrochemical properties.

The recently developed hybrid quantum–classical DPFT represents a physically consistent approach to treat electronic and ionic degrees of freedom [111,122–124]. By handling metal electrons through orbital-free DFT [83,136,137], this approach treats the electron system through a continuous density field, enabling constant-potential simulations by fixing the electrochemical potential of electrons, $\tilde{\mu}_{\mathrm{e}}$. Furthermore, it ensures high efficiency in simulating mesoscale systems which is beyond the reach of Kohn-Sham DFT. Meanwhile, classical particles including solvents and ions are treated using statistical field theory [36,96,138].

DPFT in its existing version [111] cannot capture the work function in vacuum and the PZC in solution by a set of parameters. This is due to an insufficient description of metal–solvent interactions. For the present study, capturing the PZC is a prerequisite for modelling heterogeneous multi-component systems. Therefore, more accurate description for the metal–solvent interaction is needed. In this chapter, I will first present the DPFT framework in its basic form and then introduce the newly developed treatment of metal–solvent interactions. I will explain how the model parameters are calibrated for gold and silver planar electrodes. Having obtained reliable model parameters, I will demonstrate the capability of the modified DPFT model using the simplest multi-component system composed of a gold slab in contact with a silver slab.

2.2. The DPFT framework in its basic version

2.2.1. The free energy functional for the grand canonical system

The model system considered here consists of a metal electrode and an electrolyte solution. The metal electrode contains cationic cores (denoted by cc in variable subscripts) and valence electrons (subscript, e). The electrolyte solution contains cations (subscript, c), anions (subscript, a), and solvent molecules (subscript, s). Electrons will be described at the quantum-mechanical level, while other particles will be treated at the mean-field level as classical charged particles that interact with each other via electrostatic forces and hard-sphere repulsion. Correlation effects such as those considered in ref. [139] are not accounted for in the present treatment.

Minimization of the grand potential functional, Ω, of the system gives the equilibrium profiles of variables, namely, electric potential, ϕ, electron density, n_{e}, and number density of solution species, n_{l}, where $\mathrm{l} = \mathrm{c, a, s}$ for cation, anion, and solvent.
The expression for Ω is given by,

$$\Omega = \int \left(f_{\mathrm{Q}} + f_{\mathrm{C}} + f_{\mathrm{int}} - n_{\mathrm{e}}\tilde{\mu}_{\mathrm{e}} - \sum_{\mathrm{l=c,a,s}} n_{\mathrm{l}}\,\tilde{\mu}_{\mathrm{l}} \right) \mathrm{d}^3 r. \tag{2}$$

The volumetric grand potential g of the system is written as,

$$g = f_{\mathrm{Q}} + f_{\mathrm{C}} + f_{\mathrm{int}} - n_{\mathrm{e}}\tilde{\mu}_{\mathrm{e}} - \sum_{\mathrm{l=c,a,s}} n_{\mathrm{l}}\,\tilde{\mu}_{\mathrm{l}}, \tag{3}$$

where f_{Q} and f_{C} are Helmholtz free energies of metal electrons and of solution species, respectively, formulated by quantum-mechanical DFT and classical statistical field theory, and f_{int} describes interactions between the metal electrons and the solution species, with the volumetric densities of which are denoted by n_{e} and n_{l}, respectively. $\tilde{\mu}_{\mathrm{e}}$ and $\tilde{\mu}_{\mathrm{l}}$ are the corresponding electrochemical potentials. The last two terms in Eqn. (3) ensures that the system under consideration satisfies the grand-canonical condition, connected with an electron reservoir on one side and an electrolyte solution on the other side.

The electronic contribution, f_{Q} is described by the theory of inhomogeneous electron gas [140]. Following the Kohn–Sham formalism [141,142], F_{Q} is written as,

$$f_{\mathrm{Q}} = t_{\mathrm{ni}}[n_{\mathrm{e}}, \nabla n_{\mathrm{e}}] + u_{\mathrm{X}}[n_{\mathrm{e}}, \nabla n_{\mathrm{e}}] + u_{\mathrm{C}}[n_{\mathrm{e}}, \nabla n_{\mathrm{e}}] + p_{\mathrm{cc}}[n_{\mathrm{e}}], \tag{4}$$

where $t_{\mathrm{ni}}[n_{\mathrm{e}}, \nabla n_{\mathrm{e}}]$ is the kinetic energy of non-interacting (subscript “ni”) electrons, $u_{\mathrm{X}}[n_{\mathrm{e}}, \nabla n_{\mathrm{e}}]$ and $u_{\mathrm{C}}[n_{\mathrm{e}}, \nabla n_{\mathrm{e}}]$ are the exchange and correlation energies, and $p_{\mathrm{cc}}[n_{\mathrm{e}}]$ is the pseudopotential energy that effectively captures the influence of metal cationic cores on valence electrons.

The kinetic energy term, t_{ni}, is described by the Thomas–Fermi–von Weizsäcker theory [136,137,140],

$$t_{\mathrm{ni}} = e_{\mathrm{au}} a_0^{-3} t_{\mathrm{TF}} (1 + \theta_{\mathrm{T}} s^2), \tag{5}$$

where t_{ni} is the volumetric kinetic energy given by the Thomas–Fermi theory, $t_{\mathrm{TF}} = \frac{3}{10}(3\pi^2)^{\frac{2}{3}}(n_{\mathrm{e}} a_0^3)^{\frac{5}{3}}$, $(1 + \theta_{\mathrm{T}} s^2)$ represents the correction for gradient terms, $s = |\nabla n_{\mathrm{e}}| / (2(3\pi^2)^{\frac{1}{3}}(n_{\mathrm{e}})^{\frac{4}{3}})$ is the reduced gradient term, θ_T is a coefficient controlling the contribution of the gradient term. The term $e_{\mathrm{au}} a_0^{-3}$ is used to transform the expression from atomic units to SI units, with $e_{\mathrm{au}} = e_0^2 / (4\pi\epsilon_0 a_0)$ the atomic energy, a_0 the Bohr radius, e_0 the unit of electrical charge, and ϵ_0 the vacuum permittivity.

The exchange term, u_{X}, is expanded as,

$$u_{\mathrm{X}} = e_{\mathrm{au}} a_0^{-3} u_{\mathrm{X}}^0 (1 + \theta_{\mathrm{X}} s^2), \tag{6}$$

with $u_{\mathrm{X}}^0 = -\frac{3}{4}\left(\frac{3}{\pi}\right)^{\frac{1}{3}}(n_{\mathrm{e}} a_0^3)^{\frac{4}{3}}$ the volumetric exchange energy of a uniform electron gas. The coefficient θ_{X} controls the contribution of the gradient term in the exchange energy.

The correlation term, u_{C}, is expanded as

$$u_{\mathrm{C}} = e_{\mathrm{au}} a_0^{-3} (u_{\mathrm{C}}^0 + \theta_{\mathrm{C}} n_{\mathrm{e}} a_0^3 t^2), \tag{7}$$

where $t = a_0^4 |\nabla n_\mathrm{e}| / \left(4 \left(\frac{3}{\pi}\right)^{\frac{1}{6}} (n_\mathrm{e} a_0^3)^{\frac{7}{6}} \right)$ is another reduced density gradient, and u_C^0 is the volumetric correlation energy of a uniform electron gas [142],

$$u_\mathrm{C}^0 = -2\alpha_1 n_e a_0^3 (1 + \alpha_2 r_s) \ln\left(1 + \frac{1}{\xi}\right),$$

$$r_s = \left(\frac{3}{4\pi n_\mathrm{e} a_0^3}\right)^{\frac{1}{3}}, \tag{8}$$

$$\xi = 2\alpha_1 \left(\alpha_3 r_\mathrm{s}^{\frac{1}{2}} + \alpha_4 r_\mathrm{s} + \alpha_5 r_\mathrm{s}^{\frac{3}{2}} + \alpha_6 r_\mathrm{s}^2 \right),$$

with $\alpha_1 = 0.0310907$, $\alpha_2 = 0.21370$, $\alpha_3 = 7.5957$, $\alpha_4 = 3.5876$, $\alpha_5 = 1.6382$ and $\alpha_6 = 0.49294$.

The pseudopotential energy is written as

$$p_\mathrm{cc} = e_\mathrm{au} a_0^{-3} v_\mathrm{cc}(n_\mathrm{e} a_0^3) = e_\mathrm{au} v_\mathrm{cc} n_\mathrm{e}, \tag{9}$$

where v_cc is the pseudopotential in atomic units.

The interaction contribution, f_int, captures specific interactions between metal electrons and solution particles ($\mathrm{l} = \mathrm{c, a, s}$), which can be formally written as

$$f_\mathrm{int} = \sum_{\mathrm{l=c,a,s}} n_\mathrm{l} w_\mathrm{l}(r),$$

$$w_\mathrm{l}(r) = D_\mathrm{l}\big(\exp\big(-2\beta_\mathrm{l}(d(r) - d_\mathrm{l})\big) - 2\exp\big(-\beta_\mathrm{l}(d(r) - d_\mathrm{l})\big)\big). \tag{10}$$

Here, w_l takes on a form of the Morse potential with D_l being the potential well depth, β_l a coefficient tuning the well width, d the distance to the metal surface, d_l the equilibrium distance between the particle and the metal surface. For the position within the metal, $d(r)$ is negative and $w_\mathrm{l}(r)$ becomes very positive, meaning that solution particles have a negligible probability inside the metal skeleton. Depending on the system of interest, other types of interactions could, in principle, be employed.

The classical free energy contribution, f_C, is given by,

$$
\begin{aligned}
f_{\mathrm{C}} = &-\frac{1}{2}\epsilon_{\mathrm{opt}}(\nabla\phi)^2 + \sum_{\mathrm{l=c,a}} n_{\mathrm{l}}q_{\mathrm{l}}\,\phi - n_{\mathrm{s}}\beta^{-1}\ln\left(\frac{\sinh(\beta|\vec{p}||\nabla\phi|)}{\beta|\vec{p}||\nabla\phi|}\right) \\
&+ \sum_{\mathrm{l=c,a}} \beta^{-1}\left(n_{\mathrm{l}}\ln\left(n_{\mathrm{l}}\Lambda_{\mathrm{l}}^3\right) - n_{\mathrm{l}}\right) + \Phi_{\mathrm{ex}}(\{n_{\mathrm{l}}\}) + (n_{\mathrm{cc}} - n_{\mathrm{e}})e_0\phi.
\end{aligned}
\tag{11}
$$

Here, the first term on the right-hand side is the self-energy of the electric field, with optical permittivity, ϵ_{opt}, and the electric potential, ϕ. The optical permittivity, ϵ_{opt}, typically varies from the electrode region to the electrolyte domain. The second and third terms represent the potential energies of charged particles and dipolar solvents in solution, with $\beta = (k_{\mathrm{B}}T)^{-1}$ the inverse thermal energy. The fourth term represents the Gibbs free energy of an ideal-gas reference system, where Λ_{l} is the thermal wavelength of particle l. The fifth term $\Phi_{\mathrm{ex}}(\{n_{\mathrm{l}}\})$ accounts for the excess Gibbs free energy of the studied system compared with the ideal gas system, which accounts for finite-size effects, etc. Φ_{ex} can be calculated using various methods, as summarized in Ref. [96]. The sixth term represents the Hartree energy of electrons and cationic cores of the electrode.

Combined, the volumetric grand potential g of the EDL can be written as,

$$
\begin{aligned}
g = {} & e_{\mathrm{au}}a_0^{-3}\left(t_{\mathrm{TF}}(1+\theta_{\mathrm{T}}s^2) + u_{\mathrm{X}}^0(1+\theta_{\mathrm{X}}s^2) + u_{\mathrm{C}}^0 + \theta_{\mathrm{C}}n_{\mathrm{e}}a_0^3t^2 + v_{\mathrm{cc}}n_{\mathrm{e}}a_0^3\right) \\
&-\frac{1}{2}\epsilon_{\mathrm{opt}}(\nabla\phi)^2 + \sum_{\mathrm{l=c,a,s}} n_{\mathrm{l}}w_{\mathrm{l}}(r) + \sum_{\mathrm{l=c,a}} n_{\mathrm{l}}q_{\mathrm{l}}\phi \\
&- n_{\mathrm{s}}\beta^{-1}\ln\left(\frac{\sinh(\beta|\vec{p}||\nabla\phi|)}{\beta|\vec{p}||\nabla\phi|}\right) + \sum_{\mathrm{l=c,a}} \beta^{-1}\left(n_{\mathrm{l}}\ln\left(n_{\mathrm{l}}\Lambda_{\mathrm{l}}^3\right) - n_{\mathrm{l}}\right) \\
&+ \Phi_{\mathrm{ex}}(\{n_{\mathrm{l}}\}) + (n_{\mathrm{cc}} - n_{\mathrm{e}})e_0\phi - n_{\mathrm{e}}\tilde{\mu}_{\mathrm{e}} - \sum_{\mathrm{l=c,a}} n_{\mathrm{l}}\tilde{\mu}_{\mathrm{l}}.
\end{aligned}
\tag{12}
$$

2.2.2. Controlling equations

The grand potential functional $\Omega = \int g\,\mathrm{d}^3r$ reaches its minimum under thermodynamic equilibrium, from which the controlling equations can be obtained through the Euler–Lagrange equation $\frac{\partial g}{\partial\phi} - \nabla\cdot\left(\frac{\partial g}{\partial(\nabla\phi)}\right) = 0$. Accordingly, the controlling equation for the electric potential can be obtained as

$$-\nabla\cdot(\epsilon_{\mathrm{eff}}\nabla\phi)=e_0(n_{\mathrm{cc}}-n_{\mathrm{e}})+e_0(n_{\mathrm{c}}-n_{\mathrm{a}}), \tag{13}$$

with $\mathcal{L}(x)=\coth(x)-\frac{1}{x}$ being the Langevin function and ϵ_{eff} given by

$$\epsilon_{\mathrm{eff}}=\epsilon_{\mathrm{opt}}+n_{\mathrm{s}}|\vec{p}|\frac{\mathcal{L}(\beta|\vec{p}||\nabla\phi|)}{|\nabla\phi|}. \tag{14}$$

For the number density distribution of charged particles and dipolar solvent molecules in the electrolyte solution, applying $\frac{\partial g}{\partial n_{\mathrm{l}}}-\nabla\cdot\left(\frac{\partial g}{\partial(\nabla n_{\mathrm{l}})}\right)=0$ results in

$$w_{\mathrm{l}}+\delta(\mathrm{l}\in\mathrm{M})q_{\mathrm{l}}\phi-\delta(\mathrm{l}\in\mathrm{S})\beta^{-1}\ln\left(\frac{\sinh(\beta|\vec{p}||\nabla\phi|)}{\beta|\vec{p}||\nabla\phi|}\right)+\beta^{-1}\ln n_{\mathrm{l}}\Lambda_{\mathrm{l}}^{3}+\mu_{\mathrm{l}}^{\mathrm{ex}}-\tilde{\mu}_{\mathrm{l}}=0, \tag{15}$$

The symbol $\delta(\mathrm{l}\in\mathrm{M})$ is equal to one for monopolar charged particles (M), *e.g.*, cations and anions, and zero otherwise. $\delta(\mathrm{l}\in\mathrm{S})$ is equal to one for dipolar solvent molecules (S) and zero otherwise.

The excess chemical potential, $\mu_{\mathrm{l}}^{\mathrm{ex}}$, is given by

$$\mu_{\mathrm{l}}^{\mathrm{ex}}=\frac{\partial\Phi_{\mathrm{ex}}}{\partial n_{\mathrm{l}}}-\nabla\cdot\left(\frac{\partial\Phi_{\mathrm{ex}}}{\partial(\nabla n_{\mathrm{l}})}\right). \tag{16}$$

In this work, the excess term Φ_{ex} is described by the Huang model, which calculates the mixing entropy of the electrolyte solution, considering the relative size γ_{c} for cations, γ_{a} for anions, and γ_{s} for solvents [96]. The reference size can be arbitrarily chosen and does not affect the final expression of the ion number density. In this work, the size of a solvent molecule is chosen as the reference, *i.e.*, $\gamma_{\mathrm{s}}=1$. The volumetric number density of the total lattice sites is denoted as n_{site}. The model gives,

$$\begin{aligned}\mu_{\mathrm{c}}^{\mathrm{ex}}&=\beta^{-1}\ln\frac{n_{\mathrm{site}}}{(n_{\mathrm{site}}-\gamma_{\mathrm{c}}n_{\mathrm{c}}-\gamma_{\mathrm{a}}n_{\mathrm{a}}-\gamma_{\mathrm{s}}n_{\mathrm{s}})^{\gamma_{\mathrm{c}}}},\\ \mu_{\mathrm{a}}^{\mathrm{ex}}&=\beta^{-1}\ln\frac{n_{\mathrm{site}}}{(n_{\mathrm{site}}-\gamma_{\mathrm{c}}n_{\mathrm{c}}-\gamma_{\mathrm{a}}n_{\mathrm{a}}-\gamma_{\mathrm{s}}n_{\mathrm{s}})^{\gamma_{\mathrm{a}}}},\end{aligned} \tag{17}$$

$$\mu_{\mathrm{s}}^{\mathrm{ex}} = \beta^{-1} \ln \frac{n_{\mathrm{site}}}{(n_{\mathrm{site}} - \gamma_{\mathrm{c}} n_{\mathrm{c}} - \gamma_{\mathrm{a}} n_{\mathrm{a}} - \gamma_{\mathrm{s}} n_{\mathrm{s}})^{\gamma_{\mathrm{s}}}}.$$

With detailed derivations to be found in Eqn. (9-12) in Ref. [96]. Substituting Eqn. (17) to Eqn. (15), assuming $q_{\mathrm{c}} = e$ and $q_{\mathrm{a}} = -e$, and applying a few rearrangements arrives at

$$\begin{aligned}
\exp(\beta\tilde{\mu}_{\mathrm{c}}) &= \Lambda_{\mathrm{c}}^{3} \frac{n_{\mathrm{site}} n_{\mathrm{c}}}{(n_{\mathrm{site}} - \gamma_{\mathrm{c}} n_{\mathrm{c}} - \gamma_{\mathrm{a}} n_{\mathrm{a}} - \gamma_{\mathrm{s}} n_{\mathrm{s}})^{\gamma_{\mathrm{c}}}} \exp\big(\beta(w_{\mathrm{c}} + e\phi)\big), \\
\exp(\beta\tilde{\mu}_{\mathrm{a}}) &= \Lambda_{\mathrm{a}}^{3} \frac{n_{\mathrm{site}} n_{\mathrm{a}}}{(n_{\mathrm{site}} - \gamma_{\mathrm{c}} n_{\mathrm{c}} - \gamma_{\mathrm{a}} n_{\mathrm{a}} - \gamma_{\mathrm{s}} n_{\mathrm{s}})^{\gamma_{\mathrm{a}}}} \exp\big(\beta(w_{\mathrm{a}} - e\phi)\big), \qquad (18) \\
\exp(\beta\tilde{\mu}_{\mathrm{s}}) &= \Lambda_{\mathrm{s}}^{3} \frac{n_{\mathrm{site}} n_{\mathrm{s}}}{(n_{\mathrm{site}} - \gamma_{\mathrm{c}} n_{\mathrm{c}} - \gamma_{\mathrm{a}} n_{\mathrm{a}} - \gamma_{\mathrm{s}} n_{\mathrm{s}})^{\gamma_{\mathrm{s}}}} \exp(\beta w_{\mathrm{s}}) \frac{\beta|\vec{p}||\nabla\phi|}{\sinh(\beta|\vec{p}||\nabla\phi|)}.
\end{aligned}$$

The above equation should be valid everywhere in the system, including the solution bulk where $w_{\mathrm{c}} = w_{\mathrm{a}} = w_{\mathrm{s}} = 0$ and $\phi = \nabla\phi = 0$, and, therefore,

$$\begin{aligned}
\exp\big(\beta\tilde{\mu}_{\mathrm{c}}^{\mathrm{b}}\big) &= \Lambda_{\mathrm{c}}^{3} \frac{n_{\mathrm{site}} n_{\mathrm{c}}^{\mathrm{b}}}{\big(n_{\mathrm{site}} - \gamma_{\mathrm{c}} n_{\mathrm{c}}^{\mathrm{b}} - \gamma_{\mathrm{a}} n_{\mathrm{a}}^{\mathrm{b}} - \gamma_{\mathrm{s}} n_{\mathrm{s}}^{\mathrm{b}}\big)^{\gamma_{\mathrm{c}}}}, \\
\exp\big(\beta\tilde{\mu}_{\mathrm{a}}^{\mathrm{b}}\big) &= \Lambda_{\mathrm{a}}^{3} \frac{n_{\mathrm{site}} n_{\mathrm{a}}^{\mathrm{b}}}{\big(n_{\mathrm{site}} - \gamma_{\mathrm{c}} n_{\mathrm{c}}^{\mathrm{b}} - \gamma_{\mathrm{a}} n_{\mathrm{a}}^{\mathrm{b}} - \gamma_{\mathrm{s}} n_{\mathrm{s}}^{\mathrm{b}}\big)^{\gamma_{\mathrm{a}}}}, \qquad (19) \\
\exp\big(\beta\tilde{\mu}_{\mathrm{s}}^{\mathrm{b}}\big) &= \Lambda_{\mathrm{s}}^{3} \frac{n_{\mathrm{site}} n_{\mathrm{s}}^{\mathrm{b}}}{\big(n_{\mathrm{site}} - \gamma_{\mathrm{c}} n_{\mathrm{c}}^{\mathrm{b}} - \gamma_{\mathrm{a}} n_{\mathrm{a}}^{\mathrm{b}} - \gamma_{\mathrm{s}} n_{\mathrm{s}}^{\mathrm{b}}\big)^{\gamma_{\mathrm{s}}}}.
\end{aligned}$$

Since in equilibrium, $\tilde{\mu}_{\mathrm{l}}$ should remain constant everywhere in the system, i.e., $\tilde{\mu}_{\mathrm{c}} = \tilde{\mu}_{\mathrm{c}}^{\mathrm{b}}$, $\tilde{\mu}_{\mathrm{a}} = \tilde{\mu}_{\mathrm{a}}^{\mathrm{b}}$, and $\tilde{\mu}_{\mathrm{s}} = \tilde{\mu}_{\mathrm{s}}^{\mathrm{b}}$, one can equate Eqns. (18) and (19) and obtain,

$$\frac{n_{\mathrm{c}}}{(n_{\mathrm{site}} - \gamma_{\mathrm{c}} n_{\mathrm{c}} - \gamma_{\mathrm{a}} n_{\mathrm{a}} - \gamma_{\mathrm{s}} n_{\mathrm{s}})^{\gamma_{\mathrm{c}}}} \exp\big(\beta(w_{\mathrm{c}} + e\phi)\big) = \frac{n_{\mathrm{c}}^{\mathrm{b}}}{\big(n_{\mathrm{site}} - \gamma_{\mathrm{c}} n_{\mathrm{c}}^{\mathrm{b}} - \gamma_{\mathrm{a}} n_{\mathrm{a}}^{\mathrm{b}} - \gamma_{\mathrm{s}} n_{\mathrm{s}}^{\mathrm{b}}\big)^{\gamma_{\mathrm{c}}}}, \qquad (20)$$

$$\frac{n_{\mathrm{a}}}{(n_{\mathrm{site}} - \gamma_{\mathrm{c}} n_{\mathrm{c}} - \gamma_{\mathrm{a}} n_{\mathrm{a}} - \gamma_{\mathrm{s}} n_{\mathrm{s}})^{\gamma_{\mathrm{a}}}} \exp\big(\beta(w_{\mathrm{a}} - e\phi)\big) = \frac{n_{\mathrm{a}}^{\mathrm{b}}}{\big(n_{\mathrm{site}} - \gamma_{\mathrm{c}} n_{\mathrm{c}}^{\mathrm{b}} - \gamma_{\mathrm{a}} n_{\mathrm{a}}^{\mathrm{b}} - \gamma_{\mathrm{s}} n_{\mathrm{s}}^{\mathrm{b}}\big)^{\gamma_{\mathrm{a}}}}, \qquad (21)$$

$$\frac{n_\mathrm{s}}{(n_\mathrm{site}-\gamma_\mathrm{c}n_\mathrm{c}-\gamma_\mathrm{a}n_\mathrm{a}-\gamma_\mathrm{s}n_\mathrm{s})^{\gamma_\mathrm{s}}}\exp(\beta w_\mathrm{s})\frac{\beta|\vec{p}||\nabla\phi|}{\sinh(\beta|\vec{p}||\nabla\phi|)}=\frac{n_\mathrm{s}^\mathrm{b}}{\left(n_\mathrm{site}-\gamma_\mathrm{c}n_\mathrm{c}^\mathrm{b}-\gamma_\mathrm{a}n_\mathrm{a}^\mathrm{b}-\gamma_\mathrm{s}n_\mathrm{s}^\mathrm{b}\right)^{\gamma_\mathrm{s}}} \quad (22)$$

If one approximates γ_c, γ_a and γ_s in the exponents of Eqn. (20) to (22) to be 1, one would obtain a set of linear equations of variables n_c, n_a and n_s.

$$\frac{n_\mathrm{c}}{n_\mathrm{site}-\gamma_\mathrm{c}n_\mathrm{c}-\gamma_\mathrm{a}n_\mathrm{a}-\gamma_\mathrm{s}n_\mathrm{s}}\exp\big(\beta(w_\mathrm{c}+e\phi)\big)=\frac{n_\mathrm{c}^\mathrm{b}}{n_\mathrm{site}-\gamma_\mathrm{c}n_\mathrm{c}^\mathrm{b}-\gamma_\mathrm{a}n_\mathrm{a}^\mathrm{b}-\gamma_\mathrm{s}n_\mathrm{s}^\mathrm{b}}, \quad (23)$$

$$\frac{n_\mathrm{a}}{n_\mathrm{site}-\gamma_\mathrm{c}n_\mathrm{c}-\gamma_\mathrm{a}n_\mathrm{a}-\gamma_\mathrm{s}n_\mathrm{s}}\exp\big(\beta(w_\mathrm{a}-e\phi)\big)=\frac{n_\mathrm{a}^\mathrm{b}}{n_\mathrm{site}-\gamma_\mathrm{c}n_\mathrm{c}^\mathrm{b}-\gamma_\mathrm{a}n_\mathrm{a}^\mathrm{b}-\gamma_\mathrm{s}n_\mathrm{s}^\mathrm{b}}, \quad (24)$$

$$\frac{n_\mathrm{s}}{n_\mathrm{site}-\gamma_\mathrm{c}n_\mathrm{c}-\gamma_\mathrm{a}n_\mathrm{a}-\gamma_\mathrm{s}n_\mathrm{s}}\exp(\beta w_\mathrm{s})\frac{\beta|\vec{p}||\nabla\phi|}{\sinh(\beta|\vec{p}||\nabla\phi|)}=\frac{n_\mathrm{s}^\mathrm{b}}{n_\mathrm{site}-\gamma_\mathrm{c}n_\mathrm{c}^\mathrm{b}-\gamma_\mathrm{a}n_\mathrm{a}^\mathrm{b}-\gamma_\mathrm{s}n_\mathrm{s}^\mathrm{b}}. \quad (25)$$

This set of linear equations can be solved in the following way. Dividing Eqn. (23) by Eqn. (24) gives the ratio $n_\mathrm{c}/\mathrm{n_a}$. Similarly, dividing Eqn. (23) by Eqn. (25) yields $n_\mathrm{c}/n_\mathrm{s}$. These two ratios allow expressing n_a and n_s in terms of n_c. Substituting these expressions back into Eqn. (23), n_c can be solved for. Then, using the ratios $n_\mathrm{c}/n_\mathrm{a}$ and $n_\mathrm{c}/n_\mathrm{s}$ yields n_a and n_s.

The final expressions for n_c, n_a and n_s are

$$\frac{n_\mathrm{c}}{n_\mathrm{site}}=\frac{n_\mathrm{c}^\mathrm{b}\exp[-\beta(w_\mathrm{c}+e\phi)]}{\gamma_\mathrm{c}n_\mathrm{c}^\mathrm{b}\exp[-\beta(w_\mathrm{c}+e\phi)]+\gamma_\mathrm{a}n_\mathrm{a}^\mathrm{b}\exp[-\beta(w_\mathrm{a}-e\phi)]+\gamma_\mathrm{s}n_\mathrm{s}^\mathrm{b}\frac{\sinh(\beta|\vec{p}||\nabla\phi|)}{\beta|\vec{p}||\nabla\phi|}+n_\mathrm{site}-\gamma_\mathrm{c}n_\mathrm{c}^\mathrm{b}-\gamma_\mathrm{a}n_\mathrm{a}^\mathrm{b}-\gamma_\mathrm{s}n_\mathrm{s}^\mathrm{b}}, \quad (26)$$

$$\frac{n_\mathrm{a}}{n_\mathrm{site}}=\frac{n_\mathrm{a}^\mathrm{b}\exp[-\beta(w_\mathrm{a}-e\phi)]}{\gamma_\mathrm{c}n_\mathrm{c}^\mathrm{b}\exp[-\beta(w_\mathrm{c}+e\phi)]+\gamma_\mathrm{a}n_\mathrm{a}^\mathrm{b}\exp[-\beta(w_\mathrm{a}-e\phi)]+\gamma_\mathrm{s}n_\mathrm{s}^\mathrm{b}\frac{\sinh(\beta|\vec{p}||\nabla\phi|)}{\beta|\vec{p}||\nabla\phi|}+n_\mathrm{site}-\gamma_\mathrm{c}n_\mathrm{c}^\mathrm{b}-\gamma_\mathrm{a}n_\mathrm{a}^\mathrm{b}-\gamma_\mathrm{s}n_\mathrm{s}^\mathrm{b}}, \quad (27)$$

$$\frac{n_\mathrm{s}}{n_\mathrm{site}}=\frac{n_\mathrm{s}^\mathrm{b}\exp(-\beta w_\mathrm{s})\frac{\sinh(\beta|\vec{p}||\nabla\phi|)}{\beta|\vec{p}||\nabla\phi|}}{\gamma_\mathrm{c}n_\mathrm{c}^\mathrm{b}\exp[-\beta(w_\mathrm{c}+e\phi)]+\gamma_\mathrm{a}n_\mathrm{a}^\mathrm{b}\exp[-\beta(w_\mathrm{a}-e\phi)]+\gamma_\mathrm{s}n_\mathrm{s}^\mathrm{b}\frac{\sinh(\beta|\vec{p}||\nabla\phi|)}{\beta|\vec{p}||\nabla\phi|}+n_\mathrm{site}-\gamma_\mathrm{c}n_\mathrm{c}^\mathrm{b}-\gamma_\mathrm{a}n_\mathrm{a}^\mathrm{b}-\gamma_\mathrm{s}n_\mathrm{s}^\mathrm{b}}. \quad (28)$$

For the distribution of electrons, applying $\frac{\partial g}{\partial n_\mathrm{e}}-\nabla\cdot\left(\frac{\partial g}{\partial(\nabla n_\mathrm{e})}\right)=0$ results in

$$\nabla\cdot\left[\frac{\partial(t_{\mathrm{ni}}+u_{\mathrm{x}}+u_{\mathrm{c}}+p_{\mathrm{cc}})}{\partial\nabla n_{\mathrm{e}}}\right]=\frac{\partial(t_{\mathrm{ni}}+u_{\mathrm{x}}+u_{\mathrm{c}}+p_{\mathrm{cc}})}{\partial n_{\mathrm{e}}}-e_0\phi-\tilde{\mu}_{\mathrm{e}}. \tag{29}$$

Eqn. (29) needs to be further manipulated to be actually solved numerically. Firstly, it is rewritten using the dimensionless electron density, $\bar{n}_{\mathrm{e}}=n_{\mathrm{e}}a_0^3$, with a_0 the Bohr radius,

$$\bar{\nabla}\cdot\left[\frac{\partial(t_{\mathrm{ni}}+u_{\mathrm{x}}+u_{\mathrm{c}}+p_{\mathrm{cc}})}{\partial\bar{\nabla}\bar{n}_{\mathrm{e}}}\right]=\frac{\partial(t_{\mathrm{ni}}+u_{\mathrm{x}}+u_{\mathrm{c}}+p_{\mathrm{cc}})}{\partial\bar{n}_{\mathrm{e}}}-a_0^{-3}(e_0\phi+\tilde{\mu}_{\mathrm{e}}). \tag{30}$$

The term inside the bracket at the left-hand-side can be written as

$$\frac{\partial(t_{\mathrm{ni}}+u_{\mathrm{x}}+u_{\mathrm{c}}+p_{\mathrm{cc}})}{\partial\bar{\nabla}\bar{n}_{\mathrm{e}}}=\frac{e_{\mathrm{au}}a_0^{-3}\left(\theta_{\mathrm{T}}t_{\mathrm{TF}}+\theta_{\mathrm{XC}}u_{\mathrm{X}}^0\right)}{2(3\pi^2)^{\frac{2}{3}}(\bar{n}_{\mathrm{e}})^{\frac{8}{3}}}\bar{\nabla}\bar{n}_{\mathrm{e}}, \tag{31}$$

with $\theta_{\mathrm{XC}}=\theta_{\mathrm{X}}-\frac{\pi^2}{3}\theta_{\mathrm{C}}$.

The term at the right-hand-side can be written as

$$\frac{\partial(t_{\mathrm{ni}}+u_{\mathrm{x}}+u_{\mathrm{c}}+p_{\mathrm{cc}})}{\partial\bar{n}_{\mathrm{e}}}=e_{\mathrm{au}}a_0^{-3}\left[(1+\theta_{\mathrm{T}}s^2)\frac{\partial t_{\mathrm{TF}}}{\partial\bar{n}_{\mathrm{e}}}+(1+\theta_{\mathrm{XC}}s^2)\frac{\partial u_{\mathrm{X}}^0}{\partial\bar{n}_{\mathrm{e}}}+\frac{\partial u_{\mathrm{C}}^0}{\partial\bar{n}_{\mathrm{e}}}+(\theta_{\mathrm{T}}t_{\mathrm{TF}}+\theta_{\mathrm{X}}u_{\mathrm{X}}^0)\frac{\partial s^2}{\partial\bar{n}_{\mathrm{e}}}+v_{\mathrm{cc}}\right], \tag{32}$$

with

$$\frac{\partial t_{\mathrm{TF}}}{\partial\bar{n}_{\mathrm{e}}}=\frac{1}{2}(3\pi^2\bar{n}_{\mathrm{e}})^{\frac{2}{3}}, \tag{33}$$

$$\frac{\partial s^2}{\partial\bar{n}_{\mathrm{e}}}=-\frac{8}{3\bar{n}_{\mathrm{e}}}s^2, \tag{34}$$

$$\frac{\partial u_{\mathrm{X}}^0}{\partial\bar{n}_{\mathrm{e}}}=-\left(\frac{3}{\pi}\bar{n}_{\mathrm{e}}\right)^{\frac{1}{3}}, \tag{35}$$

$$\frac{\partial u_{\mathrm{C}}^{0}}{\partial \bar{n}_{\mathrm{e}}} = -2\alpha_1(1+\alpha_2 r_{\mathrm{s}})\ln\left(1+\frac{1}{\xi}\right) + \frac{2\alpha_1 r_{\mathrm{s}}}{3}\left(\alpha_2 \ln\left(1+\frac{1}{\xi}\right) - \frac{\alpha_1(1+\alpha_2 r_{\mathrm{s}})}{\xi(1+\xi)}\left(\alpha_3 r_{\mathrm{s}}^{-\frac{1}{2}} + 2\alpha_4 + 3\alpha_5 r_{\mathrm{s}}^{\frac{1}{2}} + 4\alpha_6 r_{\mathrm{s}}\right)\right). \tag{36}$$

After a few arrangements (detailed in the supporting information S34-S37 of Ref [111]), the controlling equation for the electron density is reformulated as,

$$\bar{\nabla}^2 \bar{n}_{\mathrm{e}} = \frac{20}{3}\bar{n}_{\mathrm{e}}\frac{\omega}{\theta_{\mathrm{T}}\omega - \theta_{\mathrm{XC}}}\left(\frac{\partial t_{\mathrm{TF}}}{\partial \bar{n}_{\mathrm{e}}} + \frac{\partial u_{\mathrm{X}}^{0}}{\partial \bar{n}_{\mathrm{e}}} + \frac{\partial u_{\mathrm{C}}^{0}}{\partial \bar{n}_{\mathrm{e}}} + v_{\mathrm{cc}} - \frac{e_0\phi + \tilde{\mu}_{\mathrm{e}}}{e_{\mathrm{au}}}\right) + \frac{\theta_{\mathrm{T}}\omega - \frac{4}{3}\theta_{\mathrm{XC}}}{2\bar{n}_{\mathrm{e}}(\theta_{\mathrm{T}}\omega - \theta_{\mathrm{XC}})}(\bar{\nabla}\bar{n}_{\mathrm{e}})^2, \tag{37}$$

with $\omega = \frac{2}{5}\pi^{5/3}3^{1/3}\bar{n}_{\mathrm{e}}^{1/3}$.

For better numerical convergence, $\psi = (\bar{n}_{\mathrm{e}})^{1/3}$ rather than $\bar{n}_{\mathrm{e}}$ is solved for. In this way, the issues related to fractional exponents of $\bar{n}_{\mathrm{e}}$ is bypassed. With $\bar{\nabla}\bar{n}_{\mathrm{e}} = \bar{\nabla}\psi^3 = 3\psi^2\bar{\nabla}\psi$ and $\bar{\nabla}^2\bar{n}_{\mathrm{e}} = 3\psi^2\bar{\nabla}\bar{\nabla}\psi + 6\psi(\bar{\nabla}\psi)^2$, Eqn. (37) is transformed to

$$\bar{\nabla}^2\psi = -\frac{\pi^{\frac{5}{3}}3^{\frac{1}{3}}\theta_{\mathrm{T}}}{5(\theta_{\mathrm{T}}\omega - \theta_{\mathrm{XC}})}(\bar{\nabla}\psi)^2 + \frac{20}{9}\psi\frac{\omega}{\theta_{\mathrm{T}}\omega - \theta_{\mathrm{XC}}}\left(\frac{\partial t_{\mathrm{TF}}}{\partial \bar{n}_{\mathrm{e}}} + \frac{\partial u_{\mathrm{X}}^{0}}{\partial \bar{n}_{\mathrm{e}}} + \frac{\partial u_{\mathrm{C}}^{0}}{\partial \bar{n}_{\mathrm{e}}} + v_{\mathrm{cc}} - \frac{e_0\phi + \tilde{\mu}_{\mathrm{e}}}{e_{\mathrm{au}}}\right). \tag{38}$$

in which the $\bar{n}_{\mathrm{e}}^{\frac{2}{3}}$ and $\bar{n}_{\mathrm{e}}^{\frac{1}{3}}$ in the expression of $\frac{\partial t_{\mathrm{TF}}}{\partial \bar{n}_{\mathrm{e}}}$ and $\frac{\partial u_{\mathrm{X}}^{0}}{\partial \bar{n}_{\mathrm{e}}}$ can be replaced with ψ^2 and ψ, respectively.

2.3. Extension of the DPFT framework

2.3.1. Metal–water interactions

It has long been realized that the electronic work function of a metal, Φ, is reduced when it is immersed in a liquid phase [143,144]. The reduction can be envisaged as the sum of two contributions, $\delta\chi_{\mathrm{ori}}$ and $\delta\chi_{\mathrm{e}}$, where $\delta\chi_{\mathrm{ori}}$ arises from the change in water dipole orientation due to interactions with the metal surface and $\delta\chi_{\mathrm{e}}$ originates from the perturbation of the electron density distribution at the metal surface due to the presence of water.

For the last twenty years, DFT calculations and DFT-based MD simulations (*i.e.*, *ab initio* MD simulations, AIMD) have been used to provide atomistic information of the metal–water interfaces. Based on the revealed atomistic structure of the first layer of water dipoles, they not only provided possible explanations on the physical origin of $\delta\chi_{\mathrm{e}}$, but yielded reliable estimates of the relative proportion of the two contributions $\delta\chi_{\mathrm{ori}}$ and $\delta\chi_{\mathrm{e}}$ to $\Delta\Phi$. In 2002, Ogasawara et al. used DFT calculations to demonstrate that water is adsorbed on Pt(111) in a flat layer with both metal–oxygen (M–O) and metal–hydrogen (M–HO) bonding species [145]. Charge density difference plot revealed that a depleted electron density in the Pt–O bonding region to minimize the Pauli repulsion between the lone pair orbital of O and the d orbital of Pt. Meanwhile, bonding between Pt and hydrogen results in electron accumulation. These findings are confirmed by X-ray absorption, X-ray emission, and X-ray photoelectron spectroscopy. Following Ogasawara's work, a plethora of AIMD simulations confirmed the interfacial water structure by providing density distribution of oxygen atom and angular distribution of water bisector vector and water O–H bond [76,146–150]. While the relative importance of $\delta\chi_{\mathrm{ori}}$ and $\delta\chi_{\mathrm{e}}$ remains a subject of debate, these experimental and theoretical results clearly show that metal–water specific interactions are highly important for a reliable description of EDL structures.

2.3.2. Introduction of an auxiliary field

It is generally accepted that specific interactions of an uncharged metal surface and the first layer of solvent molecules determine the interfacial potential distribution and, thereby, make additional contribution to the difference between work function and PZC, as established by experiments [151–153] and first-principles calculations [76,145,147–150,154]. A goal of the present work is to advance the DPFT framework in order to capture electrostatic interactions between spillover electrons and the first-layer water molecules. This development allows the model to describe (i) the reduction of the interfacial potential drop due to increased dielectric permittivity, and (ii) the water dipole reorientation [155–158]. Due to the orbital-free feature of DPFT, electron exchange caused by hybridization of solvent molecules and metal surface is not explicitly modelled [76,146,148]. To address this issue, a heuristic approach is adopted by introducing an auxiliary field, $\vec{A}$, which induces a net polarization in the interfacial region. $\vec{A}$ is set to be perpendicular to the surface and decay to zero within a few Angstroms from the surface. Coupled with the solvent dipole moment $\vec{p}$, $\vec{A}$ generates an additional reorientation of solvent dipoles in the first layer and, thereby, creates an interfacial polarization. This allows one to reproduce experimental PZC values via tuning the magnitude of $\vec{A}$.

The auxiliary field gives rise to a new Hamiltonian term, H_{spec}, which, together with the electrostatic term, H_{elec}, contributes to the total solvent Hamiltonian,

$$H_{\mathrm{s}} = H_{\mathrm{elec}} + H_{\mathrm{spec}}, \tag{39}$$

with H_{spec} modelled as an effective dipole–field interaction,

$$H_{\mathrm{spec}} = -\vec{p} \cdot \vec{A}, \tag{40}$$

where $\vec{p}$ points from the negatively charged oxygen atom to the positively charged hydrogen atoms. The auxiliary field $\vec{A}$ is specific to the electrode material and surface orientation. $\vec{A}$ is given by $\vec{A} = A\vec{n}$ with $\vec{n} = (n_{\mathrm{r}}, n_{\mathrm{z}})$ defined as a unit vector pointing outwards from the solid surface, and A expressed as,

$$A = \frac{A^0}{2}\left(1 + \mathrm{erf}\left(-\frac{d - L_{\mathrm{A}}}{l_{\mathrm{A}}}\right)\right), \tag{41}$$

where d is the distance to the surface, and L_{A} and l_{A} are the position and the width of the decay region, respectively. A^0, L_{A} and l_{A} can be calibrated to reproduce the experimentally measured PZC. According to this definition, a positive A^0 favors the oxygen-down orientation, with the oxygen atom located closer to the metal surface.

For the derivation of the free energy functional of solvent molecules, the total field imposed on a solvent molecule is defined as $\vec{E}_{\mathrm{tot}} = \vec{E} + \vec{A}$.

$$\vec{E}_{\mathrm{tot}} = \vec{E} + \vec{A} = (-\nabla_{\mathrm{r}}\phi + An_{\mathrm{r}}, -\nabla_{\mathrm{z}}\phi + An_{\mathrm{z}}). \tag{42}$$

H_{s} is rewritten as,

$$H_{\mathrm{s}} = -\vec{p} \cdot \vec{E}_{\mathrm{tot}} = |\vec{p}||\vec{E}_{\mathrm{tot}}| \cos\omega, \tag{43}$$

where ω is the angle between $\vec{p}$ and $-\vec{E}_{\mathrm{tot}}$.

The partition function of the solvent is

$$Q_i = \exp\left(-\frac{H_\mathrm{s}}{k_\mathrm{B}T}\right). \tag{44}$$

The average of Q_i over all possible ω is

$$\langle Q_i \rangle = \frac{\int_0^\pi \exp\left(-\frac{H_\mathrm{s}}{k_\mathrm{B}T}\right)\sin\omega\,\mathrm{d}\omega}{\int_0^\pi \sin\omega\,\mathrm{d}\omega} = \frac{\int_0^\pi \exp\left(-\frac{|\vec{p}||\vec{E}_\mathrm{tot}|\cos\omega}{k_\mathrm{B}T}\right)\sin\omega\,\mathrm{d}\omega}{2} \\ = \frac{\sinh\left(\beta|\vec{p}||\vec{E}_\mathrm{tot}|\right)}{\beta|\vec{p}||\vec{E}_\mathrm{tot}|}. \tag{45}$$

The partition function for the ensemble of solvent molecules is

$$Q_\mathrm{s} = \langle Q_i \rangle^{n_\mathrm{s}} = \left(\frac{\sinh\left(\beta|\vec{p}||\vec{E}_\mathrm{tot}|\right)}{\beta|\vec{p}||\vec{E}_\mathrm{tot}|}\right)^{n_\mathrm{s}}. \tag{46}$$

The free energy functional of solvent molecules is

$$f_\mathrm{s} = k_\mathrm{B}T\ln Q_\mathrm{s} = n_\mathrm{s}\beta^{-1}\ln\left(\frac{\sinh\left(\beta|\vec{p}||\vec{E}_\mathrm{tot}|\right)}{\beta|\vec{p}||\vec{E}_\mathrm{tot}|}\right). \tag{47}$$

In Ref. [111] and the above section “The DPFT framework in its basic version”, the local solvent concentration, $c_\mathrm{s} = n_\mathrm{s}/N_\mathrm{A}$, was allowed to change in response to the electric field. However, this treatment results in unrealistically high local concentration of water molecules and local dielectric constant in the gap region between the electrode and the first-layer ions. To mitigate this artifact, calculating c_s (or n_s) is bypassed by predefining the profile of c_s. Since the first layer of solvents is located several Angstroms away from the electrode surface, the center of the first layer of solvent molecules is set to be located at L_s. The value of c_s is kept fixed at the bulk value (55.6 mol/L) for every position within the liquid phase, with the exception of the narrow region around L_s where c_s smoothly changes from zero to the bulk value, c_s^b, to avoid running into a numerical artifact. The width of the transition region is given by l_s, which is expressed using the error function,

$$c_\mathrm{s} = \frac{c_\mathrm{s}^\mathrm{b}}{2}\left(1 - \mathrm{erf}\left(-\frac{\mathrm{z} - L_\mathrm{s}}{l_\mathrm{s}}\right)\right). \tag{48}$$

The metal–water distance L_s represents the width of the gap between the outmost atomic plane of a specific metal and the plane of the first solvent layer. Within this gap, the relative permittivity is set to $\epsilon_\mathrm{r} = 1$ corresponding to vacuum. The parameter, L_s, is closely related to PZC and C_d. It can be calibrated to reproduce experimental data of PZC and C_d.

2.3.3. Dependence of effective dipole moment on ion concentration

In this study, it is assumed that the magnitude of the effective dipole moment of water ($|\vec{p}|$) and the local ion concentrations ($c_\mathrm{c} = n_\mathrm{c}/N_\mathrm{A},\ c_\mathrm{a} = n_\mathrm{a}/N_\mathrm{A}$) are related by

$$|\vec{p}| = p_\mathrm{w}(1 - \lambda(c_\mathrm{c} + c_\mathrm{a})/2). \tag{49}$$

Given the relationship between the dielectric constant, ϵ_s, and dipole moment, *viz.*, $\epsilon_\mathrm{s} = \epsilon_\mathrm{opt,s} + \frac{c_\mathrm{s} N_\mathrm{A} |\vec{p}|^2}{3\epsilon_0 k_\mathrm{B} T}$, the negative correlation captures the dielectric decrement in regions with high ion concentration [159]. Since the dielectric decrement effect affects the distance between the two local maxima in C_d curves, λ is also calibrated to reproduce the experimentally measured C_d. The calibration process is detailed in Chapter 3.

2.3.4. Controlling equations

The above equations change the Helmholtz free energy for classical particles (Eqn.(11)) to

$$\begin{aligned} f_\mathrm{C} = &-\frac{1}{2}\epsilon_\mathrm{opt}(\nabla\phi)^2 + (n_\mathrm{c} q_\mathrm{c} - n_\mathrm{a} q_\mathrm{a})\phi - n_\mathrm{s}\beta^{-1}\ln\left(\frac{\sinh\left(\beta|\vec{p}|\left|\vec{E}_\mathrm{tot}\right|\right)}{\beta|\vec{p}|\left|\vec{E}_\mathrm{tot}\right|}\right) \\ &+ \sum_{\mathrm{l=c,a}} \beta^{-1}\left(n_\mathrm{l}\ln\left(n_\mathrm{l}\Lambda_\mathrm{l}^3\right) - n_\mathrm{l}\right) + \Phi_\mathrm{ex}(\{n_\mathrm{l}\}) + (n_\mathrm{cc} - n_\mathrm{e})e_0\phi. \end{aligned} \tag{50}$$

Accordingly, a modified expression for the grand potential (Eqn. (12)) is obtained,

$$
\begin{aligned}
g = {} & e_{\mathrm{au}} a_0^{-3}\left(t_{\mathrm{TF}}(1+\theta_{\mathrm{T}} s^2) + u_{\mathrm{X}}^0(1+\theta_{\mathrm{X}} s^2) + u_{\mathrm{C}}^0 + \theta_{\mathrm{C}} n_{\mathrm{e}} a_0^3 t^2 + v_{\mathrm{cc}} n_{\mathrm{e}} a_0^3\right) \\
& - \frac{1}{2}\epsilon_{\mathrm{opt}}(\nabla\phi)^2 + \sum_{\mathrm{l=c,a}} n_{\mathrm{l}} w_{\mathrm{l}}(r) + \sum_{\mathrm{l=c,a}} n_{\mathrm{l}} q_{\mathrm{l}} \phi \\
& - n_{\mathrm{s}} \beta^{-1} \ln\left(\frac{\sinh\left(\beta|\vec{p}|\left|\vec{E}_{\mathrm{tot}}\right|\right)}{\beta|\vec{p}|\left|\vec{E}_{\mathrm{tot}}\right|}\right) + \sum_{\mathrm{l=c,a}} \beta^{-1}\left(n_{\mathrm{l}} \ln\left(n_{\mathrm{l}} \Lambda_{\mathrm{l}}^3\right) - n_{\mathrm{l}}\right) \\
& + \Phi_{\mathrm{ex}}(\{n_{\mathrm{l}}\}) + (n_{\mathrm{cc}} - n_{\mathrm{e}}) e_0 \phi - n_{\mathrm{e}} \tilde{\mu}_{\mathrm{e}} - \sum_{\mathrm{l=c,a}} n_{\mathrm{l}} \tilde{\mu}_{\mathrm{l}}.
\end{aligned} \tag{51}
$$

Applying Euler–Lagrange equation to Eqn. (51), the new controlling equation for the electric potential is found,

$$
-\nabla\cdot(\epsilon_{\mathrm{eff}}\nabla\phi) = e_0(n_{\mathrm{cc}} - n_{\mathrm{e}}) + e_0(n_{\mathrm{c}} - n_{\mathrm{a}}) - \nabla\cdot\left[n_{\mathrm{s}}|\vec{p}|\frac{\mathcal{L}\left(\beta|\vec{p}|\left|\vec{E}_{\mathrm{tot}}\right|\right)}{\left|\vec{E}_{\mathrm{tot}}\right|}\vec{A}\right]. \tag{52}
$$

This equation differs from the conventional modified Poisson equation (Eqn. (13)) in two aspects: (i) an additional term for the dipolar solvent $-\nabla\cdot\left[n_{\mathrm{s}}|\vec{p}|\frac{\mathcal{L}(\beta|\vec{p}||\vec{E}_{\mathrm{tot}}|)}{|\vec{E}_{\mathrm{tot}}|}\vec{A}\right]$, and (ii) the expression of ϵ_{eff},

$$
\epsilon_{\mathrm{eff}} = \epsilon_{\mathrm{opt}} + n_{\mathrm{s}}|\vec{p}|\frac{\mathcal{L}\left(\beta|\vec{p}|\left|\vec{E}_{\mathrm{tot}}\right|\right)}{\left|\vec{E}_{\mathrm{tot}}\right|}. \tag{53}
$$

Since the number density distribution of solvents are predefined by Eqn. (48), the expressions for the number density of cations and anions will change accordingly. Eqns. (23) and (24) are modified as

$$
\frac{n_{\mathrm{c}}}{n_{\mathrm{site}} - \gamma_{\mathrm{c}} n_{\mathrm{c}} - \gamma_{\mathrm{a}} n_{\mathrm{a}}} \exp\left(\beta(w_{\mathrm{c}} + e\phi)\right) = \frac{n_{\mathrm{c}}^{\mathrm{b}}}{n_{\mathrm{site}} - \gamma_{\mathrm{c}} n_{\mathrm{c}}^{\mathrm{b}} - \gamma_{\mathrm{a}} n_{\mathrm{a}}^{\mathrm{b}}}, \tag{54}
$$

$$
\frac{n_{\mathrm{a}}}{n_{\mathrm{site}} - \gamma_{\mathrm{c}} n_{\mathrm{c}} - \gamma_{\mathrm{a}} n_{\mathrm{a}}} \exp\left(\beta(w_{\mathrm{a}} - e\phi)\right) = \frac{n_{\mathrm{a}}^{\mathrm{b}}}{n_{\mathrm{site}} - \gamma_{\mathrm{c}} n_{\mathrm{c}}^{\mathrm{b}} - \gamma_{\mathrm{a}} n_{\mathrm{a}}^{\mathrm{b}}}. \tag{55}
$$

One can divide Eqn. (54) by Eqn. (55) to get $n_{\mathrm{c}}/n_{\mathrm{a}}$, and then substitute $n_{\mathrm{c}}/n_{\mathrm{a}}$ to Eqn. (54) to solve for n_{a}. Substituting the expression of n_{a} into Eqn. (55) yields n_{c}. The final expressions for n_{c} and n_{a} are

$$\frac{n_{\mathrm{c}}}{n_{\mathrm{site}}}=\frac{n_{\mathrm{c}}^{\mathrm{b}}\exp[-\beta(w_{\mathrm{c}}+e\phi)]}{\gamma_{\mathrm{c}}n_{\mathrm{c}}^{\mathrm{b}}\exp[-\beta(w_{\mathrm{c}}+e\phi)]+\gamma_{\mathrm{a}}n_{\mathrm{a}}^{\mathrm{b}}\exp[-\beta(w_{\mathrm{a}}-e\phi)]+n_{\mathrm{site}}-\gamma_{\mathrm{c}}n_{\mathrm{c}}^{\mathrm{b}}-\gamma_{\mathrm{a}}n_{\mathrm{a}}^{\mathrm{b}}}, \tag{56}$$

$$\frac{n_{\mathrm{a}}}{n_{\mathrm{site}}}=\frac{n_{\mathrm{a}}^{\mathrm{b}}\exp[-\beta(w_{\mathrm{a}}-e_0\phi)]}{\gamma_{\mathrm{c}}n_{\mathrm{c}}^{\mathrm{b}}\exp[-\beta(w_{\mathrm{c}}+e\phi)]+\gamma_{\mathrm{a}}n_{\mathrm{a}}^{\mathrm{b}}\exp[-\beta(w_{\mathrm{a}}-e\phi)]+n_{\mathrm{site}}-\gamma_{\mathrm{c}}n_{\mathrm{c}}^{\mathrm{b}}-\gamma_{\mathrm{a}}n_{\mathrm{a}}^{\mathrm{b}}}. \tag{57}$$

The controlling equation for the electron density remains the same as Eqn. (29).

2.4. Summary

This section introduced the theoretical framework that will be applied to study supported NP systems. Combining classical MPB theory and quantum-mechanical orbital-free density functional theory, the DPFT model can efficiently capture electronic and ionic degrees of freedom self-consistently in constant potential condition. The presented new formalism represents an upgrade of the model by providing a new description of metal–solvent interactions that captures the reorientation of the first-layer solvent molecules. In addition, the effective dipole moment of solvents is related to the local ion concentration to represent the ion–solvent interactions.

In the next chapter, a newly developed calibration procedure for model parameters will be presented, and then the DPFT method will be applied to the simplest metal–metal contact system, namely two infinitely extended, parallel slabs placed at various distances, before moving on to the main objective: the supported NP system.

3. Calibration of model parameters for gold and silver planar electrodes

3.1. Introduction

This chapter first presents the workflow for calibrating the model parameters using planar electrodes of gold (Au) and silver (Ag). Subsequently, the DPFT method, presented in the previous chapter, will be demonstrated by applying it to a simple system consisting of two infinitely extended, planar slabs of Au and Ag placed in contact.

To obtain meaningful and physically sound results, it is essential not only to have the correct model framework and governing equations, but also to ensure that the model parameters are accurate and reliable. This requires careful calibration of the parameters so that the model can accurately reproduce key physicochemical properties of single-metal planar electrodes, such as work function, PZC, and differential capacitance. Only after this step can one confidently apply the model to explore the properties of more complex systems, such as metal–metal contacts.

Previous application of DPFT has primarily focused on modeling the properties of electrodes immersed in electrolyte solution [111]. In contrast, this thesis will compare the electrostatic characteristics of the system of interest both in vacuum and in solution environment. Thus, it is crucial to use a single set of model parameters that can accurately reproduce the physicochemical properties of metals in both environments. To achieve this, a three-step calibration procedure will be employed, as will be discussed in detail in the following sections.

In this study, we choose polycrystalline (pc) Au and Ag(111) surfaces as test systems, rather than platinum (Pt) or carbon (C), primarily because reliable experimental data, such as work function, PZC, and differential capacitance curves, are readily available for these electrodes in the literature. Moreover, Au and Ag are widely used electrocatalysts for reactions such as CO_2 reduction, making them relevant model systems [160].

An idealized setup of two infinitely large, parallel slabs is a good starting point for evaluating the theory for two reasons. Firstly, it simplifies the problem to a one-dimensional geometry, with variations only occurring in the direction perpendicular to the slabs, while in-plane properties remain uniform. Secondly, it allows focusing on the fundamental physics of charge redistribution and potential profile at the metal–metal interface. This is a necessary step toward understanding the more complex interactions and equilibrations in supported NP systems, which involve both internal (NP–support) and external (NP–solution and support–solution) interfaces. The next chapter will turn the attention to these external interfaces.

3.2. Three-step parameter calibration

Electrochemical properties of a specific electrode can vary significantly depending on the environment. A notable example is the difference in work function between vacuum and solvent environments. The goal is to use a unique set of parameters that can consistently describe the physio-electrochemical properties of a given electrode across all three environments, *i.e.*, vacuum, solvent and electrolyte. The model calibration thus involves three consecutive steps to reproduce (i) electronic, (ii) dielectric and (iii) ionic properties. Firstly, parameters are calibrated for electronic properties in the electrode–vacuum system to reproduce experimentally observed work function, Φ. Secondly, a continuum dielectric medium is incorporated into the system and solvent-related parameters are calibrated to reproduce the PZC. Lastly, the electrolyte is introduced and ionic parameters are calibrated to reproduce the C_d curve. The sequential calibration process is summarized in Table 1 and the experimental data are summarized in Table 2.

Table 1: Three-step calibration process.

Step	Interface	Property	Calibrated parameters
1	solid–vacuum	work function	v_cc^0
2	solid–solvent	potential of zero charge	$L_\mathrm{s}, l_\mathrm{s}, A^0, L_\mathrm{A}, l_\mathrm{A}$
3	solid–electrolyte	differential capacitance	$r_\mathrm{a}, r_\mathrm{c}, \lambda$

Table 2: Experimental literature references for Φ, PZC, and C_d.

Electrode	Φ [eV]	PZC [V$_\mathrm{SHE}$]	C_d
pc Au	5.20 [161,162]	0.19 [163,164]	[163,164]
Ag(111)	4.60 [76,165,166]	–0.44 [37]	[37]

3.2.1. Calibration of electronic parameters: work function

The work function, Φ, is given by $\Phi = e\chi - \mu_{\mathrm{e}}$ with the chemical potential of electrons, μ_{e}, and the surface potential, χ. μ_{e} is determined by the volumetric number density of metal core charges, n_{cc}, and the pseudopotential caused by them, v_{cc}. χ is affected by n_{cc}. Since n_{cc} takes a fixed value for a specific material, v_{cc} is used as a fitting parameter to reproduce experimentally measured values of Φ, as specified in Table 2.

As in Ref. [111], n_{cc} is calculated by $n_{\mathrm{cc}} = N_{\mathrm{e}} n_{\mathrm{core}} = N_{\mathrm{e}} \rho N_{\mathrm{A}} / M$ with volumetric number density of metal atomic cores, n_{core}, number of valence electrons per atom, N_{e}, mass density, ρ, and the Molar mass, M. Parameter values are given in Table 3.

Table 3: Calibrated electronic parameter values for pc Au and Ag(111) electrodes.

Slab	$\boldsymbol{n_{\mathrm{core}}}$ $[\mathbf{cm^{-3}}]$	$\boldsymbol{N_{\mathrm{e}}}$	$\boldsymbol{n_{\mathrm{cc}}}$ $[\mathbf{cm^{-3}}]$	$\boldsymbol{v_{\mathrm{cc}}^{0}}$ $[\mathbf{eV}]$	$\boldsymbol{l_{v_{\mathrm{cc}}}}$ [Å]
pc Au	5.8528× 10^{22}	11	6.4875× 10^{23}	-1.5640	0.529
Ag(111)	5.8978× 10^{22}	11	6.4381× 10^{23}	12.1312	0.529

The error function is used to describe the decay of v_{cc} from its constant bulk value v_{cc}^{0} inside the metal to zero outside the metal surface,

$$v_{\mathrm{cc}} = \frac{v_{\mathrm{cc}}^{0}}{2} * \left(1 - \operatorname{erf}\left(-\frac{z}{l_{v_{\mathrm{cc}}}}\right)\right), \tag{58}$$

with the characteristic decay length $l_{v_{\mathrm{cc}}}$ assumed to be one Bohr radius. The calibration of Φ for Ag(111) and pc Au is accomplished by adjusting v_{cc}^{0}, which can be found in Table 3. Fixing the Fermi level of the system at $-\Phi$, a parametric sweep of v_{cc}^{0} is performed and the surface charge density is calculated as

$$\sigma = \int (n_{\mathrm{cc}} - n_{\mathrm{e}}) \mathrm{d}r. \tag{59}$$

The value of v_{cc}^{0} that makes σ negligibly small is chosen. The profiles of v_{cc}, n_{e} and ϕ for Ag(111) and pc Au are shown in Figure 6.

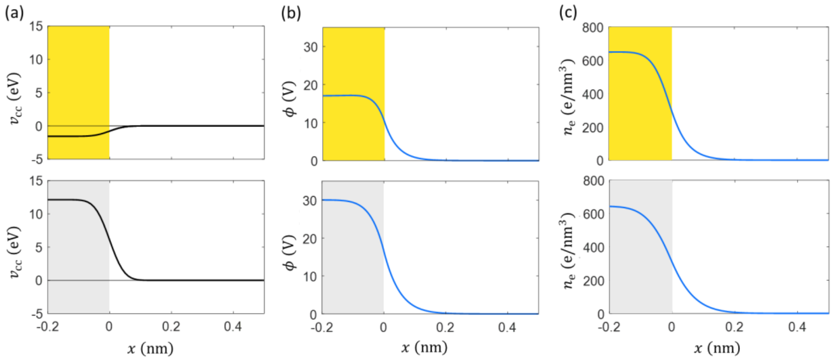

Figure 6. Profiles of (a) pseudopotential, (b) inner potential, (c) electron density for pc Au (top row) and Ag(111) (bottom row) electrode–vacuum interface.

3.2.2. Calibration of solvent parameters: potential of zero charge

The calibration of solvent parameters involves setting the electrode potential at the PZC values, and then tuning the solvent parameters, namely the profiles of $\vec{A}$ (Eqn. (41)) and c_{s} (Eqn. (48)), to ensure the charge-neutral state of the metal. The calibrated values of the solvent parameters are summarized in Table 4. The selection of L_{s} tunes features of C_{d} curves, particularly the value of the capacitance minimum at the PZC, as elaborated further in the next section.

Table 4: Calibrated solvent parameter values for pc Au and Ag(111) electrodes.

Symbol	**Definition**	**Value**	
		pc Au	Ag(111)
$\boldsymbol{A^0}$	strength of the chemical interaction, [V/m]	0	–22.185
$\boldsymbol{L_{\mathrm{A}}}$	position of the edge for $\vec{A}$, [Å]	3.9295	3.6000
$\boldsymbol{l_{\mathrm{A}}}$	width of the edge for $\vec{A}$, [Å]	0.1	0.1
$\boldsymbol{L_{\mathrm{s}}}$	position of the edge for solvent concentration, [Å]	1.1295	0.8000
$\boldsymbol{l_{\mathrm{s}}}$	width of the edge for solvent concentration, [Å]	0.1	0.1

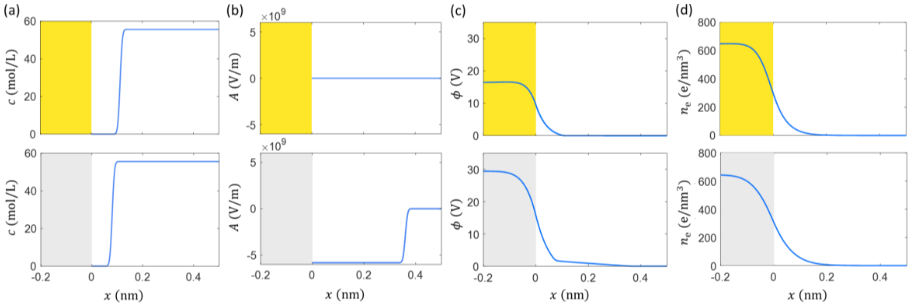

Figure 7. Profiles of (a) solvent concentration, (b) Auxiliary field strength, (c) electric potential, and (d) electron density for pc Au (top row) and Ag(111) (bottom row) electrode–solvent interface.

3.2.3. Calibration of ionic parameters: differential capacitance

In the third step, ionic parameters are calibrated to reproduce C_d curves. As shown in Figure 8, C_d curve entails four key features, namely (a) the value of the capacitance minimum, (b) the abscissa value of the minimum (the PZC), (c) the height of left and right peaks, and (d) the distance between the peaks.

Feature (a) is largely determined by the width of the gap between the electrode surface and the first layer of solvent molecules. This is due to the gap region having the lowest dielectric constant and thus the lowest capacitance. Feature (b) corresponds to the PZC of the electrode–electrolyte interface [36]. Since both features (a) and (b) have been accounted for in calibration step 2, features (c) and (d) remain to be taken care of. The relative height of the two peaks is determined by the cation and anion radii, whereas the distance between the two peaks is a concerted result of volume exclusion and dielectric decrement at large electrode potential.

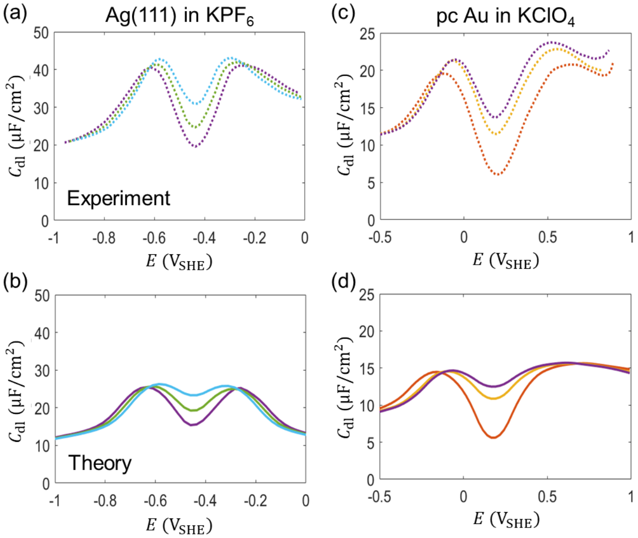

Figure 8. C_{d} curve for (a) Ag(111) in KPF$_6$ solution of 40 mM (blue), 20 mM (green) and 10 mM (purple) and (c) pc Au in KClO$_4$ solution of 20 mM (purple), 10 mM (yellow) and 1 mM (orange). (a) and (c) are experimental data [37,163,164] whereas (b) and (d) are theoretical results.

The C_{d} curves of Ag(111) in KPF$_6$ solution and pc Au in KClO$_4$ solution have been reproduced using fitting parameters in Table 5. Experimental data and fitting results are compared in Figure 8.

Table 5: Calibrated ionic parameter values for pc Au and Ag(111) electrodes.

Symbol	**Definition**	**Value**	
		pc Au	Ag(111)
$\boldsymbol{r}_{\mathbf{a}}$	anion radius, $[\text{Å}]$	$3.38\ (\mathrm{ClO}_4^-)$	$5.5\ (\mathrm{PF}_6^-)$
$\boldsymbol{r}_{\mathbf{c}}$	cation radius, $[\text{Å}]$	$6\ (\mathrm{K}^+)$	$5.5\ (\mathrm{K}^+)$
$\boldsymbol{\lambda}$	coefficient of the effective dipole moment on local ion concentration, $[\mathrm{mol}^{-1}]$	7.255×10^{-4}	9.481×10^{-4}

3.3. Contact interface of gold and silver slabs

In this section, I will demonstrate the calibrated model for the simplest multi-component system, *i.e.*, two infinitely large parallel slabs made of Ag and Ag brought into contact. Before contacted, the two slabs are charge-neutral but have different Fermi levels.

After connection by a metal wire or by direct contact, electrons redistribute across the system to equilibrate the Fermi levels, but the overall charge remains zero, i.e., the free charges on gold and silver slabs cancel each other. The electrical connection in our simulations is guaranteed by assigning to the system a uniform electrochemical potential of electrons, $\tilde{\mu}_{\mathrm{e}}$, at which the overall system is charge-neutral.

Since $\tilde{\mu}_{\mathrm{e}}$ can be converted to the electrode potential E vs. the standard hydrogen electrode by $E = -(\tilde{\mu}_{\mathrm{e}} - \tilde{\mu}_{\mathrm{e,SHE}})/e$, the Fermi levels of the three aforementioned charge-neutral entities are equivalent to $\mathrm{PZC}_{\mathrm{Au}}$, $\mathrm{PZC}_{\mathrm{Ag}}$ and GPZC, respectively.

From large distance, the distance between the two slabs is decreased, during which process it is monitored how the electric potential and electron density start to overlap (see Figure 9). Figure 10 visualizes the consequence of electron redistribution by the electric potential difference and charge density difference plot. In this section, special attention is paid to the contact region of gold and silver, which lends the convenience of focusing only on the external surface charging of supported NP in the next chapter.

As shown in Figure 9 (a) and (b), the electric potential and electron density start to overlap at a distance of around 0.3 nm. Figure 9(c) shows that significant amount of negative electronic charges locates at the gap region, while immediately inside the metal jellium edge exist positive charges. It is worth noting that, up till now, we cannot draw any conclusion about the charge redistribution, for which we need to subtract the charge density profile of the combined system by the profiles of separate constituting entities, but the results shown in Figure 9 only represent the actual profile of the combined system.

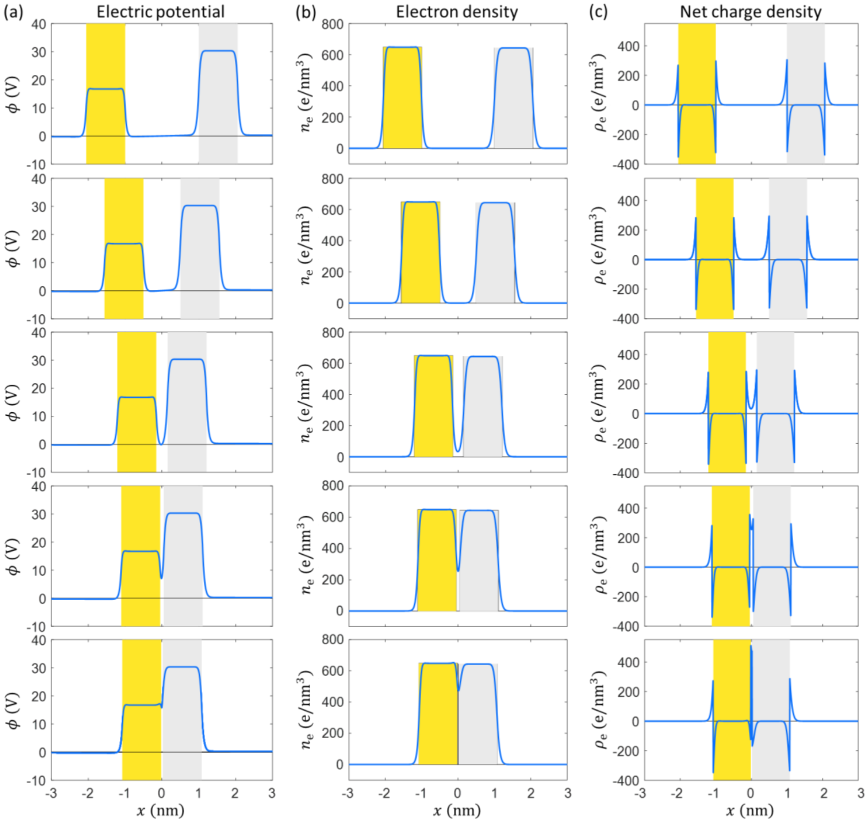

Figure 9. Profiles of (a) electric potential, (b) electron density, and (c) net charge density across the gold (left) and silver (right) slabs placed at various distances—from top to bottom, 2 nm, 1 nm, 0.3 nm, 0.1 nm, 0.033 nm. The two slabs are illustrated by the gold and silver rectangles. The electronic parameters remain the same as the calibrated model for pc Au and Ag(111) slabs in the previous section. In (b), the positive atomic charges (the jellium background) are depicted by the gold and silver rectangles.

The change of electric potential and charge density induced by electronically connecting the two metals is visualized in Figure 10 by the electric potential difference plot and charge density difference plot, calculated respectively by

$$\Delta\phi = \phi^{\mathrm{AuAg}}(\mathrm{GPZC}) - \phi^{\mathrm{Au}}(\mathrm{PZC_{Au}}) - \phi^{\mathrm{Ag}}(\mathrm{PZC_{Ag}}), \tag{60}$$

$$\Delta\rho_{\mathrm{e}} = \rho_{\mathrm{e}}^{\mathrm{AuAg}}(\mathrm{GPZC}) - \rho_{\mathrm{e}}^{\mathrm{Au}}(\mathrm{PZC_{Au}}) - \rho_{\mathrm{e}}^{\mathrm{Ag}}(\mathrm{PZC_{Ag}}). \tag{61}$$

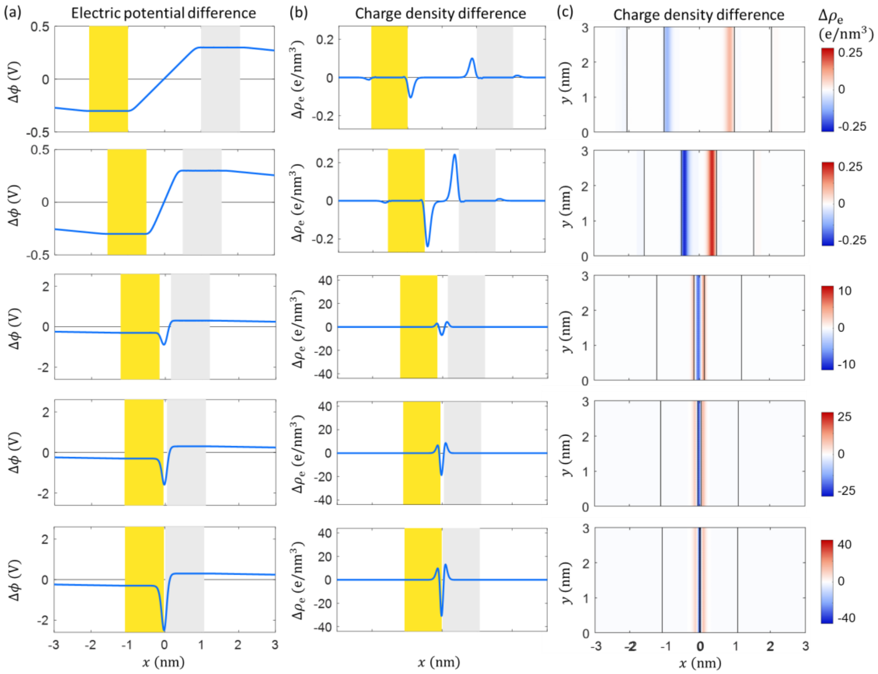

Figure 10. Profile of (a) electric potential difference and (b) charge density difference across the centers of the two slabs ($y = 0$). Two-dimensional illustration of the charge density difference is shown in (c). From top to bottom the distance between the two slabs are 2 nm, 1 nm, 0.3 nm, 0.1 nm, 0.033 nm.

At large distances ($d_{\mathrm{gap}} = 1 \text{ or } 2 \text{ nm}$), upon connecting the two slabs electronically (say, by a metal wire), electrons in the silver slab transfer to the gold slab, driven by the Fermi-level difference, as can be seen in Figure 10(b) by the positive and negative charges at silver and gold surfaces, respectively, and the resulting potential step, shown in Figure 10(a), between the two slabs with a magnitude of 0.6 V that exactly compensates the Fermi-level difference of uncharged pc Au (–5.2 eV) and uncharged Ag(111) (–4.6 eV). The potential difference of 0.6 V remains during the process of further decreasing d_{gap} down to 0.033 nm, however, in the gap region the $\Delta\phi$ profile is no longer linear, but exhibits a dip. This behavior is the result of the formation of a “triple-layer” structure of $\Delta\rho_{\mathrm{e}}$ at the contact interface shown in the bottom three rows in Figure 10(b). For free-standing gold or silver slabs, electrons spillover to as far as 0.6 nm away from the jellium edge. As soon as the gold and silver slabs are placed at a distance of 0.3 nm, the spillover electrons overlap, and Pauli repulsion leads to a so-called “pushback effect” that effectively push the electron tails back towards the metal skeleton [167]. In other words, the spillover electrons cannot exist as far from the electrode surface as before, but accumulate at a region closer to the jellium edge. Therefore, compared with separate free-standing gold and silver slabs, the combined gold–silver system has more electrons at the gap region, and fewer electrons at the solid region. It is worth noting that the deficiency of electrons in the solid phase, say Au slab, does not imply a electron transfer from Au to Ag upon contact, but simply reflects that the presence of the Au slab, by way of Pauli repulsion, prevents the spillover electrons of the Ag slab from spreading as far as before. A two-dimensional illustration is provided in Figure 10(c), where the triple layer structure seen here will also appear at the NP–support contact interface to be discussed in the next chapter.

Figure 11 shows that there exists an equilibrium distance between the gold and silver slabs with a magnitude of around 0.1 nm. The calculations are done for electrically connected Au and Ag slabs. For the slabs placed far away from each other, the excess charges of opposite signs exert attractive forces between the two slabs. When placing to close to each other, the electron kinetic energy increases significantly, leading to repulsive forces. The balance of these two factors coincides with the free energy minimum.

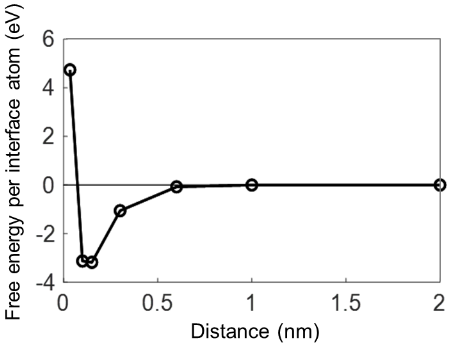

Figure 11. Free energy of the Au and Ag slabs as a function of the distance between them. At around 0.1 nm the free energy reaches a minimum.

3.4. Summary

This section presented a three-step calibration process that allows capturing electrostatic properties of a metal in both vacuum and solution environment using a single set of parameters. After obtaining reliable model parameters, capabilities of the updated DPFT model have been demonstrated using the simplest multi-component system composed of a gold slab in contact with a silver slab. It has been shown that the electron density redistribution relies on the relative magnitude of the work functions of silver and gold. There exists an equilibrium distance between the two slabs, and a triple-layer structure of redistributed electrons manifest at the Ag–Au contact region. The foundation laid in this chapter sets the stage for a detailed investigation of the supported NP system in Chapter 4.

4. Electro-ionic metal–support interactions in supported NP systems

4.1. Introduction

Electrocatalyst NPs anchored on a supporting material are key components in electrochemical devices, such as fuel cells and electrolyzers. Understanding interactions between NPs and support material is crucial for optimizing catalytic performance of supported electrocatalyst NPs. While the primary roles of the support are to provide stable anchoring and supply (or remove) electrons to (or from) NPs, it also impacts their physiochemical properties and catalytic activity [59,168–171]. A class of effects, subsumed as metal–support interactions (MSI), have garnered wide attention. However, the underlying physical phenomena contributing to these interactions have remained elusive [60,172–176].

Nanoscopic heterogeneities in composition and structure are quintessential for the functional properties of electrocatalyst materials. Yet, unraveling these properties poses formidable challenges for theory and computation. Here, the semiclassical model presented in Chapter 2 is used to study the electrochemical properties of supported electrocatalyst NPs. It captures the concurrent electronic and ionic equilibration in the three-component system of catalyst NP, support and electrolyte. It will be analyzed how the support induces perturbations in local electronic and ionic charge densities at the active surface of the NP, and how it shapes the capacitive response of supported NP electrodes.

4.2. Electronic metal–support interactions

4.2.1. Experimental findings

Photoelectron spectroscopy, scanning transmission electron microscopy, and electron holography measurements have provided direct experimental evidence and quantification for the electron redistribution across Pt NP–oxide support systems [177–179].

The influence of electron redistribution on the catalytic activity has been explored by

Hwang and coworkers, who anchored Pt NPs on $Ti_{0.7}Mo_{0.3}O_2$ support and demonstrated sevenfold increase in current density at 0.9 V_{SHE} for the ORR compared to the commercial Pt/C (E-TEK) catalyst [173]. Jackson and coworkers deposited Pt NPs on a B_4C support, showing a 2.5-fold increase in current density at 0.9 V_{SHE} [180]. Both groups attributed the drastic performance enhancement to the increased electron transfer from their novel support materials ($Ti_{0.7}Mo_{0.3}O_2$ or B_4C) compared to the conventional carbon support, using X-ray photoelectron spectroscopy (XPS) and X-ray absorption near edge structure (XANES) measurements.

Despite the apparent agreement on increased catalytic activity and the proposed mechanism, some controversies between these two studies remain unresolved. Jackson's ex-situ XPS measurements in an ultra-high vacuum showed a shift in the Pt 4f peak, indicating a higher valence state occupancy and larger electron transfer from B_4C to NP than from carbon. Hwang's ex-situ XANES results show increased electron transfer from $Ti_{0.7}Mo_{0.3}O_2$ to NP, as indicated by a lower L3 edge, in line with Jackson's XPS measurement. However, Jackson's in-situ XANES results showed decreased electron transfer from the support to the NPs, as indicated by a higher L2 edge while keeping the L3 aligned.

The discrepancy may arise from inappropriate interpretation of the X-ray spectroscopy results. Therefore, despite it being clear that electron transfer occurs from the support to the NPs, it remains elusive whether the NPs receive more electrons from the novel boron carbide support than from conventional carbon. Consequently, it is unclear whether increased electron or decreased electron transfer to the Pt NP benefits the catalytic activity.

4.2.2. State-of-the-art modelling activities

First-principles calculations based on Kohn–Sham DFT have elucidated electron redistribution at metal–support interfaces in vacuum [134,181–186]. This electron redistribution regulates electrochemical properties of surface sites at the particle, and tunes adsorption strengths of reaction intermediates [61,187–190]. Immersed in an electrolyte solution, distinct physiochemical properties of NPs and support co-determine characteristics of the EDL along the heterogeneous solid–liquid interface. Overlapping EDLs of the support and NPs modulate local reaction environment [191] and, thereby, tune the electrocatalytic activity, as revealed by experiments and rationalized by continuum modelling [57,58].

While previous studies have focused on either electronic or ionic MSI effects, viz., electron redistribution or EDL overlap, it has been emphasized that both are coupled by the equilibration across the three-component system of catalyst NP, support, and electrolyte [172]. However, there is a lack of self-consistent treatment for the electro-ionic coupling at nanoparticle-based electrodes. EDL models based on MPB theory neglect electronic equilibration inside the solid phase [95]. First-principles calculations of electrochemical interfaces face challenges not only in constant-potential simulations [130–133] but also in their considerable computational cost, rendering them unsuitable for systems containing thousands of atoms, such as electrolyte-surrounded supported nanosized particles. Consequently, previous studies of electronic MSI effects were restricted to the contact interface between a sub-nanometer cluster and its support in vacuum [134,135]. It remains unclear in what way electrons redistribute at the external surface of NPs in contact with electrolyte. As a result, there is a notable gap in understanding joint effects of electron redistribution and n local electrochemical properties.

4.3. Methodologies

4.3.1. Density–potential functional theory

The recently developed semi-classical density–potential functional theory (DPFT) represents a physically consistent approach to treating electronic and ionic degrees of freedom on an equal footing [111,122–124]. By handling metal electrons through orbital-free DFT [44–46], this method not only ensures high computational efficiency but also captures electronic equilibration and electron spillover phenomena. Furthermore, it enables constant-potential simulations by fixing the electrochemical potential of electrons, $\tilde{\mu}_{\mathrm{e}}$. Meanwhile, solvents and ions are treated using statistical field theory [36,96,138]. DPFT solves for key quantities including electron density, n_{e}, electric potential, ϕ, electric field $\vec{E}$, the number density of cations, n_{c}, and anions, n_{a}. The derivation of governing partial differential equations are introduced in Chapter 3.

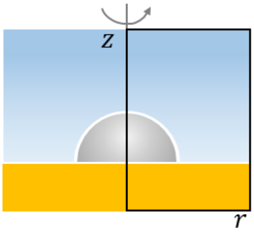

Figure 12. The supported NP system is calculated in a cylindrical coordinate.

Since the supported NP system can be approximated as having axial symmetry, the controlling equations can be solved in a cylindrical coordinate (Figure 12). The divergence operator applied to a vector F in a cylindrical coordinate is written as,

$$\nabla\cdot F=\frac{1}{r}\frac{\partial}{\partial r}(rF_r)+\frac{1}{r}\left(\frac{\partial F_\theta}{\partial\theta}\right)+\frac{\partial F_z}{\partial z},\tag{62}$$

In case of axial symmetry, the equation drops the θ-dependence and reduces to

$$\nabla\cdot F=\frac{1}{r}\frac{\partial}{\partial r}(rF_r)+\frac{\partial F_z}{\partial z},\tag{63}$$

The controlling equation of electric potential, Eqn. (52), takes on the form of,

$$\frac{1}{r}\frac{\partial}{\partial r}\left(r\left(-\epsilon_{\mathrm{eff}}\frac{\partial\phi}{\partial r}+n_{\mathrm{s}}|\vec{p}|\frac{\mathcal{L}\left(\beta|\vec{p}|\left|\vec{E}_{\mathrm{tot}}\right|\right)}{\left|\vec{E}_{\mathrm{tot}}\right|}\vec{A}_{\mathrm{r}}\right)\right)+\frac{\partial}{\partial z}\left(-\epsilon_{\mathrm{eff}}\frac{\partial\phi}{\partial z}+n_{\mathrm{s}}|\vec{p}|\frac{\mathcal{L}\left(\beta|\vec{p}|\left|\vec{E}_{\mathrm{tot}}\right|\right)}{\left|\vec{E}_{\mathrm{tot}}\right|}\vec{A}_{\mathrm{z}}\right)\\=e_0(n_{\mathrm{cc}}-n_{\mathrm{e}}+n_{\mathrm{c}}-n_{\mathrm{a}}).\tag{64}$$

The controlling equation for the electron density, Eqn. (38), is written as,

$$\frac{1}{r}\frac{\partial}{\partial r}\left(r\frac{\partial\psi}{\partial r}\right)+\frac{\partial^2\psi}{\partial z^2}=-\frac{\pi^{\frac{5}{3}}3^{\frac{1}{3}}\theta_{\mathrm{T}}}{5(\theta_{\mathrm{T}}\omega-\theta_{\mathrm{XC}})}\left(\left(\frac{\partial\psi}{\partial r}\right)^2+\left(\frac{\partial\psi}{\partial z}\right)^2\right)\\+\frac{20}{9}\psi\frac{\omega}{\theta_{\mathrm{T}}\omega-\theta_{\mathrm{XC}}}\left(\frac{\partial t_{\mathrm{TF}}}{\partial\bar{n}_{\mathrm{e}}}+\frac{\partial u_{\mathrm{X}}^0}{\partial\bar{n}_{\mathrm{e}}}+\frac{\partial u_{\mathrm{C}}^0}{\partial\bar{n}_{\mathrm{e}}}-\frac{e_0\phi+\tilde{\mu}_{\mathrm{e}}}{e_{\mathrm{au}}}\right).\tag{65}$$

4.3.2. Boundary conditions

The radial size of the simulation cell, R_{cell}, determines the fraction of the support surface that is covered by the NP, *viz*., $\theta = R_{\mathrm{cat}}^2/R_{\mathrm{cell}}^2$. The lower boundary of the cell in the bulk of the support warrants a zero-normal-flux boundary condition for n_{e} and ϕ. At the upper boundary in the bulk of the solution, we set n_{e} and ϕ to zero. At $r = R_{\mathrm{cell}}$, n_{e} and ϕ exhibit zero normal flux. The governing equations are solved using the mathematics module of COMSOL Multiphysics.

4.3.3. Equilibrium distance between NP and support

The calibrated model is used to simulate a hemispherical Ag NP with a radius of $R_{\mathrm{cat}} = 1\,\mathrm{nm}$, anchored on a Au support. The metal atomic-core charges of Ag or Au are homogeneously distributed according to a jellium model. The system's cylindrical symmetry effectively reduces the dimensionality to 2D, with a radial coordinate r and a surface-normal coordinate *z*.

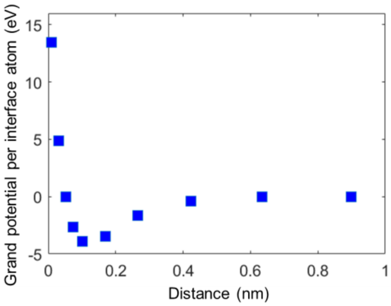

Figure 13. Grand potential of the total system as a function of the gap distance between NP and support. The NP–support contact interface corresponds to approximately 45 silver atoms within a circle of 1 nm radius. The grand potential per interface atom is therefore normalized with respect to 45 atoms.

The equilibrium distance between the two electronic jelliums of NP and support has been determined by minimizing the system's total free energy as a function of NP–support separation. As shown in Figure 13, the free energy displays a minimum at a distance of 0.1 nm, indicating stable anchoring of the NP on support. The binding energy per atom is approximately 4 eV, which approximately falls in the range of metallic bond of Au and Ag.

4.4. Model results

4.4.1. Schematic summary of main findings

Before diving into the details of the simulation results, two schematic illustrations, Figure 14 and Figure 15, are presented to highlight the two most significant findings: (1) the existence of long-range charge redistribution on the outer surface of supported NPs; (2) the classical concept of the PZC is no longer valid for describing the surface charging behavior of such heterogeneous supported NP systems.

Finding 1: Long-range charge redistribution. A commonly cited textbook example describes the contact between two different metals (idealized as infinite planar surfaces), where electrons transfer from the metal with a higher Fermi level to the one with a lower Fermi level until their Fermi levels equilibrate [192]. This results in a strong interfacial electric field as shown in Figure 14(a).

However, real catalytic systems are typically dispersed on the support as discrete NPs rather than forming a continuous film (Figure 14(b)). This structural configuration inherently introduces exposed catalyst–electrolyte and support–electrolyte interfaces. In such heterogeneous systems, in addition to the short-range charge redistribution at the metal–support interface caused by Fermi level mismatch, charge redistribution also occurs between the exposed outer surface of the NP and that of the support.

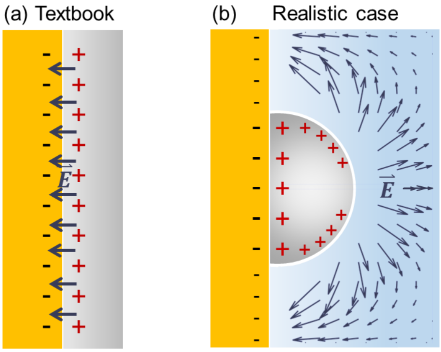

Figure 14. Schematic illustration of the first finding. (a) Textbook example of two planar metal slabs in contact. (b) Realistic supported metal NP system where long-range charge redistribution occurs on the outer surface of the NP, accompanied by the presence of an electric field in the surrounding electrolyte.

The redistribution at the outer surfaces generates a macroscopic electric field in the electrolyte, directed from the NP surface toward the support surface, surrounding the entire supported catalyst system. Notably, compared to the buried metal–support interface, the NP's outer surface is the actual site where catalytic reactions take place. It is at this interface that reactant molecules and electrolyte ions accumulate and interact. Therefore, an accurate description of the net surface charge and the associated electric field on the outer surface is critical for understanding how the support influences the catalytic activity of supported metal NPs.

Finding 2: Breakdown of local electroneutrality and inapplicability of the PZC concept. In the classical textbook model of a simplified planar electrode, when the applied electrode potential is lower (or higher) than the PZC, the metal surface acquires a net negative (or positive) charge. This surface charge attracts counterions from the electrolyte—cations for negatively charged surfaces and anions for positively charged ones—to form an EDL. These counterions screen the electric field produced by the surface charge, maintaining the overall electroneutrality of the system. Furthermore, since an infinite planar electrode is spatially uniform, local electroneutrality is preserved: in any arbitrarily chosen rectangular region near the interface, the sum of electronic and ionic charges is zero (Figure 15(a)).

In contrast, for supported metal NPs, the situation is more complex. Due to the requirement for Fermi level equilibration between the metal NP and the support, the silver NP acquires a net positive surface charge. Intuitively, one might expect anions from the electrolyte to be attracted to this positively charged surface. However, simulation results reveal the accumulation of cations at the surface of the silver NP instead. This counterintuitive phenomenon indicates that local electroneutrality is not maintained. Please see the middle figure of Figure 14(b).

The underlying cause of this behavior lies in the double-layer overlap effect, where the electric field generated by the support significantly influences the ionic distribution near the NP. Whether cations or anions accumulate near the NP surface is determined by the local electrostatic potential relative to that of the bulk solution. In a heterogeneous system, this local potential is not solely governed by the nearest solid surface, but is also affected by the charges on all surrounding surfaces. In other words, the electrostatic environment at any given point is dictated by the collective influence of the entire heterogeneous electrode system.

At the applied potential used in the simulations, the support surface bears a large negative charge. This shifts the local potential near the metal NP to a value lower than the bulk solution potential, leading to the unexpected accumulation of cations—not anions—on the positively charged Ag NP surface.

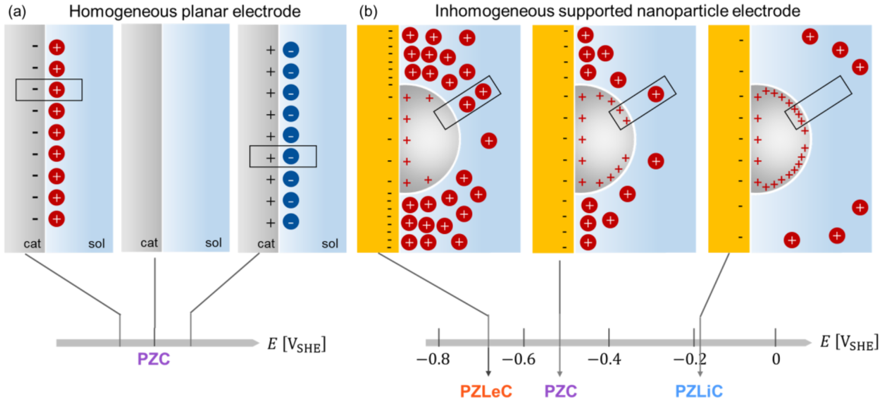

Figure 15. Schematic illustration of the second finding. (a) Classical textbook example of planar uniform electrode with local charge-neutrality. (b) In realistic supported NP system, due to the combined effects of EMSI and IMSI, regions near the outer surface of the metal NP exhibit electronic and ionic charges of the same sign. From left to right, the electrode potential is controlled at the potential of zero local electronic charge (PZLeC), the PZC of Ag NP, the potential of zero local ionic charge (PZLiC). These concepts will be explained in section 4.4.5.

4.4.2. Global work function and global PZC

Before contact, the dissimilar Fermi levels of a charge-neutral Ag NP and a charge-neutral Au support correspond to different work function (Φ) in vacuum environment. Upon contact, while the composite material remains overall charge-neutral, electrons redistribute to equilibrate the Fermi levels. The energy difference between the equilibrated Fermi level and the vacuum level is defined as the global Φ of the composite material, the value of which is affected by the Φ of individual components as well as the NP coverage on support, θ. As shown in Figure 16, in the low-coverage limit, the global Φ approaches 5.20 eV, the value for the bare Au support. As θ increases, the global Φ decreases and eventually becomes lower than the value for planar Ag (4.60 eV), because Φ of nanosized particles tends to be lower than that of extended surfaces.

In electrolyte solution, the Fermi level can also be represented by the electrode potential with respect to a reference electrode, say the standard hydrogen electrode, through $E = -(\epsilon_{\mathrm{F}} - \epsilon_{\mathrm{F,SHE}})/e$. The Fermi levels of the uncharged catalyst NP and of the uncharged support can be converted to the PZC of the catalyst ($\mathrm{PZC_c}$) and of the support ($\mathrm{PZC_s}$). The contact-induced equilibrated Fermi level can thus be converted to the electrode potential, at which the overall ρ_{e} (or ρ_{ion}) in the electrode (or electrolyte solution) equals zero; this electrode potential is called the global PZC (GPZC). The nonlinear shape of the coverage-dependent global PZC and global Φ as seen in Figure 16 signifies the electron redistribution on the external surface of NP and support, as established in Ref. [134].

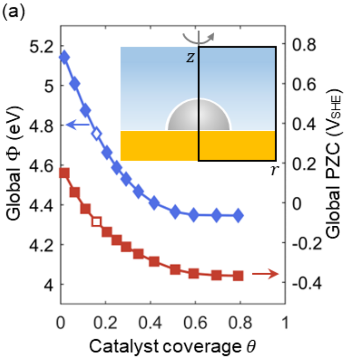

Figure 16. Global work function of Au-supported Ag NP in vacuum and global PZC in 1 mM KClO4 solution as a function of θ. Inset shows the simulation cell. The two open symbols represent a coverage of $\theta = 16\%$, which will be further studied later.

4.4.3. Local electro-ionic perturbations under constant charge condition

This section evaluates the situation for $\theta = 16\%$ and solution environment. The electronic charge density before and after contact is plotted in Figure 17(a). The charge separation across the jellium edge of NP at z≈1.15 nm due to electron spillover is clearly seen. However, the additional electronic charge induced by Fermi-level equilibration can hardly be discerned on the scale of the intrinsic ρ_{e}, as shown by the nearly overlapping curves of $\rho_{\mathrm{e}}^{\mathrm{sc}}$ and $\rho_{\mathrm{e}}^{\mathrm{s}} + \rho_{\mathrm{e}}^{\mathrm{c}}$. The electronic perturbation established upon contact of the two materials can be better visualized by plotting the electronic charge density difference between the combined and individual systems,

$$\Delta\rho_{\mathrm{e}} = \rho_{\mathrm{e}}^{\mathrm{sc}}(\mathrm{GPZC}) - \rho_{\mathrm{e}}^{\mathrm{s}}(\mathrm{PZC_s}) - \rho_{\mathrm{e}}^{\mathrm{c}}(\mathrm{PZC_c}). \tag{66}$$

The positive $\Delta\rho_{\mathrm{e}}$ at the NP surface corresponds to electron depletion, consistent with the direction of electron transfer from Ag NP to Au support. Given an atom density of around 100 atom/nm^3, the $\Delta\rho_{\mathrm{e}}$ peak value of 5 e/nm^3 translates to an increase in atom valency by approximately 0.05 e/atom. This magnitude is sufficient to exert notable catalytic effects such as the modification of activation barrier heights through electric interactions [190] and the shift in adsorbate binding energies by changing the occupancy of adsorbate-related (anti)bonding orbitals [134].

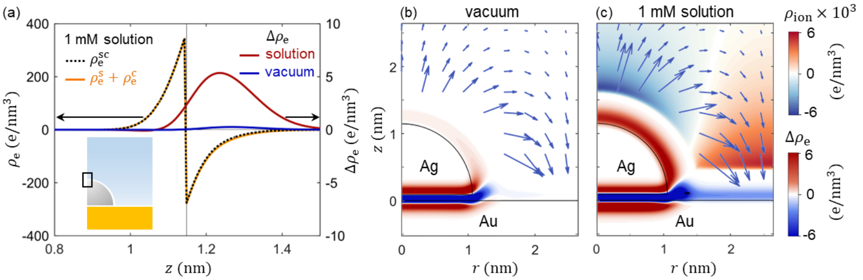

Figure 17. (a) ρ_{e} and $\Delta\rho_{\mathrm{e}}$ along a line through the top surface of the supported NP ($r = 0\ \mathrm{nm},\ 0.8\ \mathrm{nm} < z < 1.5\ \mathrm{nm}$). The jellium edge of the NP at $z \approx 1.15\ \mathrm{nm}$ is displayed by a vertical thin line for visual reference. The orange solid and black dotted curves represent ρ_{e} before and after contact, respectively, in 1 mM solution. The red and blue curves denote the $\Delta\rho_{\mathrm{e}}$ in a 1 mM $KClO_4$ solution and in vacuum, respectively. (b,c) Two-dimensional plot of ρ_{ion} and $\Delta\rho_{\mathrm{e}}$ for the overall charge-neutral supported NP in vacuum (b) and in solution (c). Calculation of ρ_{ion} requires fixing the electrode potential at the global PZC (–0.09 V_{SHE}). Ions locate approximately 0.5 nm away from the electrode, leaving the white region of 0.5 nm width along the solid surface. The electric field is represented by arrows.

Compared with the case of a solution environment, $\Delta\rho_{\mathrm{e}}$ in a vacuum environment is 20 times smaller. This effect is illustrated by direct comparison in Figure 17 (b) and (c). A surplus of electronic charge (red shaded) is apparent at the *external* surface of Ag NP, compensated by a depletion of electronic charge (blue shaded) at the surrounding Au support surface. One may well see the external surfaces of the NP and the support as two plates of a “parallel” capacitor with a dielectric medium sandwiched between them, as shown in Figure 18. The larger magnitude of charge redistribution for the solution case can be explained with capacitive charging of the two metal plates, under a “built-in” potential difference due to Fermi-level alignment [134]. This potential difference generates an electric field surrounding the composite material, pointing from the NP to the support, depicted by blue arrows in Figure 17(c). The presence of highly polarizable water dipoles contributes to a higher dielectric constant and thus stronger charging.

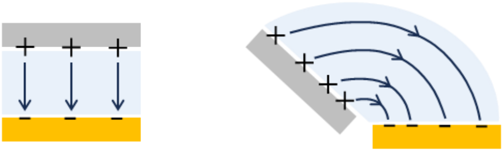

Figure 18. Conventional parallel capacitor (left) and the deformed “parallel capacitor” (right). The silver and gold slabs denote two electronic conductors while the blue region denotes a dielectric medium.

Although the solution phase maintains zero net ionic charge at the global PZC, variations in electric potential (ϕ) in the solution phase results in a lateral variation of ρ_{ion}, as shown in Figure 17(c). The blue shades above the Ag NP indicate strong accumulation of anions, while the red shades above the support imply cation excess, with local ion concentrations exceeding bulk concentration (1 mM) by an order of magnitude.

For both homogenous surface and heterogeneous surfaces, the total net ionic charge in the solution compensates the total net electronic charge in the electrode at any electrode potential, ensuring overall charge-neutrality in the simulation cell. The difference manifests at the local level. Unlike a homogeneously charged surface for which the local net ionic charges at any location compensate the adjacent local net electronic charges, the local compensation does not occur for a heterogenous surface, because the overlapping double layers determine the local ϕ and hence the local accumulation of ionic charges. For example, the local ρ_{ion} above the NP top amounts to 0.006 e/nm^3, three orders of magnitude lower than the local $\Delta\rho_{\mathrm{e}}$ which is as high as 6 e/nm^3. This is because the local ϕ near the NP top surface is not only affected by the local electronic charge density at the NP top surface, but also influenced by the whole heterogeneous surface, including the highly negatively charged support surface. This double-layer overlap effect appears more pronounced for the region that has similar distance to the NP and the support, where ϕ and ρ_{ion} reach zero, indicated by the white color between the blue and red color in Figure 17(c). It is worth noting that the Debye length is a good indicator for the strength of the double-layer overlap effect. For more concentrated solutions, the Debye length is reduced, leading to a weakened double-layer overlap.

In the following, we conduct a parametric study on the influence of NP size and coverage on the electronic charge redistribution.

(1) NP size: A larger NP has a smaller magnitude of redistributed charge density, which is caused by two factors. Firstly, larger NP has higher work function than smaller NP. Therefore, the work function difference between Ag NP and Au support is reduced. Secondly, for the larger NP, the distance between NP top and support is larger and, therefore, the capacitance is lower.

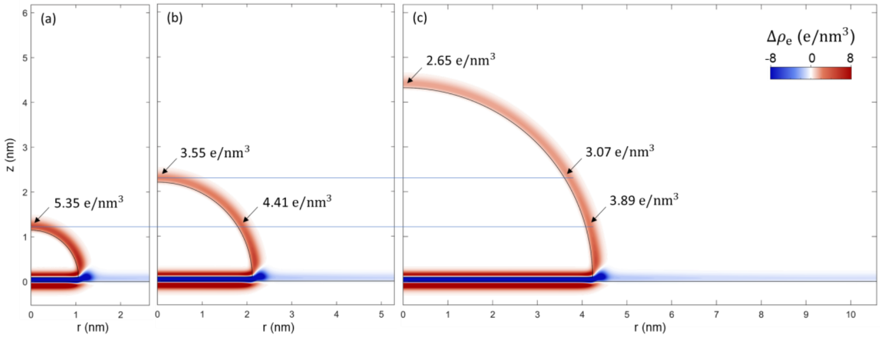

Figure 19. Charge redistribution for three NP radii: (a) 1 nm, (b) 2 nm, (3) 4 nm. The electrolyte concentration is 1 mM. The NP coverage is kept constant at 16%. The supported NP electrode is kept at the global PZC.

(2) NP proximity: The higher the NP coverage, the closer the NPs, the weaker the charge redistribution. This is due to the fact that dipoles induced by charge redistribution at external surfaces tends to repel each other and reduce its magnitude when the NPs are closer to each other.

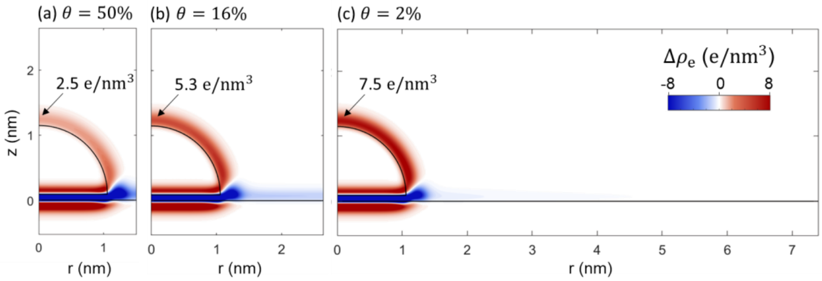

Figure 20. Charge redistribution for three NP coverages: (a) 50%, (b) 16%, (c) 2% corresponds to R_{sup} equal to 7.4 nm, 2.6 nm and 1.45 nm. The NP radius is kept constant at 1 nm. The electrolyte concentration is 1 mM. The supported NP electrode is kept at the overall charge-neutral state.

4.4.4. Diving deeper: two charging mechanisms

Upon contact, the initially different Fermi levels of separate uncharged catalyst NP and uncharged support shift to the final equilibrated Fermi level of supported catalyst NP. Given the equivalence of the Fermi level and the electrode potential, *i.e.*, $E[\text{vs. SHE}] = -\frac{\epsilon_\text{F}-\epsilon_\text{F,SHE}}{e_0}$, the contact of catalyst NP and support shifts their electrode potentials from their respective PZC to the global PZC. The contact-induced charge redistribution is calculated by subtracting the charge density of supported catalyst system by charge densities of the bare support and the unsupported catalyst, each at its potential of zero charge. This process is expressed in Eqn. (66) and illustrated schematically in Figure 21(a). It may seem intuitive to relate the excess charge at the supported NP's outer surface to the shift of electrode potential, i.e., as the electrode potential deviates from the potential of zero charge, the amount of surface charge naturally changes. However, this straightforward reasoning warrants closer examination. Are there any missing considerations? Could specific features of the supported NP system challenge this assumption? I will test the validity of this seemingly-obvious causality in two ways.

In the first way, as illustrated in Figure 21(b), the uncharged NP and uncharged support are evaluated separately. Their electrode potentials are shifted to the GPZC, and it will be checked if the resulting amount of surface charge is the same as that exerted by contact electrification. The second way is described in Figure 21(c). I eliminate the hypothesized cause (Fermi-level shift) and see if the outcome (surface charging) remains. Specifically, the same electrode potential (GPZC) is applied to all the three electrodes. In the absence of electrode-potential shift, it will checked if any charge redistribution occurs by simply placing the NP and support adjacent to each other.

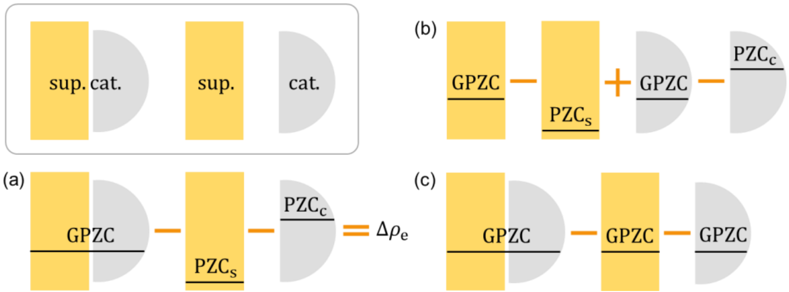

Figure 21. (a) Calculation of the electron redistribution upon contact. The initial electrode potential of support, $\mathrm{PZC_s}$, and of catalyst, $\mathrm{PZC_c}$, the global PZC of supported catalyst, GPZC. (b, c) Two ways to test the causal relation of electron redistribution and Fermi-level shift.

Since in the following paragraphs, we will compare the charge densities between different systems (unsupported catalyst NP, bare support, supported catalyst NP) fixed at various electrode potentials (GPZC, $\mathrm{PZC_c}$, $\mathrm{PZC_s}$, or arbitrary E), it is expedient to first introduce a naming convention (see Figure 22). We use $\mathrm{x}(E)$ to denote the system x (c, s, sc) at electrode potential E. For example, $\mathrm{c(PZC_c)}$ denotes the unsupported catalyst NP at its own PZC, $\mathrm{s(PZC_s)}$ represents the bare support at its own PZC, and $\mathrm{sc(GPZC)}$ expresses the supported catalyst NP system at the global potential of zero charge.

Figure 22. Naming convention of $\Delta\rho_1$ to $\Delta\rho_5$. The right most column shows the charge density difference plot for supported Ag NP at Au surface, calculated at electrolyte concentration of 1 mM.

The first way follows these steps: (a) Change the electrode potential of an unsupported charge-neutral NP to the global PZC, and quantify the additional surface charge by calculating the charge density difference, *viz.*, $\Delta\rho_1 = \rho_\mathrm{e}(\mathrm{c(GPZC)}) - \rho_\mathrm{e}(\mathrm{c(PZC_c)})$, shown in the first row of Figure 22. (b) Change the electrode potential of a bare support to the global PZC, and calculate $\Delta\rho_2 = \rho_\mathrm{e}(\mathrm{s(GPZC)}) - \rho_\mathrm{e}(\mathrm{s(PZC_s)})$, shown in the second row of Figure 22. (c) Sum up the charge density difference of unsupported NP and bare support, *viz.*, $\Delta\rho_3 = \Delta\rho_1 + \Delta\rho_2$ (the third row of Figure 22). (d) Denote the charge density difference of a supported NP system compare to separate uncharged NP and support as $\Delta\rho_4 = \rho_\mathrm{e}(\mathrm{sc(GPZC)}) - \rho_\mathrm{e}(\mathrm{c(PZC_c)}) - \rho_\mathrm{e}(\mathrm{s(PZC_s)})$, shown in the fourth row. (e) Check if $\Delta\rho_3$ is identical to $\Delta\rho_4$ at the respective external surfaces of NP and support, *viz.*, $\Delta\rho_5 = \Delta\rho_4 - \Delta\rho_3$, shown in the fifth row. If it turns out that $\Delta\rho_5$ at the external surfaces is not equal to 0, then a certain proportion of charging in $\Delta\rho_4$ cannot be explained by the shift of electrode potential.

As seen from the right most column in Figure 22, there is a clear difference between $\Delta\rho_4$ and $\Delta\rho_3$ at the NP external surface. This phenomenon can be explained by recalling that, for any metal surface, the amount of charging is not solely determined by the magnitude of the Fermi-level shift, but it also relies on the capacitance. The distinctive characteristic of the supported NP system lies in the close proximity of the two electronic conductors—the external surfaces of the NP and the support can be regarded as two plates of a “parallel” capacitor with water as a dielectric medium sandwiched between them (please see Figure 18). In contrast, for separate NP and support, there exists no such “parallel” capacitor. In the process of Fermi-level equilibration that leads to $\Delta\rho_4$, the Fermi level of the NP and that of the support shift to opposite directions. This potential difference results in dielectric charging of the “parallel” capacitor consisted of the NP and the support, constituting the difference between $\Delta\rho_4$ and $\Delta\rho_3$. In other words, $\Delta\rho_4$ is the combination of two contributions, namely ionic double-layer charging, $\Delta\rho_3$, and dielectric support–NP charging, $\Delta\rho_5$.

Having studied $\Delta\rho_1$ to $\Delta\rho_5$ for the case of 1 mM solution, I proceed to analyze the cases of 100 mM and 0 mM. Figure 23 shows that, at the external surfaces, the relative magnitude of $\Delta\rho_3$ and $\Delta\rho_5$ depends on ion concentration. At 100 mM, $\Delta\rho_3 > \Delta\rho_5$, whereas at 0 mM, $0 = \Delta\rho_3 < \Delta\rho_5$. The rationale is as follows: the double layer can be regarded as one layer of electronic charge in the electrode and another layer of ionic charge in the electrolyte. At higher electrolyte concentration, the effective thickness of the double layer is smaller, producing higher difference capacitance. Conversely, at zero concentration, the effective thickness is infinitely large, corresponding to zero differential capacitance, meaning that no matter how the electrode potential changes, there will be no ionic double-layer charging, *viz.*, $\Delta\rho_3 = 0$. That means, for the 0 mM scenario, the charging is solely contributed by the dielectric NP-support charging, *viz.*, $\Delta\rho_4 = \Delta\rho_5$, as shown in Figure 23(b). Increasing the concentration from 0 mM to 1 mM and up to 100 mM decreases the effective thickness of double layer. This reduction results in higher differential capacitance, leading to a larger $\Delta\rho_3$, while $\Delta\rho_5$ decreases correspondingly.

To sum up, contact electrification of NP and support in electrochemical environment is composed of two charging mechanisms: ionic double-layer charging and dielectric support–NP charging. The relative magnitude of the two contributions depends on the bulk ion concentration.

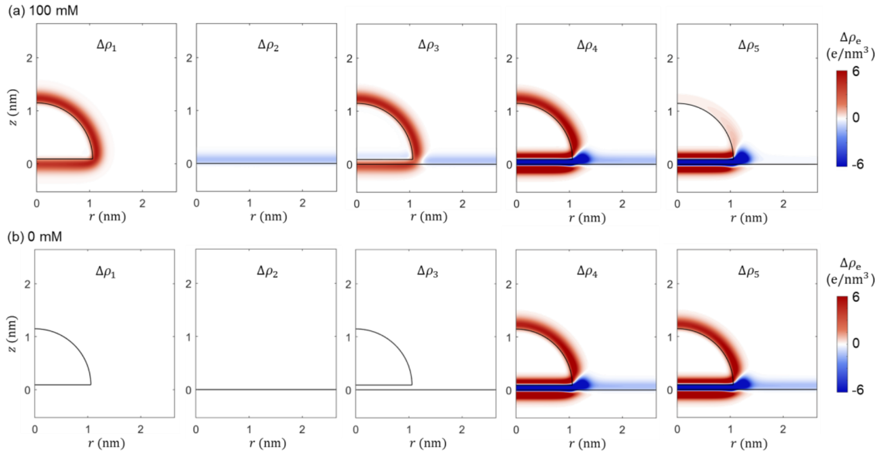

Figure 23. Charge density difference plot at electrolyte concentration of (a) 100 mM, (b) 0 mM.

The second way follows this logic: under fixed electrode potential, can the simple act of placing the NP adjacent to the support cause charge redistribution? Is $\Delta\rho_5 = \rho\big(\mathrm{sc}(\mathrm{GPZC})\big) - \rho\big(\mathrm{c}(\mathrm{GPZC})\big) - \rho\big(\mathrm{s}(\mathrm{GPZC})\big)$ nonzero at the external surface? The red (and blue) shades around the NP circumference (and support surface) clearly substantiate this speculation. How can the electron density redistribution occur when the Fermi level is fixed? This is due to the fact that electric potential distribution in the aqueous dielectric medium between the two plates of the “parallel capacitor” changes in the process of bringing the NP and support closer, giving rise to the charge redistribution. As can be seen in Figure 24(a), the unsupported NP fixed at GPZC is positively charged, so the ϕ around the NP is positive, only decaying to zero after sufficient ionic screening at long distances away from the NP. Conversely, the support fixed at GPZC is negatively charged; the negative ϕ outside the support converges to zero at large distances. Once the support is placed underneath the nanoparticle, these two conductors form a parallel capacitor, reshaping the ϕ distribution around the composite electrode. Correspondingly, the electric field changes significantly when putting NP and support together, as shown in Figure 24(c). The variation of ϕ along an arc at a distance of 0.5 nm from the composite electrode surface is shown in Figure 24(b). Compared with the positive ϕ around the unsupported NP, ϕ around the supported NP shifts to negative values at very short distance from the NP, as shown by the orange curve. In conclusion, the close proximity between the NP and the support perturbs the electric potential and field, leading to electron redistribution.

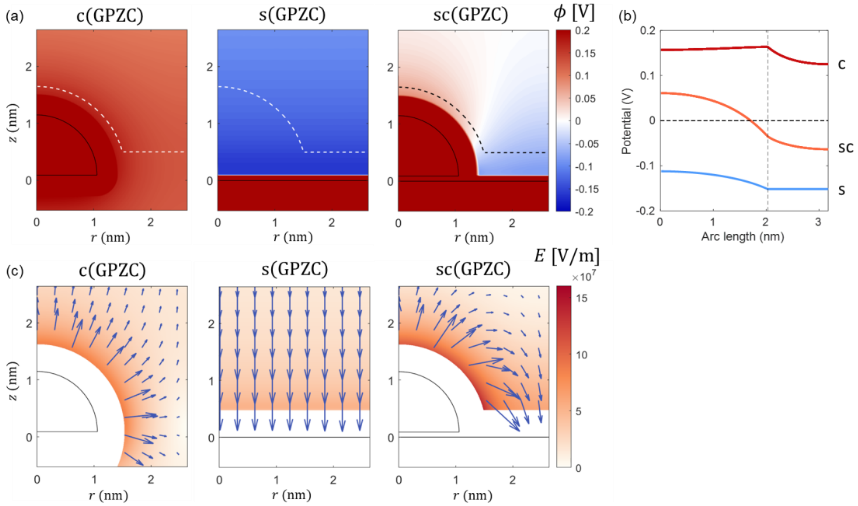

Figure 24. (a) Electric potential distribution for unsupported NP, bare support, and supported NP at the same electrode potential $E = \mathrm{GPZC}$. The dashed lines indicate an arc at a distance of 0.5 nm from the supported NP electrode surface. The electric potential profiles along the arc are shown in (b). (c) Electric field magnitude (red color) and direction (blue arrow) for unsupported NP, bare support, and supported NP at the same electrode potential $E = \mathrm{GPZC}$. Note that we only plot the electric field outside the outer Helmholtz plane.

We have analyzed $\Delta\rho_5$ for the system under applied potential $E = \mathrm{GPZC} = -0.09\ \mathrm{V_{SHE}}$. A natural question arises. Will $\Delta\rho_5$ change with applied electrode potential? We show $\Delta\rho_5$ at a range of E in Figure 25, and compare the cases of 1 mM electrolyte concentration and pure water, shown in Figure 25. It is obvious that $\Delta\rho_5$ changes with E for the 1 mM case, in contrast to the invariant $\Delta\rho_5$ for the pure water case. It is shown that the potential profiles along the arc for the pure water case only shift upwards or downwards without changing its shape (see Figure 25(d)), however, for the case of electrolyte solution, the shape of the potential profile also changes (see Figure 25(b)), due to the dependence of differential double-layer capacitance and thereby ionic screening on E.

This observation signifies the complementary feature of ionic double-layer charging ($\Delta\rho_3$) and dielectric NP–support charging ($\Delta\rho_5$), *viz.*, $\Delta\rho_4 = \Delta\rho_3 + \Delta\rho_5$. In pure water, there is no ionic double-layer charging, so $\Delta\rho_5$ is always identical to $\Delta\rho_4$. In ionic solution, the differential double-layer capacitance and thus the ionic charging vary with E, resulting in a E-dependent dielectric charging $\Delta\rho_5$.

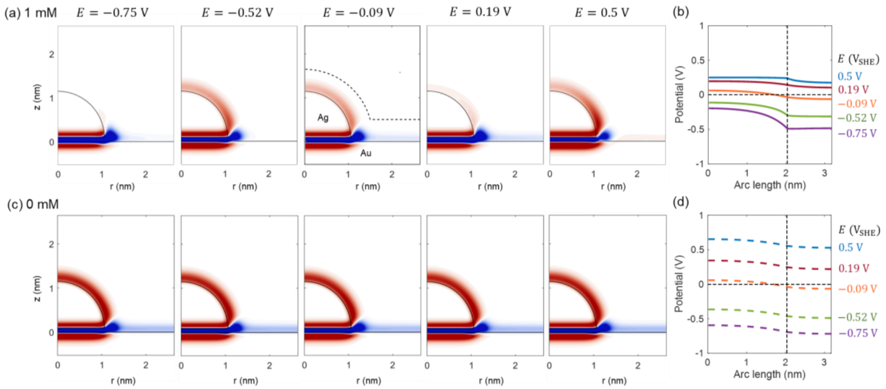

Figure 25. $\Delta\rho_5$ at a range of electrode potential for electrolyte concentration of (a) 1 mM, and (c) 0 mM. The electric potential profile along the arc is shown in (b) and (d).

With the following derivations, we will prove that for an arbitrary E, $\Delta\rho_5(E) = \Delta\rho_5(\mathrm{GPZC})$ holds for the case of pure water and generally does not hold for the case of finite electrolyte concentration.

$$
\begin{aligned}
&\Delta\rho_5(E) \\
&= \Delta\rho_5(\mathrm{GPZC}) + \Delta\rho_5(E) - \Delta\rho_5(\mathrm{GPZC}) \\
&= \Delta\rho_5(\mathrm{GPZC}) + \left[\rho\big(\mathrm{sc}(E)\big) - \rho\big(\mathrm{c}(E)\big) - \rho\big(\mathrm{s}(E)\big)\right] \\
&\qquad - \left[\rho\big(\mathrm{sc}(\mathrm{GPZC})\big) - \rho\big(\mathrm{c}(\mathrm{GPZC})\big) - \rho\big(\mathrm{s}(\mathrm{GPZC})\big)\right] \\
&= \Delta\rho_5(\mathrm{GPZC}) + \left[\rho\big(\mathrm{sc}(E)\big) - \rho\big(\mathrm{sc}(\mathrm{GPZC})\big)\right] - \left[\rho\big(\mathrm{c}(E)\big) - \rho\big(\mathrm{c}(\mathrm{GPZC})\big)\right] \\
&\qquad - \left[\rho\big(\mathrm{s}(E)\big) - \rho\big(\mathrm{s}(\mathrm{GPZC})\big)\right].
\end{aligned} \tag{67}
$$

Since the bulk ion concentration is zero, the differential capacitance vanishes. As a result, no charging occurs when the applied potential is varied, i.e.,

$$0 = \rho\big(\mathrm{sc}(E)\big) - \rho\big(\mathrm{sc}(\mathrm{GPZC})\big) = \rho\big(\mathrm{c}(E)\big) - \rho\big(\mathrm{c}(\mathrm{GPZC})\big) = \rho\big(\mathrm{s}(E)\big) - \rho\big(\mathrm{s}(\mathrm{GPZC})\big). \tag{68}$$

Finally, we arrive at

$$\Delta\rho_5(E) = \Delta\rho_5(\mathrm{GPZC}). \tag{69}$$

4.4.5. Two new characteristic potentials: PZLeC and PZLiC

In section 4.4.3, local electro-ionic perturbations under constant charge condition is thoroughly studied. In the realm of electrocatalysis, however, experiments are performed under controlled electrode potential, E, *i.e.*, under constant potential condition. Hence, it is relevant to investigate how the presence of the support perturbs the electro-ionic properties of the NP under controlled E. We choose the reference to be an unsupported Ag NP at its own PZC ($E = \mathrm{PZC_c} = -0.52$ VSHE), and focus on the region near the NP top surface ($r = 0,\ 0.9\ \mathrm{nm} < z < 2.5\ \mathrm{nm}$), indicated by the black box in the insets of Figure 26. Given charge-neutrality of the unsupported catalyst NP and thus $\rho_{\mathrm{ion}} = \rho_{\mathrm{ion}}^{\mathrm{c}}(\mathrm{PZC_c}) = 0$, this choice of reference offers the convenience to represent the support-induced ρ_{ion} perturbations by the actual ρ_{ion} for the supported NP electrode, viz., $\Delta\rho_{\mathrm{ion}} = \rho_{\mathrm{ion}}^{\mathrm{sc}}(\mathrm{PZC_c}) - \rho_{\mathrm{ion}}^{\mathrm{c}}(\mathrm{PZC_c}) = \rho_{\mathrm{ion}}^{\mathrm{sc}}(\mathrm{PZC_c})$.

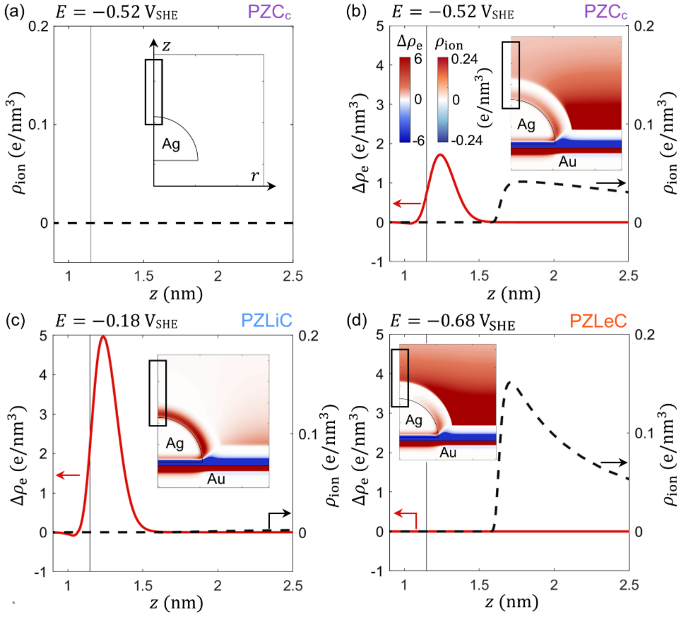

Figure 26. Impact of Au support on local electronic and ionic charge densities of supported Ag NP under potential control, in 1 mM KClO4 solution and $\theta = 16\%$. The NP jellium edge at $z \approx$

1.15 nm is indicated by a vertical line. (a) Unsupported NP at $E = \mathrm{PZC_c} = -0.52\ \mathrm{V_{SHE}}$. (b) Supported NP at $E = \mathrm{PZC_c}$. (c) Supported NP at $E = \mathrm{PZLiC} = -0.18\ \mathrm{V_{SHE}}$. (d) Supported NP at $E = \mathrm{PZLeC} = -0.68\ \mathrm{V_{SHE}}$.

Meanwhile, in reference to the ρ_e of the unsupported NP, the support-induced ρ_e perturbation is calculated by

$$\Delta\rho_\mathrm{e} = \rho_\mathrm{e}^\mathrm{sc}(\mathrm{PZC_c}) - \rho_\mathrm{e}^\mathrm{c}(\mathrm{PZC_c}). \tag{70}$$

Figure 26(b) reveals stark support-induced perturbations in the electro-ionic conditions of the NP. The red curve indicates a surplus of positive electronic charges at the top surface, caused by the electronic MSI, similar to the situation in Figure 17. While one might intuitively expect that an excess positive electronic charge would cause an accumulation of anions, it is instead observed that a cation excess exists near the NP, denoted by the black dashed curve. How can the positively charged surface attract cations? This seeming contradiction is rationalized by the ionic MSI. The EDLs of the NP and the support overlap at the heterogeneous surface and thereby co-determining the distribution of electric potential. As the applied electrode potential $(-0.52\ \mathrm{V_{SHE}})$ is more negative than the PZC of the Au support $(0.19\ \mathrm{V_{SHE}})$, the strongly negatively charged support creates a negative potential region that extends above the support and the NP. This is confirmed by the ϕ profile along a path located 0.5 nm above the electrode, illustrated by the purple curve in Figure 27(a). Consequently, cations accumulate around the NP, despite its net positive electronic charges. To summarize, although global electroneutrality in the simulation cell always holds, locally at the NP top, electronic and ionic excess charges of the same polarity are generated by the coupled electro-ionic MSI. This surprising finding constitutes a major result of the study.

For a homogeneous electrode, the PZC is the characteristic electrode potential corresponding to the charging state of zero electronic and ionic excess charges. Because of the support-induced electro-ionic perturbations, the $\mathrm{PZC_c}$ of the unsupported NP $(-0.52\ \mathrm{V_{SHE}})$ no longer guarantees zero excess charges of the supported NP and thereby fails to indicate its charging state. It is natural to ask whether a new characteristic electrode potential for the supported NP, akin to the $\mathrm{PZC_c}$ for unsupported NP, can be identified. To restore zero ρ_ion above the NP surface, corresponding to $\phi = 0$ in that region (see the blue curve in Figure 27(a)), E must be shifted positively by 0.34 V relative to the $\mathrm{PZC_c}$, as demonstrated in Figure 26(c). The resulting E is defined as the "potential of zero *local ionic* charge" (PZLiC). However, despite the restoration of the local ρ_{ion}, the local ρ_{e} deviates further from the reference value of the unsupported charge-neutral NP, as revealed by plotting $\Delta\rho_{\mathrm{e}} = \rho_{\mathrm{e}}^{\mathrm{sc}}(E) - \rho_{\mathrm{e}}^{\mathrm{c}}(\mathrm{PZC_c})$ in Figure 26(c). In contrast, to restore the local ρ_{e} at the NP top surface, E must be shifted in opposite direction by −0.16 V relative to the PZC$_{\mathrm{c}}$, as shown in Figure 26(d). Analogous to the PZLiC, we term this E as the "potential of zero *local electronic* charge" (PZLeC).

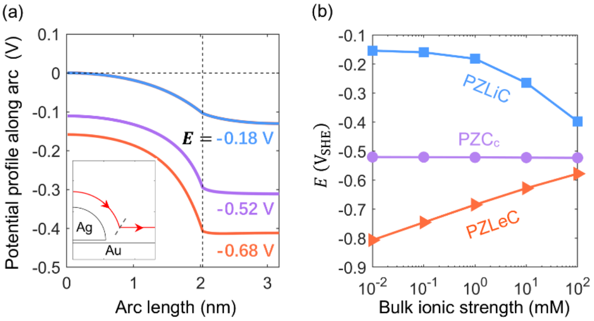

Figure 27. (a) Potential profiles along a path located 0.5 nm from the electrode surface (see the red curve in the inset) in 1 mM KClO$_4$ solution. Each profile is calculated at the electrode potential indicated nearby. (b) Variation of the PZLiC and PZLeC of supported NP as well as the PZC$_{\mathrm{c}}$ of unsupported NP with bulk ionic strength.

While at PZC$_{\mathrm{c}}$ (−0.52 V$_{\mathrm{SHE}}$), the unsupported catalyst NP exhibits both zero electronic and ionic excess charges, we have demonstrated that no single E exists for the supported NP that ensures the absence of both electronic and ionic excess charges. Moreover, the PZLiC and PZLeC deviate from the PZC$_{\mathrm{c}}$ in opposite directions, with a difference between them reaching up to 0.5 V. Consequently, the support-induced electro-ionic perturbations yield *qualitatively* different electrochemical conditions for catalyst NPs, that are expected to strongly influence their electrocatalytic properties.

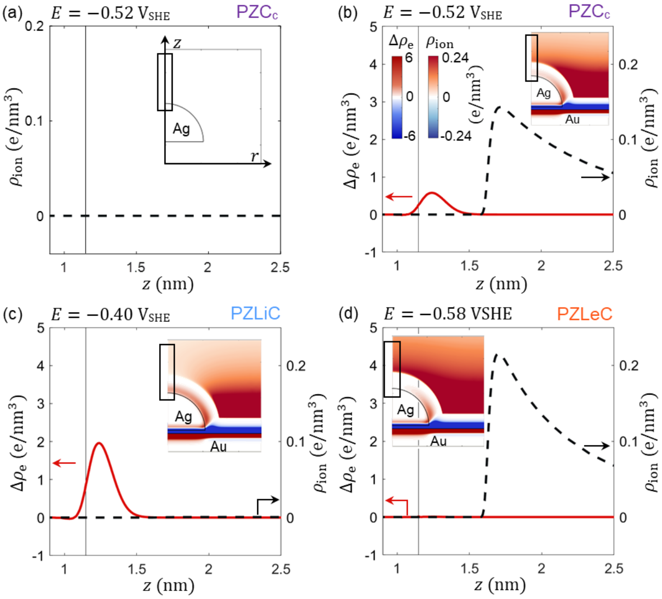

Figure 28. Impact of Au support on the local electronic and ionic charge densities of supported Ag NP under potential control. Same collection of plots as in Figure 26, but at an electrolyte concentration of 100 mM. Note that the electrolyte concentration shifts the occurrence of the PZLiC in (c) (from –0.18 V$_{\mathrm{SHE}}$ in Figure 26 to –0.40 V$_{\mathrm{SHE}}$) and of the PZLeC in (d) (from –0.68 V$_{\mathrm{SHE}}$ in Figure 26 to –0.58 V$_{\mathrm{SHE}}$).

The electro-ionic perturbations around the NP are most pronounced in dilute electrolyte. In the case of 1 mM concentration (Figure 26(b)), ρ_{e} at the NP top alters by approximately $2\ \mathrm{e/nm^3}$ and the cation concentration nearby increases by a factor of 70 compared to the bulk solution. At higher ionic strength (100 mM, Figure 28), these values decrease to around $0.5\ \mathrm{e/nm^3}$ and a factor of 2. Figure 27 (b) shows the variation of the three characteristic potentials with electrolyte concentration. The PZLiC and PZLeC converge to the PZC$_c$ at high concentration, a result of the electro-ionic decoupling between the NP and support at increased ionic screening. Additionally, the size dependency is shown in Figure 29, where the deviation of the PZLeC from the PZC$_c$ decreases from 0.29 V for a 1 nm radius NP to 0.04 V for a 4 nm radius NP.

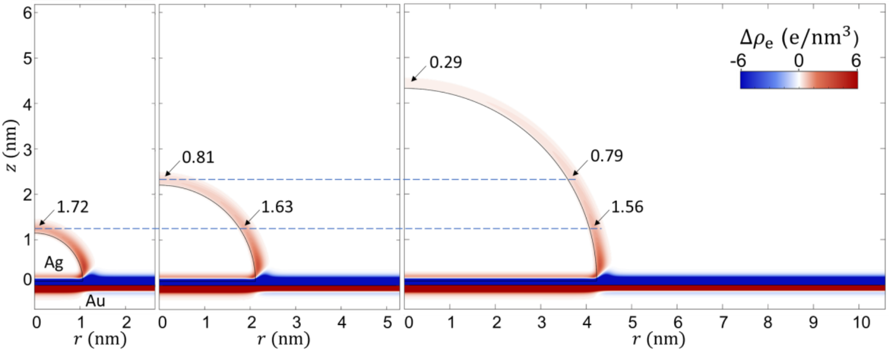

Figure 29. Impact of NP size on charge perturbation under constant potential of PZC$_\mathrm{c}$, $\Delta\rho_\mathrm{e} = \rho_\mathrm{e}^\mathrm{sc}(\mathrm{PZC_c}) - \rho_\mathrm{e}^\mathrm{c}(\mathrm{PZC_c})$, for NPs with R_cat values of 1 nm (left), 2 nm (middle), and 4 nm (right). $\Delta\rho_\mathrm{e}$ at several representative locations is marked in the plots. The value is roughly inversely proportional to the distance from the support surface.

4.4.6. Overall capacitive response

The present modelling framework offers insights into local electro-ionic conditions that are challenging to access experimentally. It is, of course, essential to provide experimentally attainable predictions. An electrochemical analogue of the global Φ in electrolyte environment is the global PZC, which corresponds to the electrode potential at which the overall ρ_ion (and ρ_e) in the electrolyte (and electrode) equals zero. As shown in Figure 16, it follows a similar trend to the global Φ. It is noteworthy that the nonlinear shape of the coverage-dependent global Φ and global PZC signifies the electron redistribution on the *external* surface, as established by a previous study [134].

While capacitance features of planar electrodes have been extensively studied both experimentally and theoretically, little is known about the capacitive response of supported NP systems. The prevailing view on the C_d curve of heterogeneous surfaces suggests that it resembles a linear superposition of the C_d curves of individual constituents. For example, the capacitance of a polycrystalline electrode has been described as a surface-area-weighted average of constituting facets.

Figure 30 shows the calculated C_d of the Au-supported Ag NP system at $\theta = 16\%$ in aqueous 1 mM KClO$_4$ solution (purple line). To facilitate comparison, reference C_d curves for planar gold and silver electrodes are plotted as gold and silver dashed lines, respectively, exhibiting characteristic minima at their respective PZC. The average of the reference C_d curves, weighted with the area fraction, is depicted as a black dotted line. It exhibits two minima, inherited from the two constituents. Surprisingly, the capacitance curve of the supported NP system calculated from our semiclassical model (solid line) reveals a single minimum located at the global PZC of the heterogeneous electrode, in between the two minima of the reference curves. This behavior is in sharp contrast to the simple linear superposition but resembles the characteristics of a homogeneous electrode. This peculiar feature represents a direct signature of electron redistribution and electro-ionic interactions between catalyst NP and support that homogenize the two entities' capacitive response.

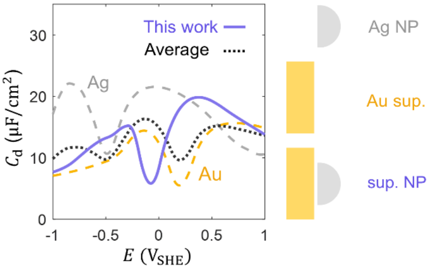

Figure 30. C_d of Au-supported Ag NP electrode at $\theta = 16\%$ in 1 mM KClO$_4$ solution (solid line). The NP has a radius of 1 nm. The dashed lines depict the C_d of Ag NP and planar pc Au electrodes, while the dotted line illustrates a surface-area-weighted average of the two reference curves.

Figure 31 shows that, as the NP size increases, C_d curve of supported NP electrodes progressively develops three peaks and two local minima, resembling the superposition of the capacitance contributions from individual constituents.

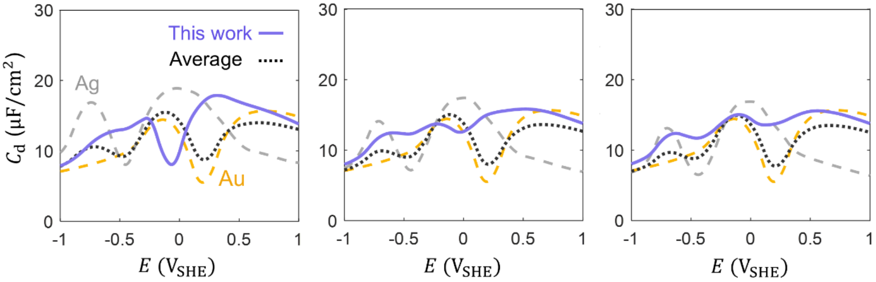

Figure 31. Impact of NP size on C_d of supported NP electrode, for NPs with R_cat values of 2 nm (left), 4 nm (middle), and 6 nm (right). The NP coverage on support is kept constant.

4.5. Summary

In this chapter, we have used the newly developed DPFT model presented in Chapter 2 to study the local electro-ionic conditions at an Au supported Ag NP electrode. We reveal that, upon contact of NP and support, electrons transfer from the silver NP with higher Fermi level to the gold support with lower Fermi level, until the two Fermi levels equilibrate. The energy difference between the final equilibrated Fermi level and the vacuum level is then the global work function of the composite electrode.

In addition to the textbook knowledge that electrons redistribute across the NP–support interface, our results reveal that a “long-range” charging exists at the external surfaces of NP and support, leading to a strong electric field pointing from the NP to the support. This finding is highly relevant because catalytic reactions occur at the external surface of NP, instead of the buried interface between NP and support. The excess charges, ion distribution and electric field may affect the catalytic activity and selectivity.

In order to visualize the electron redistribution, we have calculated the electron density distribution of three systems, namely an unsupported NP, a bare support, and a supported NP. The three systems have been examined under the conditions of constant charge and constant potential. The constant-charge condition refers to the case that the unsupported NP and the bare support before contact are both charge-neutral, and the supported NP still remains overal charge-neutral. This scenario holds relevant in vacuum, gas phase, or colloidal suspensions in liquid. The constant-potential condition means that the three systems are all controlled at the same electrode potential, which mimics the setting of electrocatalysis.

Under constant-charge condition, parametric studies reveal that NPs with larger size have fewer excess charges at the NP top surface, because the long-range charging is inversely proportional to the distance between the NP top surface and the support surface. The charge redistribution creates an effective net dipole, with the Ag NP surface being the positive end and the Au surface being the negative end. For systems of high NP coverage, the long-range charging is reduced, because the effective dipoles, if brough closer, tend to repel each other and thus reduce its own magnitude.

As we delve deeper into electron redistribution under constant-potential condition, we find out that there exist two charging mechanisms, namely ionic double-layer charging and dielectric support–NP charging. The close proximity of the external surfaces of NP and support form a capacitor, with water as a dielectric medium sandwiched between them. The potential difference caused by Fermi-level equilibration results in dielectric charging of the capacitor of the NP and the support. This explains why, although the unsupported NP and the bare support have already been set at the final electrode potential, simply placing the NP and support in contact still leads to long-range charging.

We then reveal strong support-induced perturbations of electron and ion densities at the electrocatalyst surface under controlled electrode potential. Unlike for the case of planar electrode, where in every local position the excess ionic charges in the solution phase compensate the excess electronic charges at the metal surface, we reveal that in supported NP systems, the local charge neutrality breaks down—electronic and ionic charges of the same sign exist at the NP–solution interfacial region. This renders the PZC, the most seminal concept in electrochemistry, an insufficient descriptor of the charge state of the supported NP system. We therefore introduce two new descriptors, namely the potential of zero local electronic charge and the potential of zero local ionic charge, each characterizing the electrode potential at which the local electronic or ionic excess charges are zero.

Having inspected the local properties of the supported NP system, we proceed to study global charging characteristic by calculating differential capacitance curves. We found that the double-peak feature gradually transitions to triple-peak feature as the NP radius increases from 1 nm to 6 nm.

In summary, the findings presented in this chapter demonstrate that electronic and ionic MSIs are strongly coupled in supported electrocatalyst systems. We therefore propose to denote them as electro-ionic MSI (EIMSI).

5. Comparison of DPFT with DFT calculations

5.1. Introduction

The state-of-the-art methodology for calculation of electronic properties is Kohn–Sham DFT. Explicitly considering orbitals, Kohn–Sham DFT is more accurate than orbital-free DFT used in the DPFT framework. Therefore, it provides a good benchmark of the DPFT results of electronic perturbations in supported NP systems. In this Chapter, we will first present the fundamental principles of DFT and describe the setup of our DFT calculations. We then provide direct comparison between the DFT and DPFT, focusing on key observables such as the global work function and charge density difference.

5.2. Fundamental aspects of DFT

Nowadays, DFT is the most widely used quantum mechanical approach for computing the electronic structure of materials, enabling the prediction of a broad range of physical and chemical properties. A comprehensive introduction can be found in standard textbooks [193,194]. In this section, we briefly revisit the theoretical foundations of DFT.

The formal basis of DFT was established by the two Hohenberg–Kohn (HK) theorems [195]. The first HK theorem states that the ground-state properties of a many-electron system are uniquely determined by its electron density, which depends only on three spatial coordinates. This theorem enables a dramatic simplification: it reduces the complexity of a many-body quantum system from dependence on a 3N-dimensional wavefunction to a function of just three spatial variables. This is achieved through replacing the exact wave function with electron density $n_\mathrm{e}(r)$, achieving a high accuracy at a low computational cost.

The ground-state energy E, a unique functional of the electron density, can be written as

$$E[n_\mathrm{e}(r)] = T[n_\mathrm{e}(r)] + V_\mathrm{ee}[n_\mathrm{e}(r)] + \int n_\mathrm{e}(r) V_\mathrm{ext} \mathrm{d}r. \tag{71}$$

Here, $T[n_\mathrm{e}(r)]$ is the kinetic energy of electrons, $V_\mathrm{ee}[n_\mathrm{e}(r)]$ describes the electron–

electron interaction energy, and the third term accounts for the external potential from atomic nuclei.

The second HK theorem introduces a variational principle: the ground-state electron density minimizes the energy functional, meaning any trial electron density gives an energy higher than the ground state energy,

$$E[n_{\mathrm{e}}(r)] \leq E\left[n_{\mathrm{e,trial}}(r)\right]. \tag{72}$$

Building upon this foundation, Kohn and Sham proposed a practical implementation by mapping the interacting electron system to a fictitious system of non-interacting electrons moving in an effective potential [141].

$$\left(-\frac{1}{2}\nabla^2 + V_{\mathrm{eff}}(r)\right)\psi_i(r) = \varepsilon_i \psi(r). \tag{73}$$

where $\psi_i(r)$ are single-electron wave functions. Within the Kohn–Sham scheme, the effective potential includes the external potential, the Coulomb interactions, and the exchange–correlation interactions,

$$V_{\mathrm{eff}}(r) = V_{\mathrm{ext}}(r) + \int \frac{n_{\mathrm{e}}(r)}{|r - r'|} \mathrm{d}r' + V_{\mathrm{XC}}[n_{\mathrm{e}}(r)]. \tag{74}$$

A major challenge in KS DFT lies in approximating the exchange–correlation functional, defined as

$$V_{\mathrm{XC}}[n_{\mathrm{e}}(r)] = \frac{\delta E_{\mathrm{XC}}}{\delta n_{\mathrm{e}}}. \tag{75}$$

The simplest approach is the local density approximation (LDA), which assumes that the exchange–correlation energy at each point depends only on the local density,

$$E_{\mathrm{XC}}^{\mathrm{LDA}}[n_{\mathrm{e}}] = \int \varepsilon_{\mathrm{XC}}(n_{\mathrm{e}}) n_{\mathrm{e}}(r) \, \mathrm{d}r. \tag{76}$$

To account for density inhomogeneities, the generalized gradient approximation (GGA) includes terms dependent on the density gradient,

$$E_{\mathrm{XC}}^{\mathrm{GGA}}[n_{\mathrm{e}}, \nabla n_{\mathrm{e}}] = \int \varepsilon_{\mathrm{XC}}(n_{\mathrm{e}}, \nabla n_{\mathrm{e}}) n_{\mathrm{e}}(r)\, \mathrm{d}r. \tag{77}$$

This gives rise to a new class of density functionals, including PBE, PW91, RPBE, and revPBE [196]. In this thesis, we utilize the PBE functional.

Meta-GGA functionals extend this idea by including second derivatives (e.g., the Laplacian, $\nabla^2 n_{\mathrm{e}}$) [197]. Hybrid functionals go a step further by incorporating a fraction of exact exchange energy calculated from Hartree–Fock theory [198]. These often offer improved accuracy for a wide range of systems.

An alternative formulation is orbital-free DFT, which seeks to express all relevant energies as functionals of the density alone [199]. While less widely used than KS-DFT, it is closer in spirit to the original HK theorems. Within the DPFT framework, orbital-free DFT is utilized to describe the electrode part [111].

5.3. Setup of Kohn–Sham DFT calculations

Structure relaxations and single point energies were calculated using the Vienna Ab Initio Simulation Package (VASP) commercial software [200]. The projector-augmented wave (PAW) pseudopotential was utilized to treat the core electrons while the Perdew, Burke and Enzerhoff (PBE) exchange-correlation functional of the generalized gradient approximation (GGA) was used for describing the electron interactions [155,196]. Grimme D3 dispersion correction using Becke-Johnson damping function was applied [156]. A plane wave cutoff energy of 400 eV for the Kohn-Sham one electron valence eigenstates was adopted for all calculations. The lattice constants of the Ag and Au structures was fixed to the value obtained from optimizing with DFT this constant for the bulk metal. The computed lattice constants for the bulk Ag and Au are 4.066 and 4.098 Å which compares well with the experimental value of 4.086 and 4.078 Å found in the literature [157].

The reciprocal space for the large supported NP system was sampled with a Γ-point 1 × 1 × 1 mesh. Electronic structure calculations were converged to an energy of 1E-6 eV. A Fermi smearing of σ = 0.05 eV was utilized. Charge density is updated with Pulay-mixing method and AMIX = 0.02 was used. Structural relaxation was carried out until the maximal residual force was < 0.01 eV/ Å.

The solvent environment was modeled using an implicit solvation model, as implemented by the VASPsol package, with a dielectric constant of 78.4 [117,158].

Pre-processing of input structures and post-processing of calculation results are done with the help of ASE, VESTA and VASPKIT packages [201–203].

The DFT input structure of supported NP is built to be comparable to our DPFT model. The Ag NP adopts a truncated octahedron structure, cut in half, with a height of approximately 1 nm and consisting of 94 atoms, mimicking the half-sphere geometry used in our DPFT model. The support slab consists of 4 layers of Au atoms. The number of Au atoms in the slab depends on the target Ag NP coverage on the slab. For instance, the base case of 16% coverage corresponds to 224 Au atoms. A vacuum layer with thickness 20 Å is introduced between the top of the Ag NP and the periodic Au slab to avoid spurious interactions between them.

Structural relaxation is first performed for the individual NP and the individual support. After obtaining the relaxed structures, the NP and the support are combined to form the supported NP system, which is then relaxed again. Based on the optimized structures, global work function and charge density difference plot can be obtained.

To calculate the global work function, a static calculation should be conducted for the supported NP system. The LVHAR tag must be set to TRUE in order to output the electrostatic potential into the LOCPOT file. The global work function is defined as the difference between the vacuum level and the Fermi level. Since dipole correction is applied, two flat regions of the electrostatic potential appear in the vacuum part of the simulation cell. The vacuum level should be taken from the region farthest from the supported NP, as it is less influenced by the system.

To calculate the charge density difference, three separate static calculations should be performed: one for the isolated NP, one for the bare support, and one for the combined supported NP system. In each calculation, the LCHARG tag must be set to TRUE to ensure the CHGCAR file is written. After obtaining the three CHGCAR files, the charge density difference can be computed using VASPKIT [203].

My GitHub repository (link) archives (1) python scripts for building models in POSCAR format, (2) VASP Input files (INCAR, POSCAR, KPOINTS), and (3) python script for postprocessing charge density differences.

5.4. Computation Results

5.4.1. Coverage-dependent global work function

Figure 32 presents the top view of supported NP systems at five different coverages , ranging from 15% to 62%. The Au support has four layers of atoms. The number of Au atoms varies with coverage and is 896, 528, 360, 256, and 224 atoms, respectively, corresponding to increasing coverage.

The DFT results of coverage dependent global work function of the supported NP in vacuum not only follow the same trend but also show quantitative agreement with the DPFT results, as shown in Figure 33. Specifically, the DPFT and DFT results differ by 0.1 eV at zero coverage (pure gold support) and by 0.2 eV at high coverage. In the DPFT model, we calibrated the parameters to reproduce the experimental work function of polycrystalline gold, which is 5.20 eV [161,162]. However, we used Au(111) surface in the DFT model, with a calculated work function of 5.10 eV. Considering this intrinsic offset of 0.1 eV, the maximal deviation of the DPFT and DFT results is only 0.1 eV, which is well within the typical range of DFT error.

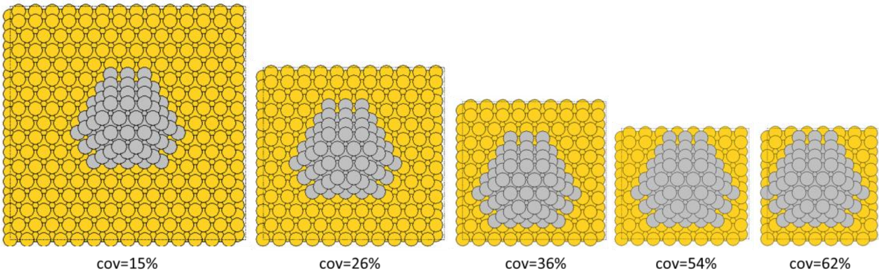

Figure 32. Top view of supported NP systems at different coverages. The Au support has four layers of atoms.

Additionally, both DPFT and DFT simulations show a reduction in the work function of Ag NP compared to the planar Ag(111) surface. The work function of the Ag(111) surface is 4.60 eV in DPFT and 4.51 eV in DFT. For a halved Ag NP with a 1 nm radius, the work function is reduced to 4.23 eV in DPFT and 4.18 eV in DFT.

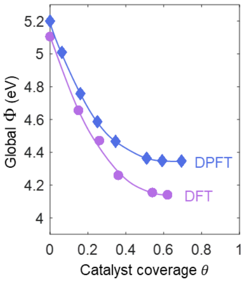

Figure 33. Comparison between DPFT and DFT results of coverage-dependent global work function in vacuum.

5.4.2. Charge density difference plot

The Ag NP covers about 15.5% of the support surface, close to 16% used in the DPFT model. For an isosurface of 0.25 e/nm^3, the comparison between Figure 34 (a) and (b) clearly shows that the external surface charging is strongly enhanced in the presence of highly polarizable water molecules, corroborating our DPFT results. For quantitative comparison, we choose two slices denoted in Figure 34(c) and plot their charge density difference in Figure 35.

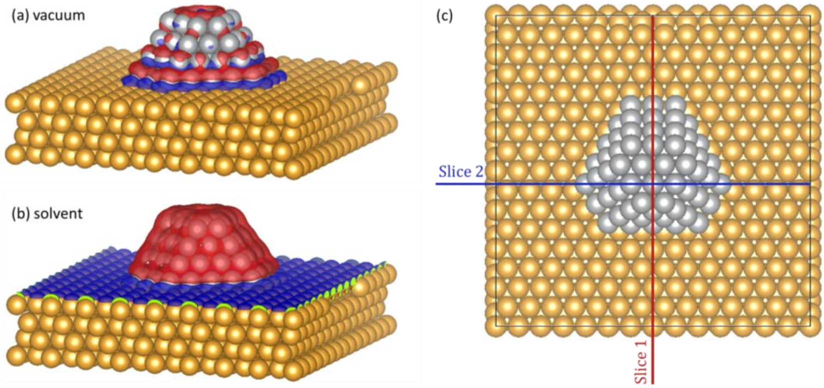

Figure 34. DFT results of charge density difference with an isosurface of 0.25 $\mathrm{e/nm^3}$ in (a) vacuum and (b) solvent environment, visualized by VESTA. [202] For further analysis, two representative slices, highlighted in (c), were selected, and their corresponding charge density differences are presented in Figure 35.

Figure 35 shows the charge density difference, $\Delta\rho_\mathrm{e}$, calculated by DFT and DPFT, with the same color scale for direct quantitative comparison. In vacuum ($\Delta\rho_\mathrm{e,vac}$, left column), we focus on the NP top as a representative region, marked by black boxes in both the DFT slice 1 and the DPFT subfigures. Integrating $\Delta\rho_{\mathrm{e,vac}}$ within the box and normalizing by length yields an additional surface charge density of 0.062 e/nm^2 for DPFT and 0.066 e/nm^2 for DFT, demonstrating quantitative agreement. In an solvent environment ($\Delta\rho_{\mathrm{e,sol}}$, middle column), both the DPFT and DFT results show a much stronger charge redistribution at the external surfaces of the supported NP than in the vacuum environment. While the charge perturbations inside the NP and the support captured by DFT are not present in the DPFT results, taking the difference between $\Delta\rho_{\mathrm{e,sol}}$ and $\Delta\rho_{\mathrm{e,vac}}$ effectively cancels these intrinsic perturbations (right column). This emphasizes the enhancement of external surface charging due to the solvent environment, with the DFT and DPFT results showing good agreement.

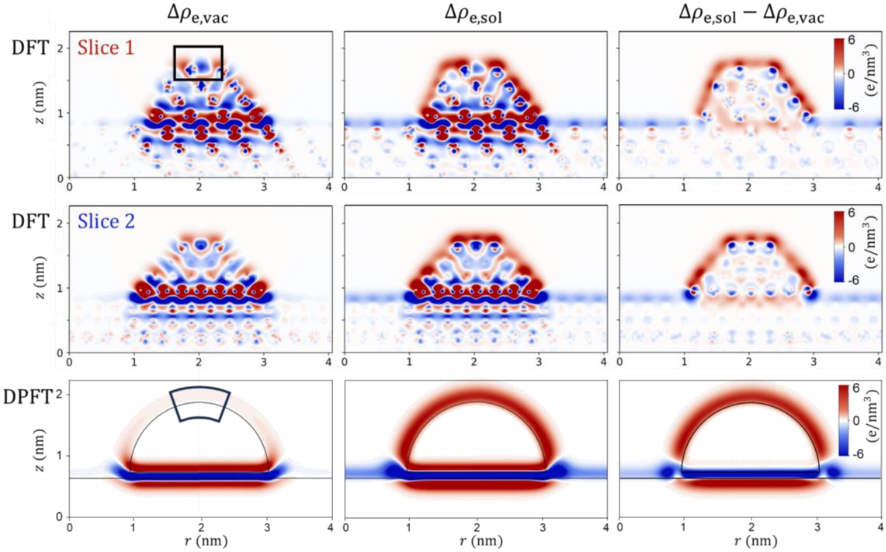

Figure 35. Charge density difference plot for slice 1 (upper row) and slice 2 (middle row) calculated by DFT, and by DPFT (lower row). The charge density difference in vacuum environment, $\Delta\rho_{\mathrm{e,vac}}$, in solvent environment, $\Delta\rho_{\mathrm{e,sol}}$, and the difference between the two, $\Delta\rho_{\mathrm{e,sol}} - \Delta\rho_{\mathrm{e,vac}}$, are shown in the left, middle and right columns, respectively.

The charge redistribution creates a net dipole moment along the *z* direction, with the negative end at the bottom and the positive end at the top. Therefore, this charge redistribution can also be quantified by calculating the total dipole moment in the cell, normalized by the support-NP contact area. As shown in Table 6, DPFT and DFT once again exhibit quantitative agreement.

Table 6: Comparison of the $\Delta\rho_\mathrm{e}$-induced dipole moment from DPFT and DFT results.

	Equation	Vacuum	Solvent
DPFT	$\iint \Delta\rho_\mathrm{e}(r,z)\times z\times 2\pi r\,\mathrm{d}r\mathrm{d}z\,/S_\mathrm{contact}$	0.1844 e/nm	1.500 e/nm
DFT	$\iiint \Delta\rho_\mathrm{e}(x,y,z)\times z\,\mathrm{d}x\mathrm{d}y\mathrm{d}z\,/S_\mathrm{contact}$	0.1877 e/nm	1.426 e/nm
Error		1.8%	-5.2%

Figure 36 shows electron accumulation at the interface of NP and support, and electron depletion at the adjacent regions, serving as a confirmation of the triple-layer structure of $\Delta\rho_\mathrm{e}$ obtained by our DPFT simulations.

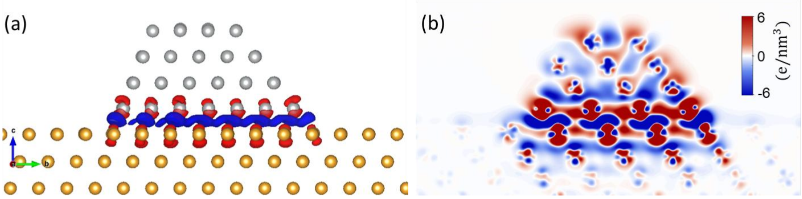

Figure 36. DFT results for the charge density difference plot in vacuum with an isosurface of 2.5 $\mathrm{e/nm^3}$ shown in (a) and a color scale from -6 to 6 $\mathrm{e/nm^3}$ in (b). These plots reveal the triple-layer structure of $\Delta\rho_\mathrm{e}$ at the NP-support contact interface.

5.5. Summary

DFT calculations have been performed on a truncated octahedron Ag NP with a height of 1 nm on an Au(111) slab to benchmark DPFT results. The coverage-dependent global Φ calculated by Kohn–Sham DFT agrees with DPFT predictions, with deviations of only 0.1 eV. In vacuum, the additional electronic charge densities at the NP's top surface calculated by DPFT and Kohn–Sham DFT show quantitative agreement. The solvent-induced enhancement of external-surface charging is further supported by Kohn–Sham DFT calculations with an implicit solvation model. The overall net dipole moment in the simulation cell, resulting from electron redistribution, shows a relative error of 1.8% in vacuum and 5.2% in solution environment when comparing DPFT and Kohn-Sham DFT calculations. Additionally, the triple-layer structure at the contact interface obtained by DPFT is also seen in Kohn–Sham DFT calculations. In summary, the DPFT results are well benchmarked by Kohn–Sham DFT calculations.

6. Effective ion concentration as a descriptor for the local reaction environment of supported NP systems

6.1. Introduction

Structural and compositional variation of NP and support create distinct EDL properties in the vicinity of these components. Neighboring to each other, the two EDLs jointly determine local ion concentrations and electric potential near the NP–support contact, influencing the electrocatalytic activity of the NPs. This chapter first presents the mathematical expression for the effective proton concentration as a LRE descriptor, followed by a parametric analysis of key compositional and structural properties. On the example of gold supported silver NP system, it is studied how support material, size and packing density of NPs, bulk ion concentration and electrode potential affect the LRE descriptor. To further rationalize the impact of LRE on electrocatalytic activity, a second LRE descriptor that incorporates the effect of the local electrostatic potential is proposed. By combining the two reaction-agnostic LRE descriptors with two reaction-specific kinetic parameters, an activity descriptor is introduced. Results are discussed in view of the suitability of the descriptors to be used in the design and optimization of supported nanoparticle-based electrocatalysts for electrochemical applications.

6.1.1. Double-layer overlap effect

As pointed out by Arenz et al. [204], current efforts in optimizing and designing catalysts are focused mainly on the atomic scale. Rarely considered are mesoscopic (from 1 to 100 nm) local reaction conditions that are determined by the overlap of EDLs at catalytic NPs and support. With a few exceptions where mesoscopic EDLs have been brought to light, the structure of overlapping EDLs and their influence on the structure–activity relationships has remained controversial.

With the NP size controlled, the variation of the catalytic activity of supported NPs as a function of interparticle distance is termed particle proximity effect [57,58]. Closer proximity is equivalent to higher NP-covered support surface fraction (NCSF) on the support. Early investigations by Nesselberger *et al.* and Huang *et al.* established the EDL overlap as an underlying mechanism for the particle proximity effect, albeit with differing explanations [57,58].

Nesselberger *et al*. attributed the NP proximity effect to an increased overlap of EDLs from neighboring Pt NPs at smaller interparticle distances [57]. This overlap reduces the potential drop from electrode surface to the inner Helmholtz plane, leading to a weaker electric field in the compact layer of the EDL. A reduced electric field was assumed to lower the coverage of site-blocking oxygen-containing adsorbates, thereby facilitating the ORR. While this study experimentally demonstrated the importance of EDL overlap, the model has several limitations. Firstly, it assumed identical PZCs for Pt and carbon, overlooking their charging characteristics. Secondly, adsorbed oxygen-containing adsorbates not only act as site-blocking species, but also participate as reactants. Therefore, a simple inverse relationship between adsorbate coverage and catalytic performance may not always hold.

The model of Huang *et al*. also captures the overlapping EDLs of Pt NP and carbon support, while it accounts for their distinct surface charging behaviors and the formation of oxygen-containing adsorbates, and rationalizes their net effect on the LRE [58]. Within the potential range relevant to the ORR, the carbon support is positively charged, leading to proton exclusion. For the Pt surface, the non-monotonic surface charging behavior that had been found in an earlier work results in a net negative charge in the relevant potential regime, which leads to proton attraction [205]. Dissimilar charging properties of Pt NP and support jointly determine the EDL structure along the surface. Huang *et al*. thus attributed the particle proximity effect to changes in the local proton concentration, which are regulated by the interplay of the surface charging characteristics of Pt NPs and the support and depend on the NCSF. At higher NCSF, electrostatic properties of Pt NPs will become more dominant and induce higher proton concentrations. A simple Butler-Volmer-type equation was used to calculate the ORR activity [58]. In a subsequent study, Zhang *et al.* coupled a microkinetic model with the EDL overlap model to calculate reaction rates and construct electrocatalytic volcano plots [31]. The latter study explored how the volcano curve can be shifted upward or downward via altering the support material or the bulk electrolyte concentration. The position of the volcano apex remained, however, unchanged upon applying these modifications in model calculations.

Despite recent progress, it remains poorly understood how NP size, NCSF, support material, and electrolyte composition determine the electro-ionic metal–support interactions and the LRE in supported electrocatalyst systems. Gaining a better understanding of these dependencies will be essential for the rational design of electrocatalyst materials for electrochemical devices with high performance and durability.

In this work, we address this need by evaluating the effective ion concentration as the average ion concentration over the reaction plane (RP) of supported NPs, using the solution of the DPFT-based model. For proton-consuming reactions that occur on the cathode side of polymer electrolyte fuel cells, *viz*. ORR and catalyst dissolution, we expect this effective proton concentration to serve as a meaningful LRE descriptor. This composite interface descriptor establishes the missing linkage between LRE effects, as obtained from microscopic theories and simulations, and device level metrics related to performance, lifetime, and economic viability. I will systematically evaluate how structural, compositional and operational parameters affect the newly proposed descriptor. I then propose a second LRE descriptor that accounts for the impact of the local electrostatic potential, and analyze how two key kinetic parameters, namely the reaction order w.r.t. the proton concentration, γ_{H^+}, and the electronic transfer coefficient, α, govern the relationship between LRE descriptors and catalytic activity.

The structure of the article is as follows. I first define our model system, present the theoretical framework, and introduce the LRE descriptor. This is followed by a parametric analysis exploring the key structural and compositional properties and operating conditions. Furthermore, I extend the analysis to establish how relevant LRE effects can be combined into an activity descriptor that properly reproduces and eventually allows predicting trends of reaction rates. Finally, I conclude with a summary of the main findings and their implications for the optimization of supported electrocatalysts.

6.2. Definition of effective proton concentration

In planar catalytic surfaces, the reactant concentration at the RP is spatially homogeneous. In such systems, the rate of proton-coupled electrochemical reactions correlates positively with the local proton concentration at the RP. Higher proton concentrations increase the probability of proton consumption, and thus enhance the reaction rate.

However, in supported NP systems, the situation becomes more complex. Firstly, the spatial distribution of the electrolyte is no longer uniform at the RP due to nanoscale curvature, heterogeneous surface structures, and catalyst–support interactions. Secondly, NP surfaces feature a range of crystallographic features, including terraces, edges, and corners, each exhibiting distinct catalytic activities. While these atomistic features are critical, identifying the most catalytically active sites or regions remains challenging and is typically beyond the resolution of mean-field models.

Therefore, to characterize the LRE in a physically meaningful and computationally accessible way, we introduce a descriptor: the average proton concentration over the entire NP's RP. This quantity provides a first-order approximation of proton availability at the interface and enables comparison across different NP sizes, NP coverages, support types, and electrochemical conditions.

For proton-consuming reactions, such as hydrogen evolution, oxygen and CO_2 reduction, this effective proton concentration is expected to be directly related to catalytic activity. It captures in highly condensed form the interplay between NP morphology, relative magnitude of Fermi levels of NP and support materials, and ion distributions, making it a valuable descriptor for understanding and predicting structure–reactivity relationships in electrocatalytic NP systems.

Figure 37(a) shows the system of interest in a cylindrical coordinate (r, z, φ). Owing to the axial symmetry of the supported NP system, *i.e.*, no variation with respect to the azimuthal angle φ, the three-dimensional problem reduces to a two-dimensional one in the (r, z) plane. Here, the RP is assumed to be located at the same position as the outer Helmholtz plane (OHP), which represents the closest approach of solvated ions. The OHP is positioned at a distance, L_{RP}, from the electrode surface, as indicated by the red dashed arc $\widehat{\mathrm{RP}}$ in Figure 37(a). Plots in the following will show not only the two-dimensional (2D) distribution of proton concentration but also the concentration profile along the red dashed arc.

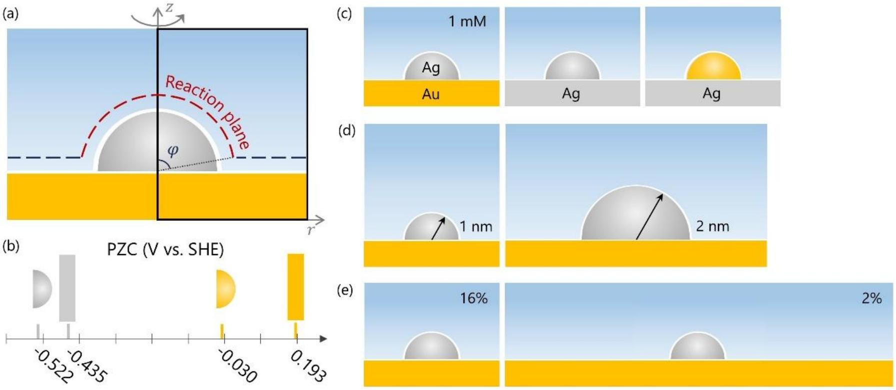

Figure 37. (a) Schematic representation of the supported NP system and the 2D modeling domain. (b) PZC of Ag NP, Ag support, Au NP and Au support [37,163,164]. (c-e) Tunable system parameters: (c) material combination, (d) NP size, and (e) NCSF on support.

The effective proton concentration, $\overline{c_{\mathrm{H}^+}^{\mathrm{RP}}}$, is defined as the average c_{H^+} over the hemispherical RP around the NP , which can be calculated by a line integral of c_{H^+} along the arc $\widehat{\mathrm{RP}}$, weighted by $2\pi r$ and divided by the area, S_{RP}, of the RP.

$$\overline{c_{\mathrm{H}^+}^{\mathrm{RP}}} = \frac{\iint_{\mathrm{RP}} c_{\mathrm{H}^+}(r, z, \varphi)\mathrm{d}S}{S_{\mathrm{RP}}}, \tag{78}$$

$$S_{\mathrm{RP}} = 2\pi(R_{\mathrm{cat}} + L_{\mathrm{RP}})^2(1 - cos\,\varphi). \tag{79}$$

Since c_{H^+} is rotationally symmetric about the vertical axis, the surface integral can be reduced to a one-dimensional line integral along the arc $\widehat{\mathrm{RP}}$, parametrized by arc length s. Accordingly, Eqn. (78) is rewritten as,

$$\overline{c_{\mathrm{H}^+}^{\mathrm{RP}}} = \frac{\int_{\widehat{\mathrm{RP}}} c_{\mathrm{H}^+}(r(s), z(s)) 2\pi r \mathrm{d}s}{S_{\mathrm{RP}}}, \tag{80}$$

With $\mathrm{d}s$ the infinitesimal arc length element of $\widehat{\mathrm{RP}}$ and $\varphi = \frac{\pi}{2} - \arcsin\frac{L_{\mathrm{RP}}}{R_{\mathrm{cat}}+L_{\mathrm{RP}}}$. Figure 37(b) visualizes the PZCs of Au support, Ag support, Au NP and Ag NP. The PZC of Au support is 715 mV more positive than that of Ag NP. Additionally, the PZC of the NP is more negative than that of the corresponding planar surface, due to the nanoscale surface curvature [208].

Table 7. Base case parameters and their variations.

	Parameters	**Base case**	**Variations**				
1	Materials combination	Ag @ Au	Ag @ Ag			Au @ Ag	
2	NP radius	1 nm	2 nm				
3	NP-covered support surface fraction	16%	2%				
4	Bulk ion concentration	100 mM	1 mM				
5	Electrode potential (V_{SHE})	-0.522	-0.4	-0.3	-0.2	-0.09	0.193

Figure 37 (c) to (e) illustrate the key parameters available for adjustment in this study: support material, NP radius, and NCSF on the support, summarized in Table 7. Additionally, the influence of bulk electrolyte concentration on the system behavior is examined. For the baseline case, a 1 nm Ag NP deposited on an planar Au surface immersed in a 100 mM $HClO_4$ electrolyte solution, with protons as the only cation species. The simulation cell has a radius of 2.5 nm, implying a NCSF of 16%.

6.3. Parametric studies

6.3.1. Effect of the support materials

In an effort to elucidate the influence of support properties on the LRE, I compare Ag NP supported on Au and Ag surfaces, focusing on their effect on the effective proton concentration, $\overline{c_{\mathrm{H^+}}^{\mathrm{RP}}}$. Figure 38 (a) and (c) show 2D proton concentration distributions around the catalyst NP, while Figure 38 (b) and (d) display 1D concentration profiles along $\widehat{\mathrm{RP}}$. The values of calculated $\overline{c_{\mathrm{H^+}}^{\mathrm{RP}}}$ of a specific system are indicated by the diamond marks on the corresponding curves in Figure 38 (b) and (d).

As a reference, the base case of an Ag nanoparticle supported on an Au surface is considered first. Since Au support has a more positive PZC ($0.193\ \mathrm{V_{SHE}}$) than Ag NP ($-0.522\ \mathrm{V_{SHE}}$), at a given electrode potential, specifically, at the PZC of the Ag NP, the Au surface is strongly negatively charged. This creates a negative potential region above the support surface, leading to proton accumulation. The close distance between NP and support allows the EDL structure around the NP to be strongly affected by the negative charges on the support surface, caused by the double-layer overlap effect. This effect is most pronounced in the vicinity of the NP–support interface, where the overlap of the respective EDL is the strongest. This is evidenced by the rising blue curve within the arc length range of 0 to 2 nm in Figure 38 (b) and (d).

Next, it is investigated how the proton concentration profile is altered when the support material changes from Au to Ag. Given that the PZC of planar Ag support is $-0.435\ \mathrm{V_{SHE}}$, the mismatch in PZC is smaller for the Ag NP–Ag support system than for the Ag NP–Au support system. As reflected by the lower grey curve compared to the blue curve in Figure 38 (b) and (d), a lower proton concentration surrounding the NP is observed when it is supported on the Ag surface compared to the case on the Au surface. To summarize, the double-layer overlap effect is especially prominent when there is a significant difference in PZC between NP and support.

The impact of electrolyte concentration on the double-layer overlap effect is studied by varying the electrolyte concentration from 100 mM to 1 mM. At 100 mM, the $\overline{c_{\mathrm{H^+}}^{\mathrm{RP}}}$ of NPs supported on an Au surface is twice as large as that on an Ag surface, as shown by the diamond marks in Figure 38 (b) and (d). In contrast, at 1 mM, the difference increases markedly, from a 2-fold to a more than 5-fold variation. This suggests that the double-layer overlap effect becomes more pronounced at lower electrolyte concentrations, as implied by the larger Debye length.

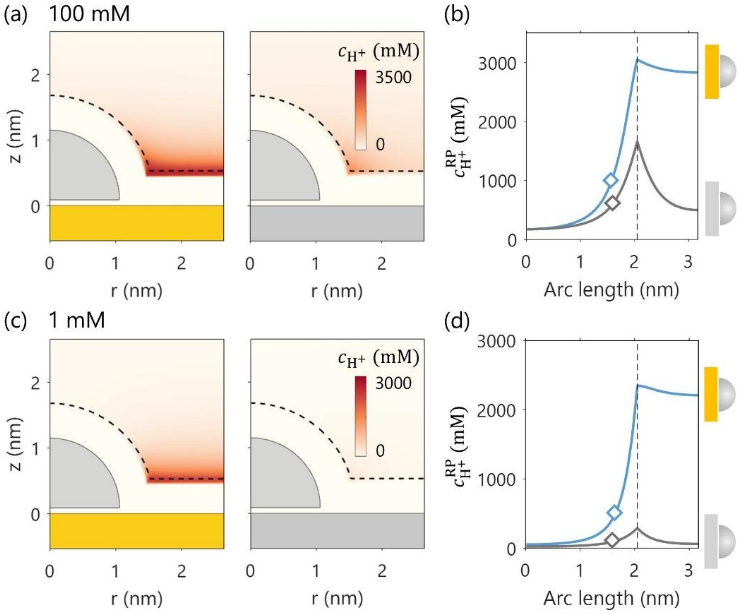

Figure 38. Effect of support material (Au vs. Ag) on proton concentration distribution,

c_{H^+}. Panels (a) and (c) show the 2D distribution of c_{H^+} for bulk concentrations of 100 mM and 1 mM, respectively. Panels (b) and (d) display the corresponding 1D profiles of c_{H^+} along the RP. The diamond marks in (b) and (d) denote the calculated $\overline{c_{\mathrm{H}^+}^{\mathrm{RP}}}$. The vertical lines mark the boundary of the RP. The electrode potential is set to be the PZC of the hemispherical Ag NP, $E = -0.522\ \mathrm{V_{SHE}}$.The PZC of planar Ag and Au support are $-0.435\ \mathrm{V_{SHE}}$ and $0.193\ \mathrm{V_{SHE}}$, respectively.

6.3.2. Effect of NP size

Next, the influence of NP size on the proposed descriptor is analyzed by comparing NPs with radii of 1 nm and 2 nm, while maintaining the NCSF at 16%. It is well established that the work function and PZC of larger NPs are more positive than those of smaller NPs due to surface curvature effect [209]. Indeed, simulations performed as part of this Ph.D. research show that an unsupported Ag NP with a 2 nm radius has a more positive PZC ($-0.478\ \mathrm{V_{SHE}}$) compared to a 1 nm NP ($-0.522\ \mathrm{V_{SHE}}$). As a result, at a given electrode potential, the larger NP would carry a more negative surface charge, leading to greater proton accumulation around it. However, this trend is reversed when the Ag NP is anchored on an Au support. As indicated by the diamond markers in Figure 39 (b) and (d), the average proton concentration is actually lower for the larger supported NP. This reversal is attributed to the double-layer overlap effect, which is most prominent near the NP–support interface. For the larger NP, a significant portion of its surface lies farther from the support, reducing the influence of the support's double layer on the local proton concentration at the RP. Consequently, the average proton concentration at the RP of the larger NP is lower than that of the smaller NP. This trend is observed under both electrolyte concentrations examined.

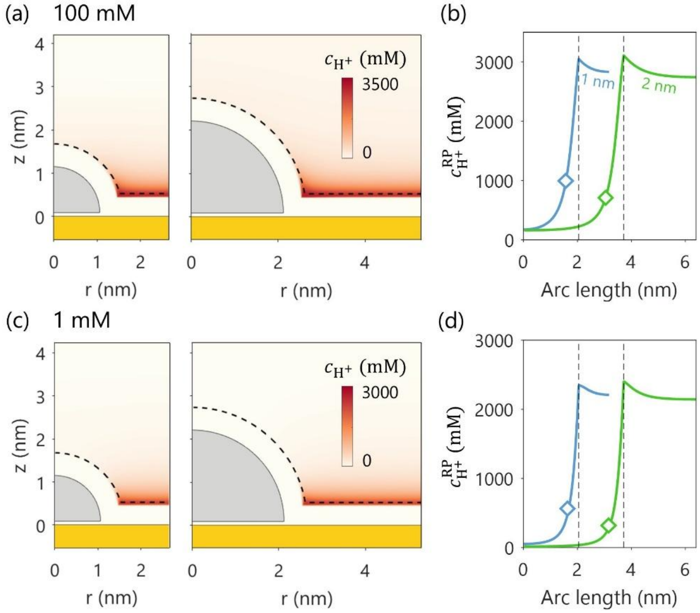

Figure 39. Effect of NP radius (1 nm vs. 2 nm) on proton concentration distribution, $c_{\mathrm{H^+}}$. Panels (a) and (c) show the 2D distribution of $c_{\mathrm{H^+}}$ for bulk concentrations of 100 mM and 1 mM, respectively. Panels (b) and (d) display the corresponding 1D profiles of $c_{\mathrm{H^+}}$ along the reaction plane. The diamond marks in (b) and (d) denote the calculated $\overline{c_{\mathrm{H^+}}^{\mathrm{RP}}}$. The vertical lines mark the boundary of the RP. The electrode potential is set to be the PZC of the hemispherical Ag NP of 1nm radius, $E = -0.522\ \mathrm{V_{SHE}}$. The PZC of the 2 nm Ag NP and the planar Au support are $-0.478\ \mathrm{V_{SHE}}$ and $0.193\ \mathrm{V_{SHE}}$, respectively.

6.3.3. Effect of NCSF

Maintaining a fixed NP size while reducing the NCSF on the support leads to an increase in interparticle distance Previous studies have shown that NP proximity significantly influences the catalytic activity of carbon-supported Pt NPs for the ORR [58]. At $0.9\ \mathrm{V_{RHE}}$, Pt NPs are negatively charged and thus protophilic, while the positively charged carbon support is protophobic. The overlap of their respective EDLs depletes the proton concentration near the Pt NPs. However, when the interparticle distance is reduced, the overlapping EDL is increasingly governed by the charging properties of neighboring Pt NPs, which amplifies the protophilic behavior and eventually dominates over the protophobic effect of the support. The study in Ref. [58] concluded that the NCSF or interparticle distance plays a crucial role in determining the accumulation and depletion of protons.

In this chapter, the effect of NCSF and particle proximity was revisit. By increasing the simulation cell size, the NCSF was reduced from 16% to 2%, which increases the interparticle distance from 3 nm to 13 nm. As the Ag NP has a more negative PZC than a pcAu support, it bears more positive charges, and thus more protophobic. It was therefore expected that larger NCSF will repel protons more strongly, resulting lower proton concentration at the RP. However, the nearly identical c_{H^+} profiles along the RP in Figure 40 (b) show that the coverage has a negligible effect on proton distribution. This counterintuitive result might be explained for the case of 100 mM bulk concentration, where the Debye length of 1 nm is smaller than both interparticle distances (3 nm and 13 nm), effectively screening electrostatic interactions between neighboring NPs.

Surprisingly, even at a dilute solution of 1 mM concentration, where the Debye length is roughly 10 nm, there is still no discernable difference in $\overline{c_{\mathrm{H}^+}}$ between the two coverage cases, as shown in Figure 40 (c) and (d). This observation highlights an important point: whether interparticle “communication” occurs of not is not governed by the bulk ion concentration or its associated Debye length, but rather by the local ion concentration in the space between neighboring NPs. This local ion concentration is governed by the surface charge density of the support. A more relevant length scale in this context is the so-called Gouy–Chapman length, defined as $l_{\mathrm{GC}} = \frac{2\epsilon k_{\mathrm{B}}T}{e|\sigma|}$, where ϵ is the permittivity of the dielectric medium, σ is the surface charge density, k_{B} is the Boltzmann constant, T is the temperature, and e is the elementary charge. The Gouy-Chapman length is inversely proportional to the surface charge density σ [210].

At an applied potential of $-0.522\ \mathrm{V_{SHE}}$, which is much more negative than the PZC of the Au support ($0.193\ \mathrm{V_{SHE}}$), σ reaches $10\ \mathrm{\mu C/cm^2}$. This corresponds to a Gouy–Chapman length of 0.36 nm in aqueous solution, much smaller than the interparticle distances in both coverage cases (3 nm and 13 nm). As a result, the NPs are electrostatically isolated by the highly concentrated region near the support, explaining the negligible variation in $\overline{c_{\mathrm{H}^+}^{\mathrm{RP}}}$ with NP proximity.

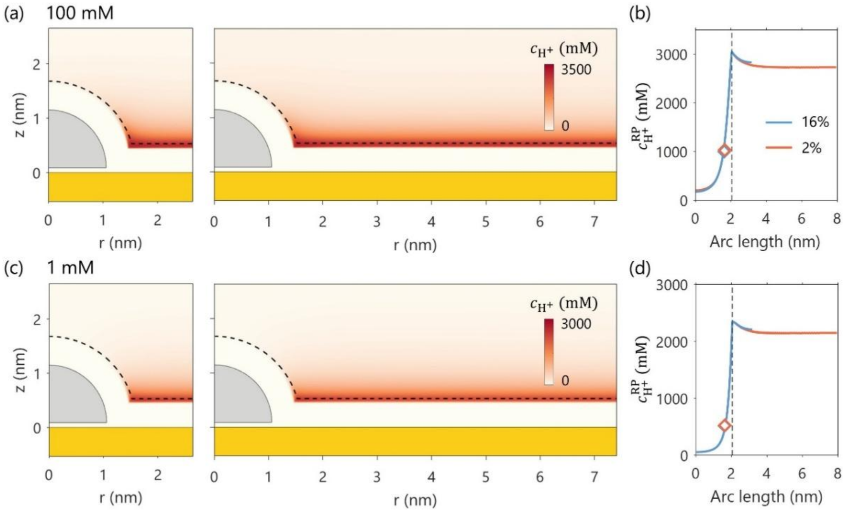

Figure 40. Effect of NCSF (16% vs. 2%) on proton concentration distribution, $c_{\mathrm{H^+}}$. Panels (a) and (c) show the 2D distribution of $c_{\mathrm{H^+}}$ for bulk concentrations of 100 mM and 1 mM, respectively. Panels (b) and (d) display the corresponding 1D profiles of $c_{\mathrm{H^+}}$ along the reaction plane. The diamond symbols in (b) and (d) denote the calculated $\overline{c_{\mathrm{H^+}}^{\mathrm{RP}}}$. The vertical lines mark the end of the RP. The electrode potential is set to be the PZC of the hemispherical Ag NP, $E = -0.522\ \mathrm{V_{SHE}}$. The PZC of planar Au support is $0.193\ \mathrm{V_{SHE}}$.

The strong cation accumulation near the support surface is caused by the electrode potential being significantly more negative than the PZC of the support material. This ion accumulation can be reduced by tuning the electrode potential toward more positive values. A question then arises naturally: will the proximity effect emerge if fewer ions are present in the space between neighboring NPs?

Figure 41 presents the 2D distribution and 1D profile of proton concentration for a series of increasingly positive E. Figure 42 plots $\overline{c_{\mathrm{H^+}}^{\mathrm{RP}}}$ as a function of E, shown in both linear and logarithm scales. At strongly negative potentials, such as $-0.522\ \mathrm{V_{SHE}}$ and $-0.4\ \mathrm{V_{SHE}}$, no significant difference in $\overline{c_{\mathrm{H^+}}^{\mathrm{RP}}}$ is observed between the two NP coverage conditions. However, as E becomes more positive, at $-0.3\ \mathrm{V_{SHE}}$ and $-0.2\ \mathrm{V_{SHE}}$, a modest difference in $\overline{c_{\mathrm{H^+}}^{\mathrm{RP}}}$ of approximately 10 mM appears. At even more positive potentials, such as $-0.093\ \mathrm{V_{SHE}}$ and $0.193\ \mathrm{V_{SHE}}$, this difference vanishes again, as protons are strongly repelled from the NP surfaces under these conditions.

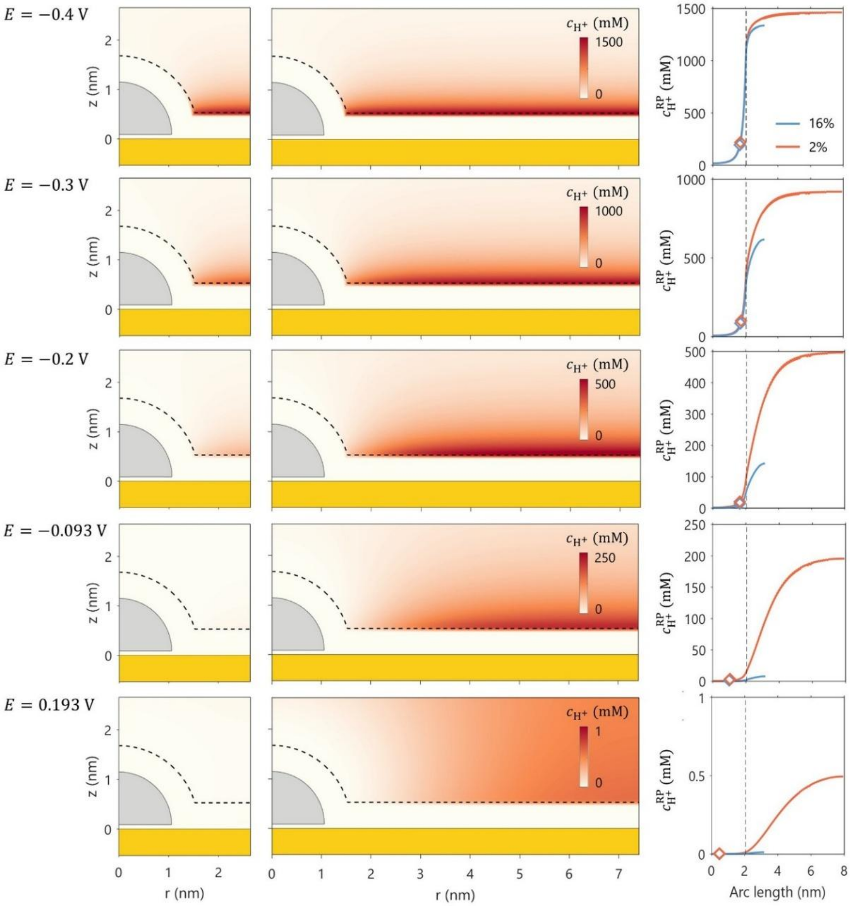

Figure 41. 2D distribution of c_{H^+} for bulk concentrations of 1 mM and the corresponding 1D profiles of c_{H^+} profiles along the reaction plane for a series of electrode potentials as specified in the figure. The diamond symbols in the line graph denote the calculated $\overline{c_{\mathrm{H}^+}^{\mathrm{RP}}}$. The vertical lines mark the end of the RP.

Figure 41 and Figure 42 reveal that, even though the ion accumulation near the support surface is alleviated as E approaches the PZC of the support, protons are nonetheless repelled from the NP surface at very positive electrode potentials, and no significant particle proximity effect is observed. One would naturally ask: since anions will not be repelled from the NP, could their concentration be influenced by variations in NP proximity? The answer is affirmative, as demonstrated in Figure 43. While the proximity effect remains small in the 100 mM solution, it becomes noticeably more pronounced in the 1 mM case.

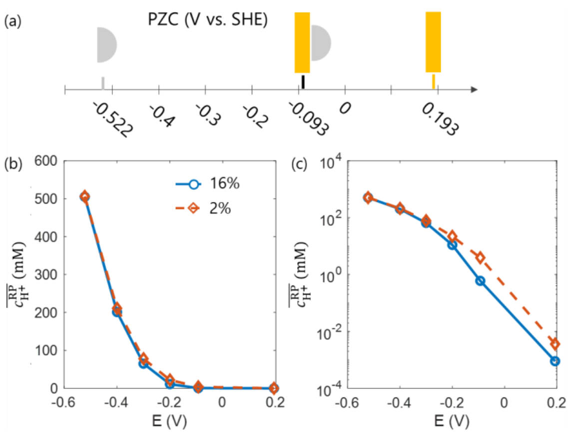

Figure 42. (a) A series of electrode potentials applied to the Au supported Ag NP system. (b) and (c) show $\overline{c_{\mathrm{H^+}}^{\mathrm{RP}}}$ as a function of electrode potentials in linear and logarithmic scales.

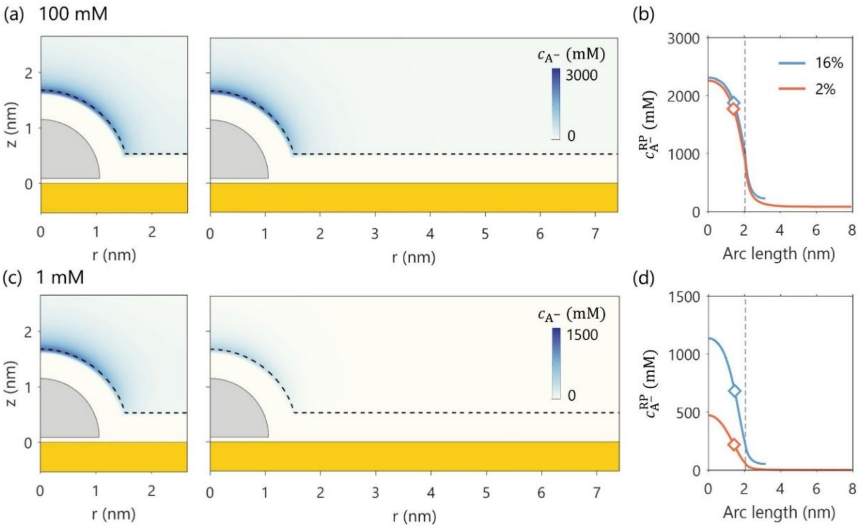

Figure 43. Effect of NCSF (16% vs. 2%) on anion concentration distribution, $c_{\mathrm{A^-}}$, for Ag NP supported on Au substrate. Panels (a) and (c) show the 2D distribution of $c_{\mathrm{A^-}}$ for bulk concentrations of 100 mM and 1 mM, respectively. Panels (b) and (d) display the corresponding 1D profiles of $c_{\mathrm{A^-}}$ along the reaction plane. The diamond symbols in (b) and (d) denote the calculated $\overline{c_{\mathrm{A^-}}^{\mathrm{RP}}}$. The vertical lines mark the end of the RP. $E = 0.193\ \mathrm{V_{SHE}}$. The electrode potential is set to be the PZC of planar Au support, $E = -0.193\ \mathrm{V_{SHE}}$. The PZC of hemispherical Ag NP is $-0.435\ \mathrm{V_{SHE}}$.

Above presented results and discussions can be subsumed into three main conditions that must be met for a pronounced NCSF (proximity) effect to emerge: (i) low bulk concentration in the solution, (ii) the electrode potential close to the PZC of the support material, and (iii) a specific sequence of the PZC of the catalyst NP and the support such that the ions of interests are more attracted to the NP than to the support. For proton-consuming reactions, this implies that the PZC of the catalyst should be more positive than that of the support. To test this hypothesis, the materials of NP and support are reversed, *viz.*, a Au NP supported on a Ag surface, as illustrated in Figure 44. With the electrode potential set to be the PZC of Ag support $(-0.435\ \mathrm{V_{SHE}})$, the 1 mM solution shows a clear proximity effect in proton concentration, validating our hypothesis.

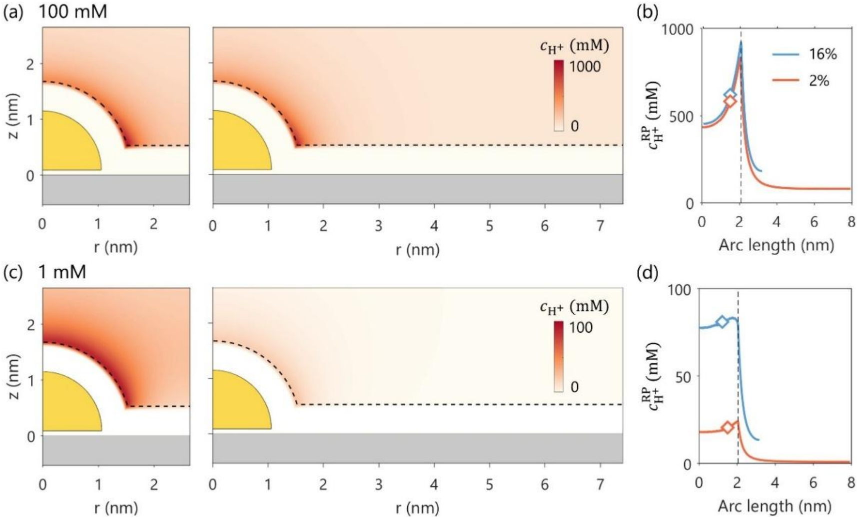

Figure 44. Effect of NCSF (16% vs. 2%) on proton concentration distribution, $c_{\mathrm{H^+}}$, for Au NP supported on Ag substrate. Panels (a) and (c) show the 2D distribution of $c_{\mathrm{H^+}}$ for bulk concentrations of 100 mM and 1 mM, respectively. Panels (b) and (d) display the corresponding 1D profiles of $c_{\mathrm{H^+}}$ along the reaction plane. The diamond symbols in (b) and (d) denote the calculated $\overline{c_{\mathrm{H^+}}^{\mathrm{RP}}}$. The vertical lines mark the end of the RP. $E = -0.435\ \mathrm{V_{SHE}}$. The PZC for Au NP and Ag support are $-0.03\ \mathrm{V_{SHE}}$ and $-0.435\ \mathrm{V_{SHE}}$, respectively.

6.4. Reaction rate descriptor

In the preceding section, it has been analyzed how support material, NP size, NCSF and electrode potential affect the LRE by monitoring the proposed LRE descriptor, namely the average proton concentration over the RP. The specific value of the LRE descriptor lies in its independence of parameters that are specific to reactions. In an attempt to further elucidate its impact on reaction rates, a simple Butler–Volmer-type kinetic model is built. The surface-area-specific activity is expressed as the averaged kinetic current density over the area of the reaction plane enveloping the particle,

$$\bar{j} = \frac{\int_{\overset{\frown}{\mathrm{RP}}} j(r,z) 2\pi r ds}{S_{\mathrm{RP}}}, \tag{81}$$

where the spatially varying current density is given by the Butler–Volmer equation accounting for the Frumkin effect,

$$j(r,z) = j^0 \left(\frac{c_{\mathrm{H}^+}^{\mathrm{RP}}(r,z)}{c_{\mathrm{H}^+}^{\mathrm{b}}} \right)^{\gamma_{\mathrm{H}^+}} \exp\left(-\frac{\alpha e (E - \Delta\phi_{\mathrm{RP}}(r,z) - E^{\mathrm{eq}})}{k_{\mathrm{B}} T} \right), \tag{82}$$

with j^0 being the exchange current density, γ_{H}^{+} the reaction order of protons, $c_{\mathrm{H}^+}^{\mathrm{RP}}$ and $c_{\mathrm{H}^+}^{\mathrm{b}}$ the proton concentrations at the RP and in the bulk solution, α the transfer coefficient, $\Delta\phi_{\mathrm{RP}}$ deviation of the electrostatic potential at the RP from the solution bulk, and E^{eq} the equilibrium potential. Note in passing that j^0, $c_{\mathrm{H}^+}^{\mathrm{b}}$ and E^{eq} are interrelated: $c_{\mathrm{H}^+}^{\mathrm{b}}$ corresponds to the bulk concentration at which j^0 is measured, and E^{eq} refers to the equilibrium potential at a solution of that same bulk concentration.

Separating location-dependent and independent terms in Equation (82) yields,

$$j = j^0 {c_{\mathrm{H}^+}^{\mathrm{b}}}^{-\gamma_{\mathrm{H}^+}} \exp\left(-\frac{\alpha e (E - E^{\mathrm{eq}})}{k_{\mathrm{B}} T} \right) \left(c_{\mathrm{H}^+}^{\mathrm{RP}}(r,z) \right)^{\gamma_{\mathrm{H}^+}} \exp\left(\frac{e \Delta\phi_{\mathrm{RP}}(r,z)}{k_{\mathrm{B}} T} \right)^{\alpha}. \tag{83}$$

The first three factors on the right-hand side of Equation (83) are spatially invariant, while the last two factors incorporate the LRE effects. In addition to $c_{\mathrm{H}^+}^{\mathrm{RP}}$, $\Delta\phi_{\mathrm{RP}}$ also modulates the reaction rate through the exponential term of driving force, indicating that an LRE descriptor that is solely based on proton concentration cannot fully capture the LRE effects. To complement it, we denote the exponential factor by the symbol Λ,

$$\Lambda(r,z) = \exp\left(\frac{e \Delta\phi(r,z)}{k_{\mathrm{B}} T} \right), \tag{84}$$

and introduce its area-averaged value over the RP as a complementary LRE descriptor, providing a mean-field-type measure of the spatial variations in the electrostatic potential,

$$\overline{\Lambda_{\mathrm{RP}}} = \frac{\int_{\widehat{\mathrm{RP}}} \Lambda_{\mathrm{RP}} 2\pi r \mathrm{d}s}{S_{\mathrm{RP}}} = \frac{\int_{\widehat{\mathrm{RP}}} \exp\left(\frac{e\Delta\phi_{\mathrm{RP}}(r,z)}{k_{\mathrm{B}}T}\right) 2\pi r \mathrm{d}s}{S_{\mathrm{RP}}}. \tag{85}$$

Note that $\overline{\Lambda_{\mathrm{RP}}}$ is likewise reaction-agnostic; as an LRE descriptor, it reflects only the properties of the LRE and not the kinetic specifics of any reaction.

The surface-area-specific activity , viz., the area-averaged kinetic current density, can be rewritten by substituting Equations (83) and (84) into Equation (81),

$$\bar{j} = j^0 {c_{\mathrm{H}^+}^{\mathrm{b}}}^{-\gamma_{\mathrm{H}^+}} \exp\left(-\frac{\alpha e(E - E^{\mathrm{eq}})}{k_{\mathrm{B}}T}\right) \frac{\int_{\widehat{\mathrm{RP}}} \left(c_{\mathrm{H}^+}^{\mathrm{RP}}(r,z)\right)^{\gamma_{\mathrm{H}^+}} \left(\Lambda_{\mathrm{RP}}(r,z)\right)^{\alpha} 2\pi r \mathrm{d}s}{S_{\mathrm{RP}}}. \tag{86}$$

Making use of the two defined LRE descriptors, an approximate expression of the kinetic current density can be written by replacing the spatially-varying $c_{\mathrm{H}^+}^{\mathrm{RP}}(r,z)$ and $\Lambda_{\mathrm{RP}}(r,z)$ in Equation (86) with their average values, $\overline{c_{\mathrm{H}^+}^{\mathrm{RP}}}$ and $\overline{\Lambda_{\mathrm{RP}}}$,

$$\overline{j_{\mathrm{ap}}} = j^0 {c_{\mathrm{H}^+}^{\mathrm{b}}}^{-\gamma_{\mathrm{H}^+}} \exp\left(-\frac{\alpha e(E - E^{\mathrm{eq}})}{k_{\mathrm{B}}T}\right) \frac{\int_{\widehat{\mathrm{RP}}} \left(\overline{c_{\mathrm{H}^+}^{\mathrm{RP}}}\right)^{\gamma_{\mathrm{H}^+}} \left(\overline{\Lambda_{\mathrm{RP}}}\right)^{\alpha} 2\pi r \mathrm{d}s}{S_{\mathrm{RP}}}, \tag{87}$$

$$\overline{j_{\mathrm{ap}}} = j^0 {c_{\mathrm{H}^+}^{\mathrm{b}}}^{-\gamma_{\mathrm{H}^+}} \exp\left(-\frac{\alpha e(E - E^{\mathrm{eq}})}{k_{\mathrm{B}}T}\right) \left(\overline{c_{\mathrm{H}^+}^{\mathrm{RP}}}\right)^{\gamma_{\mathrm{H}^+}} \left(\overline{\Lambda_{\mathrm{RP}}}\right)^{\alpha}.$$

(87)Although Equation (87) is not strictly equivalent to Equation (86) (since the product of averages is not equal to the average of the product), it turns out to be a reasonable approximation for many cases (for a detailed discussion, vide infra). The practical value of Equation (87) is that it enables the definition of an activity descriptor of the form $\left(\overline{c_{\mathrm{H}^+}^{\mathrm{RP}}}\right)^{\gamma_{\mathrm{H}^+}} \left(\overline{\Lambda_{\mathrm{RP}}}\right)^{\alpha}$ that is a combination of two reaction-agnostic LRE descriptors, $\overline{c_{\mathrm{H}^+}^{\mathrm{RP}}}$ and $\overline{\Lambda_{\mathrm{RP}}}$, with the specifics of a particular reaction entered through the kinetic parameters γ_{H^+} and α.

We expect this representation to be of practical utility since it allows the impact of the catalyst–support combination and nanoscale configuration to be accounted for explicitly through the LRE descriptors. They can therefore be tabulated or computed in advance (as a first step) for a given supported NP system. In a separate step, researchers interested in a particular reaction can combine these two values with reaction-specific parameters $\gamma_{\mathrm{H^+}}$ and α to evaluate $\left(\overline{c_{\mathrm{H^+}}^{\mathrm{RP}}}\right)^{\gamma_{\mathrm{H^+}}}\left(\overline{\Lambda_{\mathrm{RP}}}\right)^{\alpha}$ to predict activity trends.

Of course, for each specific reaction one could alternatively use the average Frumkin factor, $\frac{\int_{\widehat{\mathrm{RP}}}\exp\left(\frac{-\left(\gamma_{\mathrm{H^+}}-\alpha\right)e\Delta\phi_{\mathrm{RP}}}{k_{\mathrm{B}}T}\right)2\pi r\mathrm{d}s}{S_{\mathrm{RP}}}$, derived by approximating $c_{\mathrm{H^+}}^{\mathrm{RP}}$ in Equation (86) with Boltzmann distribution, as an activity descriptor. However, this requires recalculating the full spatial distributions of $c_{\mathrm{H^+}}^{\mathrm{RP}}(r,z)$and $\Lambda_{\mathrm{RP}}(r,z)$. In contrast, our proposed recipe $\left(\overline{c_{\mathrm{H^+}}^{\mathrm{RP}}}\right)^{\gamma_{\mathrm{H^+}}}\left(\overline{\Lambda_{\mathrm{RP}}}\right)^{\alpha}$ provides a more efficient and transferable means of screening material combinations and configurations for reactions of interest, without the need for solving the spatial averages again.

I now proceed to illustrate the formal step-wise analysis, proposed above, with an example. Since the exchange current density of HER on Ag is two orders of magnitude lower than that of Au [27,211,212], we study Au NP supported on Ag surface and neglect the HER contribution from the Ag support. Figure 45 (a) and (b) show the 2D distributions of Λ as well as the Λ_{RP} along the RP for NCSF of 16%, 10%, 6% and 2%. Since the Au NP is more negatively charged than the Ag support, closer interparticle distance gives more negative ϕ_{RP}, resulting in lower Λ_{RP}.

Using Equation (86), we calculate the surface-area specific activity for these NCSF, examining two representative parameter sets: (i) $\gamma_{\mathrm{H^+}}=1$ and $\alpha=0.5$ (a reasonable combination) and (ii) $\gamma_{\mathrm{H^+}}=\alpha=0.5$ (a less common but physically possible combination). To probe the quantitative relationship between LRE effects and reaction rate, the normalized quantities $\overline{c_{\mathrm{H^+}}^{\mathrm{RP}}}$, $\overline{\Lambda_{\mathrm{RP}}}$ and $\bar{j}$ are plotted versus NCSF in Figure 45 (c). Normalization was achieved by dividing each series by its minimal value, i.e., $\bar{j}\,/\min(\bar{j}\,)$, $\overline{c_{\mathrm{H^+}}^{\mathrm{RP}}}/\min\left(\overline{c_{\mathrm{H^+}}^{\mathrm{RP}}}\right)$, and $\overline{\Lambda_{\mathrm{RP}}}/\min\left(\overline{\Lambda_{\mathrm{RP}}}\right)$.

For the case of $\gamma_{\mathrm{H}^+} = 1$ and $\alpha = 0.5$, both $\bar{j}$ and $\overline{c_{\mathrm{H}^+}}$ increase with NCSF, whereas $\overline{\Lambda_{\mathrm{RP}}}$ decreases, see Figure 45 (c). Recalling Equation (87), when the two descriptors are combined as $\left(\overline{c_{\mathrm{H}^+}^{\mathrm{RP}}}\right)^{\gamma_{\mathrm{H}^+}}\left(\overline{\Lambda_{\mathrm{RP}}}\right)^{\alpha}$, the resulting trend aligns closely with that of $\bar{j}$, showing an approximately linear correlation, see Figure 45 (d). Indeed, the approximation (Equation (87)) reproduces the fully resolved current density (Equation (86)) with good agreement, as shown in Figure 45 (e).

The discrepancy between $\bar{j}$ and $\overline{j_{\mathrm{ap}}}$ could be larger when the spatial variations of the electrostatic potential and proton concentration over the RP are larger, which in turn are primarily controlled by the PZC difference between the NP and the support. In our Ag-supported Au NP system, this PZC difference is already substantial ($\approx 0.4\ \mathrm{V}$), and most practical catalyst–support combinations are expected to exhibits differences in PZC of similar or smaller magnitude [157,213]. Thus, the approximation appears justified in more general terms. It is worth noting that Au-supported Ag NP system (Figure 40(d)) exhibits larger variations in proton concentration over the RP than Ag supported Au NP system (Figure 44(d)). Therefore, the activity descriptor should be more suitable for the former case than the latter one.

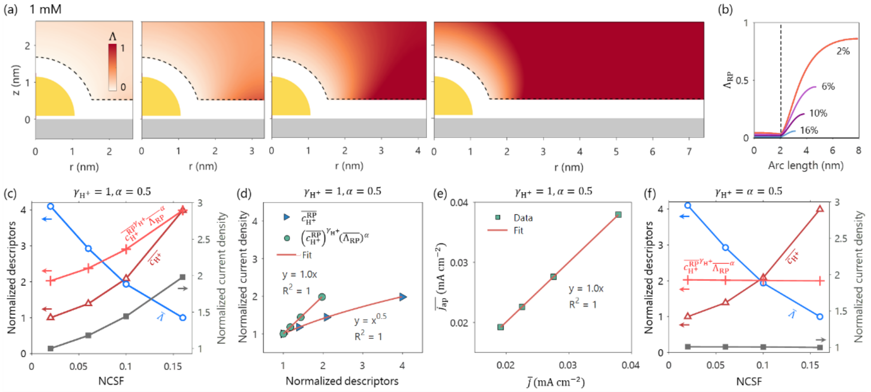

Figure 45. (a) 2D distribution of Λ for NCSF of 16%, 10%, 6% and 2%. The bulk proton concentration is 1 mM. (b) Corresponding 1D profiles of Λ_{RP} along the reaction plane. The PZC for Au NP and Ag support are $-0.03\ \mathrm{V_{SHE}}$ and $-0.435\ \mathrm{V_{SHE}}$, respectively. $E = -0.435\ \mathrm{V_{SHE}}$. (c)-(f) Quantitative relationships between the LRE descriptors and reaction rate of the hydrogen evolution reaction. Panel (c) and (f) show the normalized descriptors and

current densities as functions of NCSF for the case of $\gamma_{\mathrm{H}^+} = 1$, $\alpha = 0.5$, and $\gamma_{\mathrm{H}^+} = \alpha = 0.5$, respectively. (d) Correlation between the normalized descriptors and normalized current density. (e) Correlation between the averaged current density $\bar{j}$ and its approximation $\overline{j_{\mathrm{ap}}}$. The exchange current density is taken as $10^{-3.5}\ \mathrm{mA\ cm^{-2}}$ in 100 mM HCl solution, and $\alpha = 0.5$ [27].

For the case $\gamma_{\mathrm{H}^+} = \alpha = 0.5$ (Figure 45(f)), $\bar{j}$ remains nearly constant with NCSF and neither $\overline{c_{\mathrm{H}^+}^{\mathrm{RP}}}$ nor $\overline{\Lambda_{\mathrm{RP}}}$ alone captures this behavior; only their combined form $\left(\overline{c_{\mathrm{H}^+}^{\mathrm{RP}}}\right)^{\gamma_{\mathrm{H}^+}} \left(\overline{\Lambda_{\mathrm{RP}}}\right)^{\alpha}$ reproduces the correct trend. The underlying reason is, to a first approximation, $c_{\mathrm{H}^+}^{\mathrm{RP}}$ follows a Boltzmann distribution, *i.e.*, $c_{\mathrm{H}^+}^{\mathrm{RP}} \propto \exp(-e\Delta\phi_{\mathrm{RP}}/k_{\mathrm{B}}T)$; thus, when $\gamma_{\mathrm{H}^+} = \alpha$ the potential dependence cancels exactly in the exponential term.

It is worth noting that the effective proton concentration, while not directly measurable experimentally, serves as a computational descriptor of the LRE. Similar to widely used descriptors in catalysis, such as the d-band center [214], this quantity provides a measure that connects computed properties to observable electrochemical behavior. By averaging over the RP, it captures the heterogeneity of the double layer around supported NPs and allows for systematic comparison across different materials, particle sizes, and electrode configurations. Therefore, even though it is model-specific, the effective proton concentration offers a practical and physically meaningful metric for understanding and rationally designing NP-based electrocatalysts.

6.5. Summary

This chapter introduced a modeling approach to investigate the local reaction environment around supported electrocatalyst NPs. The average proton (or reactant) concentration over the reaction plane is proposed as a descriptor of the local reaction environment for such systems. The presented findings reveal that the double-layer overlap between NP and support plays a critical role in shaping local ion distributions, particularly near the NP–support interfacial region. The impacts of various key parameters, such as support material, NP size, NP coverage, electrolyte concentration, and electrode potential, on the local reaction environment have been explored.

(1) Support material: As the reactant concentration on the RP can be strongly raised

by a support material that attracts protons, a favorable support material for proton-consuming reactions is expected to have a more positive PZC than the catalyst NP.

(2) NP size: Smaller NPs exhibit a stronger double-layer overlap effect due to closer interactions with the support surface, resulting in higher reactant concentration. This effect diminishes with increasing NP size as the distance between the NP and support surface reduces the influence of double-layer overlap.

(3) NCSF or proximity: the interparticle distance has a minimal effect on proton distribution not only in high ionic strength solutions (100 mM), but also at low ionic strength (1 mM). This seemingly counter-intuitive observation shows that the local ion concentrations and the corresponding Gouy-Chapman length, rather than the bulk Debye length, govern the strength of interparticle double-layer overlap. The study identifies three prerequisites for a pronounced proximity effect: low bulk electrolyte concentration, electrode potential near the PZC of the support, and a relative PZC sequence that favors attraction of the ion species of interest, *viz*. either cations or anions, to the NP. In practice, these conditions are rarely met in real electrochemical environments.

(4) Electrode potential: Tuning the electrode potential closer to the PZC of the support can mitigate ion accumulation on the support surface, allowing the double-layer overlap effect to be visible.

(5) Bulk ion concentration: a reduction in bulk ion concentration amplifies the EDL overlap effect. However, for the NCSF/proximity effect to become noticeable, low bulk ion concentration serves as a necessary but not sufficient condition. The relative position of the electrode potential, the PZC of the catalyst NP, and the PZC of the support material play an important role in governing the NCSF/proximity effect.

To accurately capture the connection between the local reaction environment and electrochemical activity, I have defined a complementary descriptor that incorporates variations in local electrostatic potential. This descriptor accounts for the impact of variations in the local potential at the reaction plane on the driving force for electrochemical reactions. By combining this descriptor with the effective proton concentration, a unified activity descriptor is obtained. This combined descriptor incorporates the impact of the reaction order with respect to the proton concentration and the transfer coefficient in the kinetic rate equation, constituting a simplified variant of the Frumkin effects. It quantitatively reproduces current density trends, thereby linking the peculiar microscopic reaction environment of supported nanoparticle systems with observable electrochemical kinetics.

7. Conclusion and perspectives

This thesis presented attempts to extend the reach of theoretical treatments of electrochemical phenomena beyond those of oversimplified planar homogeneous electrodes toward realistic supported nanoparticle electrodes, with an emphasis on the interplay of electronic and ionic effects. The chosen method is based on the density–potential functional theory, with key concepts and equations presented in Chapter 2. Specifically, the theory has been extended to account for metal–solvent interactions, which are crucial for modelling systems composed of more than one metal. Chapter 3 presented a three-step calibration procedure to uniquely determine a set of parameters that reproduces experimental data of gold and silver, including work function, potential of zero charge and differential capacitance. Then, Fermi-level equilibration at the metal–metal contact interface has been illustrated using infinitely large slabs of gold and silver. A triple-layer structure of electron density perturbation and electric potential difference equal to Fermi-level difference have been visualized.

Chapter 4 studied the system of major interest—supported NP electrocatalysts. Taking use of its axial symmetry, we have assembled the supported NP system using a 2D cylindrical coordinate. The equilibrium distance between the jellium edges of NP and support has been identified by minimizing the system's total free energy as a function of the NP–support separation. I have investigated both global and local properties of the supported NP. The global work function and global PZC have been computed as a function of NP coverage. The perturbations in local electron density and local ion concentration have been revealed under both constant charge and constant potential conditions. In addition to the short-range charging at the NP–support contact interface, the analysis revealed the presence of excess charge at the external surfaces of both the NP and the support. An electric field covers the supported NP, pointing from the NP's external surface toward the support. Notably, the NP's external surface plays a more significant role than the contact interface, as catalytic reactions primarily occur there.

Under constant charge conditions, the electron redistribution is accompanied by ionic charge separation in the electrolyte. Studying the electron redistribution under constant potential conditions, two distinct charging mechanisms have been identified: ionic double-layer charging and dielectric support–NP charging. A seemingly counterintuitive phenomenon has been discussed: fixing the electrode potential at the PZC of an unsupported Ag NP, excess electronic and ionic charges of the same polarity coexist at the NP surface. Specifically, excess positive charge at the NP surface is not compensated by anion accumulation in the solution phase, but instead coexists with a surplus of cation. This is caused by the so-called double-layer overlap effect. The local ion distribution is dictated by the local electric potential, which depends not only on the surface charge of adjacent NP surface but also on the surface charge of support surface. Because the support surface is heavily negatively charged at the potential of zero charge of unsupported NP, the local electric potential is negative, leading to cation accumulation.

This phenomenon suggests that the classical concept of potential of zero charge is not sufficient to describe the charging behavior of heterogeneous supported NP. Therefore, two new concepts have been defined: the potential of zero local electronic charge and the potential of zero local ionic charge. While these two new characteristic potentials converge to the classical potential of zero charge at high electrolyte concentrations, they diverge in the low-concentration limit. Finally, it has beenfound that the differential capacitance of supported NPs can exhibit double-peak or triple-peak features, depending on NP size.

In Chapter 5, the DPFT results have been compared with DFT calculations, demonstrating a quantitative agreement in electronic perturbations. Chapter 6 studied the local reaction environment of supported NP catalyst. The average ion concentration at the reaction plane has been identified as a LRE descriptor, followed by a parametric study to analyze the impact of structural and compositional properties on the descriptor. To further rationalize its impact on electrochemical activity, I define a second LRE descriptor that incorporates the effect of the local electrostatic potential. An activity descriptor is defined by combining the two reaction-agnostic LRE descriptors with two reaction-specific kinetic parameters.

As potential future research directions, one can conduct certain experiments to validate our model results and also develop the DPFT methodology further to be able to apply to other systems.

Possible experimental validations are:

(1) Use ultraviolet photoelectron spectroscopy (UPS) to measure the global work function at a range of NP coverages and compare with our model predictions in Figure 33.

(2) Use off-axis electron holography to measure the phase shift of the electron beam passing through the space surrounding the supported NP. The phase shift is in principle related with the electric potential distribution, in particular, the integration of the electric potential along paths near the supported NP.

(3) Use electrochemical impedance spectroscopy to measure the impedance spectra and derive the capacitive response of the supported NP electrode, and compare with our model predictions in Figure 30 and Figure 31. Of course, a meaningful comparison requires the precise fabrication of supported NP electrodes with well-controlled particle size and interparticle distance.

Promising methodology development includes:

(1) Extend the DPFT model for application to oxide electrode, which is heavily used in water splitting. Now orbital-free DFT can only treat simple metal, but not oxide materials due to its small occupancy in Fermi level. In addition, oxide–electrolyte interface model also needs to be developed.

(2) Until now, chemisorption has been out of reach for the DPFT model. Further development is required to take reaction intermediates into account.

(3) Development of DPFT model is needed to extend the reach of theoretical treatments of electrochemical phenomena beyond those in equilibrium towards non-equilibrium conditions, *i.e.*, from zero reaction rate to non-zero steady-state rate.

8. Bibliography

[1] W. Ostwald, Lecture given in 1894, Reprinted in Z. Phys. Chem. **15**, 409 (1894).

[2] P. Friedlingstein et al., Global Carbon Budget 2021, Earth System Science Data **14**, 1917 (2022).

[3] Climate Action Tracker: Warming Projections Global Update, 2024.

[4] R. P. Allan, Frequently Asked Questions, The Intergovernmental Panel on Climate Change, 2021.

[5] W. J. Shaw et al., A US perspective on closing the carbon cycle to defossilize difficult-to-electrify segments of our economy, Nat. Rev. Chem. **8**, 376 (2024).

[6] K. M. Diederichsen, R. Sharifian, J. S. Kang, Y. Liu, S. Kim, B. M. Gallant, D. A. Vermaas, and T. A. Hatton, Electrochemical methods for carbon dioxide separations, Nat. Rev. Methods Primers **2**, (2022).

[7] I. A. Digdaya, I. Sullivan, M. Lin, L. Han, W.-H. Cheng, H. A. Atwater, and C. Xiang, A direct coupled electrochemical system for capture and conversion of CO2 from oceanwater, Nat. Commun. **11**, 4412 (2020).

[8] T. Yoshida and K. Kojima, Toyota MIRAI Fuel Cell Vehicle and Progress Toward a Future Hydrogen Society, Electrochem. Soc. Interface **24**, 45 (2015).

[9] E. J. Adler and J. R. R. A. Martins, Hydrogen-powered aircraft: Fundamental concepts, key technologies, and environmental impacts, Prog. Aerosp. Sci. **141**, 100922 (2023).

[10] K. Machaj, J. Kupecki, Z. Malecha, A. W. Morawski, M. Skrzypkiewicz, M. Stanclik, and M. Chorowski, Ammonia as a potential marine fuel: A review, Energy Strat. Rev. **44**, 100926 (2022).

[11] T. M. Gür, Review of electrical energy storage technologies, materials and systems: challenges and prospects for large-scale grid storage, Energy Environ. Sci. **11**, 2696 (2018).

[12] M. Chatenet et al., Water electrolysis: from textbook knowledge to the latest scientific strategies and industrial developments, Chem. Soc. Rev. **51**, 4583

(2022).

[13] A. R. Singh, B. A. Rohr, J. A. Schwalbe, M. Cargnello, K. Chan, T. F. Jaramillo, I. Chorkendorff, and J. K. Nørskov, Electrochemical Ammonia Synthesis—The Selectivity Challenge, ACS Catal. **7**, 706 (2017).

[14] H. Shen, C. Choi, J. Masa, X. Li, J. Qiu, Y. Jung, and Z. Sun, Electrochemical ammonia synthesis: Mechanistic understanding and catalyst design, Chem **7**, 1708 (2021).

[15] M. Li, J. Lu, Z. Chen, and K. Amine, 30 Years of Lithium-Ion Batteries, Adv. Mater. **30**, 1800561 (2018).

[16] A. Manthiram, X. Yu, and S. Wang, Lithium battery chemistries enabled by solid-state electrolytes, Nat. Rev. Mater. **2**, 1 (2017).

[17] M. W. Roberts, Birth of the catalytic concept (1800-1900), Catal. Lett. **67**, 1 (2000).

[18] *Chemical Process Catalysts: The Essential Ingredient for Industrial Chemical Reactions*, https://www.heraeus.com/en/hpm/hmp_products_solutions/heterogeneous_catalysts/chemical_process_catalysts/process_catalysts.html.

[19] U. Dingerdissen, A. Martin, D. Herein, and H. J. Wernicke, *The Development of Industrial Heterogeneous Catalysis*, in *Handbook of Heterogeneous Catalysis* (John Wiley & Sons, Ltd, 2008), pp. 37–56.

[20] S. Sui, X. Wang, X. Zhou, Y. Su, S. Riffat, and C. Liu, A comprehensive review of Pt electrocatalysts for the oxygen reduction reaction: Nanostructure, activity, mechanism and carbon support in PEM fuel cells, J. Mater. Chem. A **5**, 1808 (2017).

[21] T. Binninger and M.-L. Doublet, The Ir–OOOO–Ir transition state and the mechanism of the oxygen evolution reaction on IrO 2 (110), Energy Environ. Sci. **15**, 2519 (2022).

[22] S. Nitopi et al., Progress and Perspectives of Electrochemical CO2 Reduction on Copper in Aqueous Electrolyte, Chem. Rev. **119**, 7610 (2019).

[23] P. Sabatier, *La catalyse en chimie organique* (Librairie polytechnique, Paris et Liege, 1920).

[24] J. K. Nørskov, J. Rossmeisl, A. Logadottir, L. Lindqvist, J. R. Kitchin, T. Bligaard, and H. Jónsson, Origin of the Overpotential for Oxygen Reduction at a Fuel-Cell Cathode, J. Phys. Chem. B **108**, 46 (2004).

[25] R. Parsons, The rate of electrolytic hydrogen evolution and the heat of adsorption of hydrogen, Trans. Faraday Soc. **54**, 0 (1958).

[26] H. Gerischer, Mechanismus der Elektrolytischen Wasserstoffabscheidung und Adsorptionsenergie von Atomarem Wasserstoff, Bulletin des Sociétés Chimiques Belges **67**, 7–8 (1958).

[27] S. Trasatti, Work function, electronegativity, and electrochemical behaviour of metals: III. Electrolytic hydrogen evolution in acid solutions, J. Electroanal. Chem. Interfacial Electrochem. **39**, 1 (1972).

[28] Paul. Delahay and C. W. . Tobias, *Advances in Electrochemistry and Electrochemical Engineering Volume 7, Volume 7,* (Interscience Publishers, New York; London; Sydney [Etc.], 1970).

[29] K. S. Exner, Beyond the Traditional Volcano Concept: Overpotential-Dependent Volcano Plots Exemplified by the Chlorine Evolution Reaction over Transition-Metal Oxides, J. Phys. Chem. C **123**, 27 (2019).

[30] H. Ooka and R. Nakamura, Shift of the Optimum Binding Energy at Higher Rates of Catalysis, J. Phys. Chem. Lett. **10**, 21 (2019).

[31] Y. Zhang, J. Zhang, and J. Huang, Potential-Dependent Volcano Plot for Oxygen Reduction: Mathematical Origin and Implications for Catalyst Design, J. Phys. Chem. Lett. **10**, 22 (2019).

[32] Y. Zhang, J. Huang, and M. Eikerling, Criterion for finding the optimal electrocatalyst at any overpotential, Electrochim. Acta **400**, 139413 (2021).

[33] W. Schmickler and E. Santos, *Interfacial Electrochemistry* (Springer Science & Business Media, 2010).

[34] T. Pajkossy, T. Wandlowski, and D. M. Kolb, Impedance aspects of anion

adsorption on gold single crystal electrodes, J. Electroanal. Chem. **414**, 209 (1996).

[35] L. Zhang and J. Huang, Measurement and interpretation of the double layer capacitance of Pt(111)/aqueous solution interfaces, Curr. Opin. Electrochem. 101419 (2023).

[36] A. A. Kornyshev, Double-Layer in Ionic Liquids: Paradigm Change?, J. Phys. Chem. B **111**, 5545 (2007).

[37] G. Valette, Double layer on silver single crystal electrodes in contact with electrolytes having anions which are slightly specifically adsorbed: Part III. The (111) face, J. Electroanal. Chem. & Interfacial Electrochem. **269**, 191 (1989).

[38] C. D. Koolen, W. Luo, and A. Züttel, From Single Crystal to Single Atom Catalysts: Structural Factors Influencing the Performance of Metal Catalysts for CO2 Electroreduction, ACS Catal. **13**, 948 (2023).

[39] L. Liu and A. Corma, Metal Catalysts for Heterogeneous Catalysis: From Single Atoms to Nanoclusters and Nanoparticles, Chem. Rev. **118**, 4981 (2018).

[40] R. T. Hannagan, G. Giannakakis, M. Flytzani-Stephanopoulos, and E. C. H. Sykes, Single-Atom Alloy Catalysis, Chem. Rev. **120**, 12044 (2020).

[41] J.-C. Wasilke, S. J. Obrey, R. T. Baker, and G. C. Bazan, Concurrent Tandem Catalysis, Chem. Rev. **105**, 1001 (2005).

[42] C. Pei and J. Gong, Tandem catalysis at nanoscale, Science **371**, 1203 (2021).

[43] M. B. Gawande, A. Goswami, T. Asefa, H. Guo, A. V. Biradar, D.-L. Peng, R. Zboril, and R. S. Varma, Core–shell nanoparticles: synthesis and applications in catalysis and electrocatalysis, Chem. Soc. Rev. **44**, 7540 (2015).

[44] X. Wang, C. Xu, M. Jaroniec, Y. Zheng, and S.-Z. Qiao, Anomalous hydrogen evolution behavior in high-pH environment induced by locally generated hydronium ions, Nat. Commun. **10**, 4876 (2019).

[45] B. James, J. Huya-Kouadio, and C. Houchins, *Mass Production Cost Estimation of Direct H2 PEM Fuel Cell Systems for Transportation Applications: 2015 Update* (2015).

[46] C. T. Campbell, The energetics of supported metal nanoparticles: relationships to sintering rates and catalytic activity, Acc Chem Res **46**, 1712 (2013).

[47] W. Zhu, R. Michalsky, Ö. Metin, H. Lv, S. Guo, C. J. Wright, X. Sun, A. A. Peterson, and S. Sun, Monodisperse Au Nanoparticles for Selective Electrocatalytic Reduction of CO2 to CO, J. Am. Chem. Soc. **135**, 16833 (2013).

[48] Y. Kameya, T. Hayashi, and M. Motosuke, Stability of platinum nanoparticles supported on surface-treated carbon black, Appl. Catal. B: Environ **189**, 219 (2016).

[49] Y. Ni, L. Yao, Y. Wang, B. Liu, M. Cao, and C. Hu, Construction of hierarchically porous graphitized carbon-supported NiFe layered double hydroxides with a core–shell structure as an enhanced electrocatalyst for the oxygen evolution reaction, Nanoscale **9**, 11596 (2017).

[50] F. Karimi and B. A. Peppley, Metal Carbide and Oxide Supports for Iridium-Based Oxygen Evolution Reaction Electrocatalysts for Polymer-Electrolyte-Membrane Water Electrolysis, Electrochim. Acta **246**, 654 (2017).

[51] X. Peng, S. G. Karakalos, and W. E. Mustain, Preferentially Oriented Ag Nanocrystals with Extremely High Activity and Faradaic Efficiency for CO2 Electrochemical Reduction to CO, ACS Appl. Mater. Interfaces **10**, 1734 (2018).

[52] W. Hu, S. Chen, and Q. Xia, IrO2/Nb–TiO2 electrocatalyst for oxygen evolution reaction in acidic medium, Int. J. Hydrogen Energy **39**, 6967 (2014).

[53] I. N. Leontyev, S. V. Belenov, V. E. Guterman, P. Haghi-Ashtiani, A. P. Shaganov, and B. Dkhil, Catalytic Activity of Carbon-Supported Pt Nanoelectrocatalysts. Why Reducing the Size of Pt Nanoparticles is Not Always Beneficial, J. Phys. Chem. C **115**, 5429 (2011).

[54] F. J. Perez-Alonso, D. N. McCarthy, A. Nierhoff, P. Hernandez-Fernandez, C. Strebel, I. E. L. Stephens, J. H. Nielsen, and I. Chorkendorff, The Effect of Size on the Oxygen Electroreduction Activity of Mass-Selected Platinum Nanoparticles, Angew. Chem. Int. Ed. **51**, 4641 (2012).

[55] E. Roduner, Size matters: why nanomaterials are different, Chem. Soc. Rev. **35**, 583 (2006).

[56] R. Kubo, Electronic Properties of Metallic Fine Particles. I., J. Phys. Soc. Jpn. **17**, 975 (1962).

[57] M. Nesselberger et al., The effect of particle proximity on the oxygen reduction rate of size-selected platinum clusters, Nat. Mater. **12**, 919 (2013).

[58] J. Huang, J. Zhang, and M. H. Eikerling, Particle Proximity Effect in Nanoparticle Electrocatalysis: Surface Charging and Electrostatic Interactions, J. Phys. Chem. C **121**, 4806 (2017).

[59] G. Pacchioni and H.-J. Freund, Controlling the charge state of supported nanoparticles in catalysis: lessons from model systems, Chem. Soc. Rev. **47**, 8474 (2018).

[60] C. Hernández Mejía, T. van Deelen, and K. De Jong, Control of metal-support interactions in heterogeneous catalysts to enhance activity and selectivity, Nat. Catal. **2**, 955 (2019).

[61] C. T. Campbell, Electronic perturbations, Nat. Chem. **4**, 597 (2012).

[62] B. Hammer, Special Sites at Noble and Late Transition Metal Catalysts, Top. Catal. **37**, 3 (2006).

[63] W. C. Conner Jr and J. L. Falconer, Spillover in heterogeneous catalysis, Chem. Rev. **95**, 759 (1995).

[64] R. Prins, Hydrogen Spillover. Facts and Fiction, Chem. Rev. **112**, 2714 (2012).

[65] B. Roldan Cuenya, Metal Nanoparticle Catalysts Beginning to Shape-up, Acc. Chem. Res. **46**, 1682 (2013).

[66] T. Nilsson Pingel, M. Jørgensen, A. B. Yankovich, H. Grönbeck, and E. Olsson, Influence of atomic site-specific strain on catalytic activity of supported nanoparticles, Nat. Commun. **9**, 2722 (2018).

[67] T. Wang, J. Hu, R. Ouyang, Y. Wang, Y. Huang, S. Hu, and W.-X. Li, Nature of metal-support interaction for metal catalysts on oxide supports, Science **386**, 915 (2024).

[68] T. Ishida, T. Murayama, A. Taketoshi, and M. Haruta, Importance of Size and

Contact Structure of Gold Nanoparticles for the Genesis of Unique Catalytic Processes, Chem. Rev. **120**, 464 (2020).

[69] H. Frey, A. Beck, X. Huang, J. A. van Bokhoven, and M. G. Willinger, Dynamic interplay between metal nanoparticles and oxide support under redox conditions, Science **376**, 982 (2022).

[70] M. G. Willinger, W. Zhang, O. Bondarchuk, S. Shaikhutdinov, H.-J. Freund, and R. Schlögl, A Case of Strong Metal–Support Interactions: Combining Advanced Microscopy and Model Systems to Elucidate the Atomic Structure of Interfaces, Angew. Chem. Int. Ed. **53**, 5998 (2014).

[71] S. Zhang, P. N. Plessow, J. J. Willis, S. Dai, M. Xu, G. W. Graham, M. Cargnello, F. Abild-Pedersen, and X. Pan, Dynamical Observation and Detailed Description of Catalysts under Strong Metal–Support Interaction, Nano Lett. **16**, 4528 (2016).

[72] R. Jinnouchi and A. B. Anderson, Electronic structure calculations of liquid-solid interfaces: Combination of density functional theory and modified Poisson-Boltzmann theory, Phys. Rev. B **77**, 245417 (2008).

[73] V. Tripkovic, M. E. Björketun, E. Skúlason, and J. Rossmeisl, Standard hydrogen electrode and potential of zero charge in density functional calculations, Phys. Rev. B **84**, 115452 (2011).

[74] K. Letchworth-Weaver and T. A. Arias, Joint density functional theory of the electrode-electrolyte interface: Application to fixed electrode potentials, interfacial capacitances, and potentials of zero charge, Phys. Rev. B **86**, 075140 (2012).

[75] S. Sakong, K. Forster-Tonigold, and A. Groß, The structure of water at a Pt(111) electrode and the potential of zero charge studied from first principles, J. Chem. Phys. **144**, 194701 (2016).

[76] J. Le, M. Iannuzzi, A. Cuesta, and J. Cheng, Determining Potentials of Zero Charge of Metal Electrodes versus the Standard Hydrogen Electrode from Density-Functional-Theory-Based Molecular Dynamics, Phys. Rev. Lett. **119**, 1 (2017).

[77] S. Nishihara and M. Otani, Hybrid solvation models for bulk, interface, and membrane: Reference interaction site methods coupled with density functional theory, Phys. Rev. B **96**, 115429 (2017).

[78] J. P. Badiali, M. L. Rosinberg, and J. Goodisman, Contribution of the metal to the differential capacity of an ideally polarisable electrode, J. Electroanal. Chem. Interfacial Electrochem. **143**, 73 (1983).

[79] J. P. Badiali, M. L. Rosinberg, F. Vericat, and L. Blum, A microscopic model for the liquid metal-ionic solution interface, J. Electroanal. Chem. Interfacial Electrochem. **158**, 253 (1983).

[80] W. Schmickler, A jellium-dipole model for the double layer, J. Electroanal. Chem. Interfacial Electrochem. **150**, 19 (1983).

[81] W. Schmickler and D. Henderson, The interphase between jellium and a hard sphere electrolyte. A model for the electric double layer, J. Chem. Phys. **80**, 3381 (1984).

[82] V. I. Feldman, A. A. Kornyshev, and M. B. Partenskiĭ, Density functional simulation of interfacial relaxation and capacity of a model metal/electrolyte interface, Solid State Commun. **53**, 157 (1985).

[83] A. A. Kornyshev, Metal electrons in the double layer theory, Electrochim. Acta **34**, 1829 (1989).

[84] A. Gupta, A. Govind Rajan, E. A. Carter, and H. A. Stone, Ionic Layering and Overcharging in Electrical Double Layers in a Poisson-Boltzmann Model, Phys. Rev. Lett. **125**, 188004 (2020).

[85] M. Z. Bazant, B. D. Storey, and A. A. Kornyshev, Double Layer in Ionic Liquids: Overscreening versus Crowding, Phys. Rev. Lett. **106**, 046102 (2011).

[86] J. P. de Souza, Z. A. H. Goodwin, M. McEldrew, A. A. Kornyshev, and M. Z. Bazant, Interfacial Layering in the Electric Double Layer of Ionic Liquids, Phys. Rev. Lett. **125**, 116001 (2020).

[87] Y. Avni, R. M. Adar, and D. Andelman, Charge oscillations in ionic liquids: A microscopic cluster model, Phys. Rev. E **101**, 010601 (2020).

[88] H. Helmholtz, Studien über electrische Grenzschichten, Annalen Der Physik **243**, 7 (1879).

[89] M. Gouy, Sur la constitution de la charge électrique à la surface d'un électrolyte, J. Phys. Theor. Appl. **9**, 1 (1910).

[90] D. L. Chapman, LI. A contribution to the theory of electrocapillarity, London, Edinburgh Dublin Philos. Mag. J. Sci **25**, 475 (1913).

[91] O. Stern, ZUR THEORIE DER ELEKTROLYTISCHEN DOPPELSCHICHT, Z. Elektrochem. Angew. Phys. Chem. **30**, 508 (1924).

[92] J. O. Bockris, The structure of water in the double layer, Inorg. Chim. Acta. **40**, X14 (1980).

[93] J. J. Bikerman, XXXIX. Structure and capacity of electrical double layer, London, Edinburgh, Dublin Philos. Mag. J. Sci **33**, 384 (1942).

[94] M. S. Kilic, M. Z. Bazant, and A. Ajdari, Steric effects in the dynamics of electrolytes at large applied voltages. I. Double-layer charging, Phys. Rev. E **75**, 021502 (2007).

[95] I. Borukhov, D. Andelman, and H. Orland, Steric Effects in Electrolytes: A Modified Poisson-Boltzmann Equation, Phys. Rev. Lett. **79**, 435 (1997).

[96] Y. Zhang and J. Huang, Treatment of Ion-Size Asymmetry in Lattice-Gas Models for Electrical Double Layer, J. Phys. Chem. C **122**, 28652 (2018).

[97] M. Valiskó, T. Kristóf, D. Gillespie, and D. Boda, A systematic Monte Carlo simulation study of the primitive model planar electrical double layer over an extended range of concentrations, electrode charges, cation diameters and valences, AIP Adv. **8**, 025320 (2018).

[98] L. Scalfi, M. Salanne, and B. Rotenberg, Molecular Simulation of Electrode-Solution Interfaces, Annu. Rev. Phys. Chem. **72**, 189 (2021).

[99] J. Wu, Understanding the Electric Double-Layer Structure, Capacitance, and Charging Dynamics, Chem. Rev. **122**, 10821 (2022).

[100] Z. Wang, L. Liu, and I. Neretnieks, The weighted correlation approach for density

functional theory: a study on the structure of the electric double layer, J. Phys.: Condens. Matter **23**, 175002 (2011).

[101] R. Roth, Fundamental measure theory for hard-sphere mixtures: a review, J. Phys.: Condens. Matter **22**, 063102 (2010).

[102] Y.-X. Yu and J. Wu, Structures of hard-sphere fluids from a modified fundamental-measure theory, J Chem. Phys. **117**, 10156 (2002).

[103] A. Frumkin, XLIII. On the theory of electrocapillarity: II, London, Edinburgh, Dublin Philos. Mag. J. Sci **40**, 375 (1920).

[104] O. K. Rice, Application of the Fermi Statistics to the Distribution of Electrons Under Fields in Metals and the Theory of Electrocapillarity, Phys. Rev. **31**, 1051 (1928).

[105] S. Luryi, Quantum capacitance devices, Appl. Phys. Lett. **52**, 501 (1988).

[106] S. Fleischmann, J. B. Mitchell, R. Wang, C. Zhan, D. Jiang, V. Presser, and V. Augustyn, Pseudocapacitance: From Fundamental Understanding to High Power Energy Storage Materials, Chem. Rev. **120**, 6738 (2020).

[107] N. D. Lang and W. Kohn, Theory of Metal Surfaces: Charge Density and Surface Energy, Phys. Rev. B **1**, 4555 (1970).

[108] N. D. Lang, *The Density-Functional Formalism and the Electronic Structure of Metal Surfaces*, in *Solid State Physics*, edited by H. Ehrenreich, F. Seitz, and D. Turnbull, Vol. 28 (Academic Press, 1974), pp. 225–300.

[109] S. M. R. Islam, F. Khezeli, S. Ringe, and C. Plaisance, An implicit electrolyte model for plane wave density functional theory exhibiting nonlinear response and a nonlocal cavity definition, J Chem. Phys. **159**, 234117 (2023).

[110] E. Brunk and U. Rothlisberger, Mixed Quantum Mechanical/Molecular Mechanical Molecular Dynamics Simulations of Biological Systems in Ground and Electronically Excited States, Chem. Rev. **115**, 6217 (2015).

[111] J. Huang, Density-Potential Functional Theory of Electrochemical Double Layers: Calibration on the Ag(111)-KPF6 System and Parametric Analysis, J. Chem. Theory Comput. **19**, 1003 (2023).

[112] A. Warshel and M. Levitt, Theoretical studies of enzymic reactions: Dielectric, electrostatic and steric stabilization of the carbonium ion in the reaction of lysozyme, J. Mol. Biol. **103**, 227 (1976).

[113] G. Adrian Bramley, O. Tomos Beynon, P. Viktorovich Stishenko, and A. James Logsdail, The application of QM/MM simulations in heterogeneous catalysis, Phys. Chem. Chem. Phys. **25**, 6562 (2023).

[114] D. M. Hayes and P. A. Kollman, Electrostatic potentials of proteins. 2. Role of electrostatics in a possible catalytic mechanism for carboxypeptidase A, J. Am. Chem. Soc. **98**, 7811 (1976).

[115] R. Tesch, P. M. Kowalski, and M. H. Eikerling, Properties of the Pt(111)/electrolyte electrochemical interface studied with a hybrid DFT–solvation approach, J. Phys.: Condens. Matter **33**, 444004 (2021).

[116] M. Otani and O. Sugino, First-principles calculations of charged surfaces and interfaces: A plane-wave nonrepeated slab approach, Phys. Rev. B **73**, 115407 (2006).

[117] K. Mathew, V. S. C. Kolluru, S. Mula, S. N. Steinmann, and R. G. Hennig, Implicit self-consistent electrolyte model in plane-wave density-functional theory, J. Chem. Phys. **151**, 234101 (2019).

[118] S. A. Petrosyan, A. A. Rigos, and T. A. Arias, Joint Density-Functional Theory: Ab Initio Study of Cr2O3 Surface Chemistry in Solution, J. Phys. Chem. B **109**, 15436 (2005).

[119] M. M. Melander, Grand Canonical Rate Theory for Electrochemical and Electrocatalytic Systems I: General Formulation and Proton-coupled Electron Transfer Reactions, J. Electrochem. Soc. **167**, 116518 (2020).

[120] J. Dziedzic, A. Bhandari, L. Anton, C. Peng, J. C. Womack, M. Famili, D. Kramer, and C.-K. Skylaris, Practical Approach to Large-Scale Electronic Structure Calculations in Electrolyte Solutions via Continuum-Embedded Linear-Scaling Density Functional Theory, J. Phys. Chem. C **124**, 7860 (2020).

[121] M. J. Eslamibidgoli and M. H. Eikerling, Approaching the self-consistency challenge of electrocatalysis with theory and computation, Curr. Opin.

Electrochem. **9**, 189 (2018).

[122] J. Huang, Mixed quantum-classical treatment of electron transfer at electrocatalytic interfaces: Theoretical framework and conceptual analysis, J Chem. Phys. **153**, 164707 (2020).

[123] J. Huang, S. Chen, and M. Eikerling, Grand-Canonical Model of Electrochemical Double Layers from a Hybrid Density–Potential Functional, J. Chem. Theory Comput. **17**, 2417 (2021).

[124] J. Huang, Hybrid density-potential functional theory of electric double layers, Electrochim. Acta **389**, 138720 (2021).

[125] J. Huang, F. Domínguez-Flores, and M. Melander, Variants of Surface Charges and Capacitances in Electrocatalysis: Insights from Density-Potential Functional Theory Embedded with an Implicit Chemisorption Model, PRX Energy **3**, 043008 (2024).

[126] Y. Zhang, T. Binninger, J. Huang, and M. H. Eikerling, Theory of Electro-Ionic Perturbations at Supported Electrocatalyst Nanoparticles, Phys. Rev. Lett. **134**, 066201 (2025).

[127] W. R. Fawcett, Monte Carlo studies of ion size effects in the diffuse double layer, Electrochim. Acta **54**, 4997 (2009).

[128] G. M. Torrie and J. P. Valleau, A Monte Carlo study of an electrical double layer, Chem. Phys. Lett. **65**, 343 (1979).

[129] C. Merlet, B. Rotenberg, P. A. Madden, P.-L. Taberna, P. Simon, Y. Gogotsi, and M. Salanne, On the molecular origin of supercapacitance in nanoporous carbon electrodes, Nat. Mater. **11**, 306 (2012).

[130] S. Ringe, N. G. Hörmann, H. Oberhofer, and K. Reuter, Implicit Solvation Methods for Catalysis at Electrified Interfaces, Chem. Rev. **122**, 12 (2022).

[131] R. Sundararaman, W. A. Goddard, and T. A. Arias, Grand canonical electronic density-functional theory: Algorithms and applications to electrochemistry, J. Chem. Phys. **146**, 11 (2017).

[132] K. Schwarz and R. Sundararaman, The electrochemical interface in first-

principles calculations, Surf. Sci. Rep. **75**, 100492 (2020).

[133] A. Groß, Grand-canonical approaches to understand structures and processes at electrochemical interfaces from an atomistic perspective, Curr. Opin. Electrochem. **27**, 100684 (2021).

[134] T. Binninger, T. J. Schmidt, and D. Kramer, Capacitive electronic metal-support interactions: Outer surface charging of supported catalyst particles, Phys. Rev. B **96**, 165405 (2017).

[135] M. Zhou, A. Zhang, Z. Dai, Y. P. Feng, and C. Zhang, Strain-Enhanced Stabilization and Catalytic Activity of Metal Nanoclusters on Graphene, J. Phys. Chem. C **114**, 16541 (2010).

[136] L. H. Thomas, The calculation of atomic fields, Math. Proc. Camb. Philos. Soc. **23**, 5 (1927).

[137] E. Fermi, Eine statistische Methode zur Bestimmung einiger Eigenschaften des Atoms und ihre Anwendung auf die Theorie des periodischen Systems der Elemente, Z. Physik **48**, 73 (1928).

[138] Y. Zhang, T. Ye, M. Chen, Z. A. H. Goodwin, G. Feng, J. Huang, and A. A. Kornyshev, Enforced Freedom: Electric-Field-Induced Declustering of Ionic-Liquid Ions in the Electrical Double Layer, Energy Environ. Mater. **3**, 414 (2020).

[139] N. Bruch, T. Binninger, J. Huang, and M. Eikerling, Incorporating Electrolyte Correlation Effects into Variational Models of Electrochemical Interfaces, J. Phys. Chem. Lett. **15**, 2015 (2024).

[140] S. Lundqvist and N. H. March, *Theory of the Inhomogeneous Electron Gas* (Springer Science & Business Media, 2013).

[141] W. Kohn and L. J. Sham, Self-Consistent Equations Including Exchange and Correlation Effects, Phys. Rev. **140**, 4A (1965).

[142] J. P. Perdew and S. Kurth, *Density Functionals for Non-Relativistic Coulomb Systems in the New Century*, in *A Primer in Density Functional Theory*, edited by C. Fiolhais, F. Nogueira, and M. A. L. Marques (Springer Berlin Heidelberg, Berlin, Heidelberg, 2003), pp. 1–55.

[143] S. Trasatti and L. M. Doubova, Crystal-face specificity of electrical double-layer parameters at metal/solution interfaces, J. Chem. Soc., Faraday Trans. **91**, 3311 (1995).

[144] W. Schmickler, Electronic Effects in the Electric Double Layer, Chem. Rev. **96**, 3177 (1996).

[145] H. Ogasawara, B. Brena, D. Nordlund, M. Nyberg, A. Pelmenschikov, L. G. M. Pettersson, and A. Nilsson, Structure and Bonding of Water on Pt(111), Phys. Rev. Lett. **89**, 276102 (2002).

[146] A. Groß and S. Sakong, Ab Initio Simulations of Water/Metal Interfaces, Chem. Rev. **122**, 10746 (2022).

[147] J. Le, Q. Fan, J. Li, and J. Cheng, Molecular origin of negative component of Helmholtz capacitance at electrified Pt(111)/water interface, Sci. Adv. **6**, eabb1219 (2020).

[148] P. Li, J. Huang, Y. Hu, and S. Chen, Establishment of the Potential of Zero Charge of Metals in Aqueous Solutions: Different Faces of Water Revealed by Ab Initio Molecular Dynamics Simulations, J. Phys. Chem. C **125**, 3972 (2021).

[149] S. Schnur and A. Groß, Properties of metal–water interfaces studied from first principles, New J. Phys. **11**, 125003 (2009).

[150] S. R. Kelly, H. H. Heenen, N. Govindarajan, K. Chan, and J. K. Nørskov, OH Binding Energy as a Universal Descriptor of the Potential of Zero Charge on Transition Metal Surfaces, J. Phys. Chem. C **126**, 5521 (2022).

[151] P. A. Thiel and T. E. Madey, The interaction of water with solid surfaces: Fundamental aspects, Surf. Sci. Rep. **7**, 6 (1987).

[152] M. A. Henderson, The interaction of water with solid surfaces: fundamental aspects revisited, Surf. Sci. Rep. **46**, 1 (2002).

[153] N. Garcia-Araez, V. Climent, and J. Feliu, Potential-Dependent Water Orientation on Pt(111), Pt(100), and Pt(110), As Inferred from Laser-Pulsed Experiments. Electrostatic and Chemical Effects, J. Phys. Chem. C **113**, 9290 (2009).

[154] S. Sakong and A. Groß, Water structures on a Pt(111) electrode from ab initio molecular dynamic simulations for a variety of electrochemical conditions, Phys. Chem. Chem. Phys. **22**, 10431 (2020).

[155] G. Kresse and D. Joubert, From ultrasoft pseudopotentials to the projector augmented-wave method, Phys. Rev. B **59**, 1758 (1999).

[156] S. Grimme, S. Ehrlich, and L. Goerigk, Effect of the damping function in dispersion corrected density functional theory, J. Comput. Chem. **32**, 1456 (2011).

[157] D. R. Lide, *CRC Handbook of Chemistry and Physics, 88th Edition* (Taylor & Francis, 2007).

[158] K. Mathew, R. Sundararaman, K. Letchworth-Weaver, T. A. Arias, and R. G. Hennig, Implicit solvation model for density-functional study of nanocrystal surfaces and reaction pathways, J. Chem. Phys. **140**, 084106 (2014).

[159] R. Buchner, G. T. Hefter, and P. M. May, Dielectric Relaxation of Aqueous NaCl Solutions, J. Phys. Chem. A **103**, 1 (1999).

[160] P. W. Kang, G.-M. Kim, R. Haaring, J. W. Lee, S. S. Jeon, D. C. Lee, and H. Lee, Applying Plasmonic Catalyst in CO2 Electrolyzer for Enhancing Energy Efficiency, ACS Energy Lett. 4941 (2023).

[161] E. E. Huber Jr., The Effect of Mercury Contamination on the Work Function of Gold, Appl. Phys. Lett. **8**, 169 (2004).

[162] R. P. W. Lawson and G. Carter, The Desorption of Mercury and the Work Function of Polycrystalline Gold, Appl. Phys. Lett. **9**, 85 (2004).

[163] J. Clavilier and C. N. Van Huong, Etude de l’interface de l’or polycristallin au contact de solutions aqueuses de perchlorate de potassium et d’acide perchlorique, Journal of Electroanalytical Chemistry and Interfacial Electrochemistry **80**, 101 (1977).

[164] Z. Samec and K. Doblhofer, Mechanism of peroxodisulfate reduction at a polycrystalline gold electrode, J. Electroanal. Chem. **367**, 141 (1994).

[165] M Chelvayohan and C H B Mee, Work function measurements on (110), (100)

and (111) surfaces of silver, J Phys. C: Solid State Phys. **15**, 2305 (1982).

[166] H. E. Farnsworth and R. P. Winch, Photoelectric Work Functions of (100) and (111) Faces of Silver Single Crystals and Their Contact Potential Difference, Phys. Rev. **58**, 812 (1940).

[167] S. Trishin, T. Müller, D. Rolf, C. Lotze, P. Rietsch, S. Eigler, B. Meyer, and K. J. Franke, Resolution of Intramolecular Dipoles and a Push-Back Effect of Individual Molecules on a Metal Surface, J. Phys. Chem. C **126**, 7667 (2022).

[168] E. C. Akubuiro and X. E. Verykios, Dopant-induced metal-support interactions: 1. Influence on chemisorptive behavior, J. Catal. **103**, 320 (1987).

[169] M. Ahmadi, H. Mistry, and B. Roldan Cuenya, Tailoring the Catalytic Properties of Metal Nanoparticles via Support Interactions, J. Phys. Chem. Lett. **7**, (2016).

[170] C. Dong, Y. Li, D. Cheng, M. Zhang, J. Liu, Y.-G. Wang, D. Xiao, and D. Ma, Supported Metal Clusters: Fabrication and Application in Heterogeneous Catalysis, ACS Catal. **10**, 11011 (2020).

[171] V. A. Saveleva et al., Insight into the Mechanisms of High Activity and Stability of Iridium Supported on Antimony-Doped Tin Oxide Aerogel for Anodes of Proton Exchange Membrane Water Electrolyzers, ACS Catal. **10**, 2508 (2020).

[172] T. Binninger, Electronic Metal-Support Interactions in Vacuum vs. Electrolyte, Nat. Comm. **11**, 1471 (2020).

[173] V. T. T. Ho, C.-J. Pan, J. Rick, W.-N. Su, and B.-J. Hwang, Nanostructured Ti0.7Mo0.3O2 Support Enhances Electron Transfer to Pt: High-Performance Catalyst for Oxygen Reduction Reaction, J. Am. Chem. Soc. **133**, 11716 (2011).

[174] K. Fujiwara, K. Okuyama, and S. E. Pratsinis, Metal–support interactions in catalysts for environmental remediation, Environ. Sci.: Nano **4**, 2076 (2017).

[175] S. B. Trung Tran, H. S. Choi, S. Y. Oh, S. Y. Moon, and J. Y. Park, Iron-doped ZnO as a support for Pt-based catalysts to improve activity and stability: enhancement of metal–support interaction by the doping effect, RSC Adv. **8**, 21528 (2018).

[176] Y. Wang, D. Widmann, and R. J. Behm, Influence of TiO2 Bulk Defects on CO

Adsorption and CO Oxidation on Au/TiO2: Electronic Metal–Support Interactions (EMSIs) in Supported Au Catalysts, ACS Catal. **7**, 2339 (2017).

[177] Y. Lykhach et al., Counting electrons on supported nanoparticles., Nat. Mater. **15 3**, 284 (2016).

[178] M. J. Zachman, V. Fung, F. Polo-Garzon, S. Cao, J. Moon, Z. Huang, D. Jiang, Z. Wu, and M. Chi, Measuring and directing charge transfer in heterogenous catalysts, Nat Commun **13**, 3253 (2022).

[179] R. Aso et al., Direct identification of the charge state in a single platinum nanoparticle on titanium oxide, Science **378**, 202 (2022).

[180] C. Jackson, G. T. Smith, D. W. Inwood, A. S. Leach, P. S. Whalley, M. Callisti, T. Polcar, A. E. Russell, P. Levecque, and D. Kramer, Electronic metal-support interaction enhanced oxygen reduction activity and stability of boron carbide supported platinum, Nat. Commun. **8**, 15802 (2017).

[181] N. Holmberg, K. Laasonen, and P. Peljo, Charge distribution and Fermi level in bimetallic nanoparticles, Phys. Chem. Chem. Phys. **18**, 2924 (2016).

[182] P. Peljo, J. A. Manzanares, and H. H. Girault, Contact Potentials, Fermi Level Equilibration, and Surface Charging, Langmuir **32**, 5765 (2016).

[183] P. Peljo, J. A. Manzanares, and H. H. Girault, Variation of the Fermi level and the electrostatic force of a metallic nanoparticle upon colliding with an electrode, Chem. Sci. **8**, 4795 (2017).

[184] L. G. Verga, A. E. Russell, and C.-K. Skylaris, Ethanol, O, and CO adsorption on Pt nanoparticles: effects of nanoparticle size and graphene support, Phys. Chem. Chem. Phys. **20**, 25918 (2018).

[185] K. Iida, Atomic-Scale Picture of the Electric Double Layer around a Heterogeneous Solid–Liquid Interface Based on 3D-RISM-SCF Theory, J. Phys. Chem. C **126**, 9466 (2022).

[186] I. V. Yudanov, A. Genest, S. Schauermann, H.-J. Freund, and N. Rösch, Size Dependence of the Adsorption Energy of CO on Metal Nanoparticles: A DFT Search for the Minimum Value, Nano Lett. **12**, 2134 (2012).

[187] G.-M. Schwab, J. Block, and D. Schultze, Kontaktkatalytische Verstärkung durch dotierte Träger, Angew. Chem. **71**, 101 (1959).

[188] A. Bruix, J. A. Rodriguez, P. J. Ramírez, S. D. Senanayake, J. Evans, J. B. Park, D. Stacchiola, P. Liu, J. Hrbek, and F. Illas, A New Type of Strong Metal–Support Interaction and the Production of H2 through the Transformation of Water on Pt/CeO2(111) and Pt/CeOx/TiO2(110) Catalysts, J. Am. Chem. Soc. **134**, 8968 (2012).

[189] O. Bezkrovnyi et al., Metal–Support Interaction and Charge Distribution in Ceria-Supported Au Particles Exposed to CO, Chem. Mater. **34**, 7916 (2022).

[190] X. Chen, G. Kastlunger, and A. A. Peterson, Fundamental Drivers of Electrochemical Barriers, Phys. Rev. Lett. **131**, 23 (2023).

[191] C. Chen, H. Jin, P. Wang, X. Sun, M. Jaroniec, Y. Zheng, and S. Qiao, Local reaction environment in electrocatalysis, Chem. Soc. Rev. **53**, 2022 (2024).

[192] H. H. Girault, *Analytical and Physical Electrochemistry* (EPFL Press, New York, 2004).

[193] A. Szabo and N. S. Ostlund., *Modern Quantum Chemistry: Introduction to Advanced Electronic Structure Theory* (Courier Corporation, 1996).

[194] F. Jensen, *Introduction to Computational Chemistry* (John wiley & sons, 2017).

[195] P. Hohenberg and W. Kohn, Inhomogeneous Electron Gas, Phys. Rev. **136**, B864 (1964).

[196] J. P. Perdew, K. Burke, and M. Ernzerhof, Generalized Gradient Approximation Made Simple, Phys. Rev. Lett. **77**, 3865 (1996).

[197] J. Tao, J. P. Perdew, V. N. Staroverov, and G. E. Scuseria, Climbing the Density Functional Ladder: Nonempirical Meta--Generalized Gradient Approximation Designed for Molecules and Solids, Phys. Rev. Lett. **91**, 146401 (2003).

[198] J. Heyd, G. E. Scuseria, and M. Ernzerhof, Hybrid functionals based on a screened Coulomb potential, The Journal of Chemical Physics **118**, 8207 (2003).

[199] L. H. Thomas, The calculation of atomic fields, Math. Proc. Camb. Philos. Soc.

23, 542 (1927).

[200] G. Kresse and J. Furthmüller, Efficiency of ab-initio total energy calculations for metals and semiconductors using a plane-wave basis set, Comput. Mater. Sci. **6**, 15 (1996).

[201] A. Hjorth Larsen et al., The atomic simulation environment—a Python library for working with atoms, Journal of Physics: Condensed Matter **29**, 273002 (2017).

[202] K. Momma and F. Izumi, VESTA 3 for three-dimensional visualization of crystal, volumetric and morphology data, J. Appl. Cryst. **44**, 1272 (2011).

[203] V. Wang, N. Xu, J.-C. Liu, G. Tang, and W.-T. Geng, VASPKIT: A user-friendly interface facilitating high-throughput computing and analysis using VASP code, Comput. Phys. Commun. **267**, 108033 (2021).

[204] M. Inaba, A. Zana, J. Quinson, F. Bizzotto, C. Dosche, A. Dworzak, M. Oezaslan, S. B. Simonsen, L. T. Kuhn, and M. Arenz, The Oxygen Reduction Reaction on Pt: Why Particle Size and Interparticle Distance Matter, ACS Catal. **11**, 7144 (2021).

[205] J. Huang, A. Malek, J. Zhang, and M. H. Eikerling, Non-monotonic Surface Charging Behavior of Platinum: A Paradigm Change, J. Phys. Chem. C **120**, 25 (2016).

[206] X. Zhu, J. Huang, and M. Eikerling, Electrochemical CO2 Reduction at Silver from a Local Perspective, ACS Catal. **11**, 14521 (2021).

[207] J. Huang, Y. Zhang, M. Li, A. Groß, and S. Sakong, Comparing Ab Initio Molecular Dynamics and a Semiclassical Grand Canonical Scheme for the Electric Double Layer of the Pt(111)/Water Interface, J. Phys. Chem. Lett. **14**, 2354 (2023).

[208] K. J. Taylor, C. L. Pettiette-Hall, O. Cheshnovsky, and R. E. Smalley, Ultraviolet photoelectron spectra of coinage metal clusters, J. Chem. Phys. **96**, 4 (1992).

[209] E. Kalered, N. Brenning, I. Pilch, L. Caillault, T. Minéa, and L. Ojamäe, On the work function and the charging of small (r≤ 5 nm) nanoparticles in plasmas, Phys. Plasmas **24**, 013702 (2017).

[210] T. Markovich, D. Andelman, and R. Podgornik, *Charged Membranes: Poisson–Boltzmann Theory, The DLVO Paradigm, and Beyond*, in *Handbook of Lipid Membranes* (CRC Press, 2021).

[211] J. O. Bockris and A. K. N. Ready, *Modern Electrochemistry*, Vol. Vol. 2 (Plenum Publishing Corporation, New York, 1973).

[212] J. K. Nørskov, T. Bligaard, A. Logadottir, J. R. Kitchin, J. G. Chen, S. Pandelov, and U. Stimming, Trends in the Exchange Current for Hydrogen Evolution, Journal of The Electrochemical Society **152**, 3 (2005).

[213] V. S. Fomenko and G. V. Samsonov, *Handbook of Thermionic Properties* (Springer New York, NY, 1966).

[214] B. Hammer and J. K. Nørskov, *Theoretical Surface Science and Catalysis—Calculations and Concepts*, in *Advances in Catalysis*, Vol. 45 (Academic Press, 2000), pp. 71–129.

9. List of publications

Journal articles

10 **Zhang, Y.**, Binninger, T., Huang, J., & Eikerling, M. (2026). Effective Ion Concentration as a Descriptor for the Local Reaction Environment at Nanoparticle-Based Electrocatalysts, *ACS Catalysis*, 16, 4, 3175–3187.
DOI: 10.1021/acscatal.5c06754

9 **Zhang, Y.**, Binninger, T., Huang, J., & Eikerling, M. (2025). Theory of Electro-Ionic Perturbations at Supported Electrocatalyst Nanoparticles, *Physical Review Letters*, *134*, 066201.
DOI: 10.1103/PhysRevLett.134.066201

8 **Zhang, Y.**, Agravante, G., Kadyk, T., & Eikerling, M. (2023). Modeling Water Phenomena in the Cathode Side of Polymer Electrolyte Fuel Cells. *Electrochimica Acta*, *452*, 142228.
DOI: 10.1016/j.electacta.2023.142228

7 **Zhang, Y.**, Kadyk, T., & Eikerling, M. (2023). Droplet Evolution from a Single Hydrophobic Pore in the Diffusion Media of Polymer Electrolyte Fuel Cells: A Conceptual Analysis. *The Journal of Electrochemistry Society*, *170*, 054501.
DOI: 10.1149/1945-7111/accfc2

6 Huang, J., **Zhang, Y.**, Li, M., Groß, A., & Sakong S. (2023). Comparing Ab Initio Molecular Dynamics and a Semiclassical Grand Canonical Scheme for the Electric Double Layer of the Pt(111)/Water Interface. *The Journal of Physical Chemistry Letters, 14*, 2354–2363.
DOI: 10.1021/acs.jpclett.2c03892

5 Huang, J., & **Zhang, Y.** (2022) Essays on Conceptual Electrochemistry: I. Bridging Open-Circuit Voltage of Electrochemical Cells and Charge Distribution at Electrode–Electrolyte Interfaces. *Frontiers in* Chemistry, 10, 938064.
DOI: 10.3389/fchem.2022.938064

4 **Zhang, Y.**, Huang, J., & Eikerling, M. (2021). Criterion for finding the optimal electrocatalyst at any overpotential. *Electrochimica Acta*, *400*, 139413.
DOI: 10.1016/j.electacta.2021.139413

3 **Zhang, Y**., Ye, T., Chen, M., Goodwin, Z. A., Feng, G., Huang, J., & Kornyshev, A. A. (2020). Enforced Freedom: Electric - Field - Induced Declustering of Ionic -

Liquid Ions in the Electrical Double Layer. *Energy & Environmental Materials*, *3*(3), 414-420.
DOI: 10.1002/eem2.12107

2 **Zhang, Y.**, Zhang, J., & Huang, J. (2019). Potential-dependent volcano plot for oxygen reduction: mathematical origin and implications for catalyst design. *The Journal of Physical Chemistry Letters*, *10*(22), 7037-7043.
DOI: 10.1021/acs.jpclett.9b02436

1 **Zhang, Y.**, & Huang, J. (2018). Treatment of ion-size asymmetry in lattice-gas models for electrical double layer. *The Journal of Physical Chemistry C*, *122*(50), 28652-28664.
DOI: 10.1021/acs.jpcc.8b08298

Manuscripts in preparation

1 **Zhang, Y.**, Lu, Y., Dunin-Borkowski, R., Eikerling, M., & Binninger, T. (2026). Metal–Metal Contact Electrification at the Nanoscale, *in preparation.*

Conference talks

8 **Zhang, Y.**, Lu, Y., Dunin-Borkowski, R., Eikerling, M., & Binninger, T., Metal–Metal Contact Electrification at the Nanoscale, DPG Spring Meeting, Dresden, Germany (March 2026).

7 **Zhang, Y.**, Binninger, T., Huang, J., & Eikerling, M., Theory Unravels Electro-Ionic Metal–Support Interactions at Supported Electrocatalyst Nanoparticles, 76th Annual Meeting of the International Society of Electrochemistry, Mainz, Germany (September 2025).

6 **Zhang, Y.**, Binninger, T., Huang, J., & Eikerling, M., Tango in Catalysis: Spontaneous Electrification between Metal Particle and Support, HITEC Communication Award Competition in Research Center Juelich, Juelich, Germany (August 2023).

5 **Zhang, Y.**, Agranvante, G., Kadyk, T., & Eikerling, M., Modelling Liquid Water Accumulation in the Cathode of Polymer Electrolyte Fuel Cells, European Fuel Cell Forum 2023, Luzern, Switzerland (July 2023).

4 **Zhang, Y.**, Huang, J., & Eikerling, M., Criterion for Finding the Optimal Electrocatalyst at Any Overpotential, Electrochemistry 2022, Berlin, Germany

(September 2022).

3 **Zhang, Y.**, Agranvante, G., Kadyk, T., & Eikerling, M., Modelling Liquid Water Accumulation in the Cathode of Polymer Electrolyte Fuel Cells, 32nd topical meeting of International Society of Electrochemistry, Stockholm, Sweden (June 2022).

2 **Zhang, Y.**, Agranvante, G., Kadyk, T., & Eikerling, M., Modelling Liquid Water Accumulation in the Cathode of Polymer Electrolyte Fuel Cells, 31st topical meeting of International Society of Electrochemistry, Aachen, Germany (May 2022).

1 **Zhang, Y.**, Huang, J., & Zhang, J., Potential Dependence of Volcano Plot of Oxygen Reduction Reaction: Mathematical Origin and Implications for Catalyst Design, 1st World Fuel Cell Conference, Shanghai, China (August 2019).

Conference Posters

4 **Zhang, Y.**, Binninger, T., Huang, J., & Eikerling, M., Density–Potential Functional Theory Unveils Electronic and Ionic Perturbations at Electrocatalyst Nanoparticles Induced by Support Materials, CECAM Workshop in Atomistic Modelling of Solid-Liquid Interfaces in Electrocatalysis, Leiden, the Netherlands (January 2024).

3 **Zhang, Y.**, Binninger, T., Huang, J., & Eikerling, M., Electronic Interactions and Double-Layer Charging for Supported Catalyst Nanoparticles Disentangled by Density Potential Functional Theory, 74th Annual Meeting of the International Society of Electrochemistry, Lyon, France (September 2023).

2 **Zhang, Y.**, Huang, J., & Eikerling, M., Criterion for Finding the Optimal Electrocatalyst at Any Overpotential, Annual Meeting of International Society of Electrochemistry, Lyon, France (September 2023).

1 **Zhang, Y.**, Agranvante, G., Kadyk, T., & Eikerling, M., Modelling Liquid Water Accumulation in the Cathode of Polymer Electrolyte Fuel Cells, Symposium on Modeling and Experimental Validation of Electrochemical Energy Technologies, Germany (March 2022).

Awards

3 **Lindau Alumnus (2025)**
Invited to attend the prestigious **74th Lindau Nobel Laureate Meeting in**

Chemistry, held in Lindau, Germany, as one of the 600 selected early-career researchers worldwide.

2 **Umbrella Award (2025)**
Awarded by the Umbrella Alliance (RWTH Aachen, Technion – Israel Institute of Technology, and Juelich Research Center) for outstanding research contributions in **Advancing Energy Materials and Systems.** The award includes €5,000 to support international collaborative visits.

1 **ISE Student Fellowship (2025)**
Awarded by the International Society of Electrochemistry (ISE) Division 7 (Physical Electrochemistry) for an outstanding contribution submitted to the 76th ISE Annual Meeting in Mainz. One of 10 recipients selected. The fellowship includes a full waiver of the conference registration fee.

Band / Volume 685
Performance and stability of solar cells and modules: From laboratory characterization to field data analysis
T. S. Vaas (2025), xvii, 146 pp
ISBN: 978-3-95806-871-1

Band / Volume 686
From Soil Legacy to Wheat Yield Decline: Studying the Plant-Soil Feedback Mechanisms in Wheat Rotations
N. Kaloterakis (2025), XXIX, 188 pp
ISBN: 978-3-95806-874-2

Band / Volume 687
Entwicklung von Beschichtungsverfahren für die Herstellung von Wärmedämmschichten auf additiv gefertigten Komponenten
M. Rüßmann (2026), ix, 188 pp
ISBN: 978-3-95806-877-3

Band / Volume 688
Model Perovskite Oxide Electrocatalysts for the Oxygen Evolution Reaction and their Material Sustainability Evaluation
L. Heymann (2026), vi, 174 pp
ISBN: 978-3-95806-878-0

Band / Volume 689
Development of an oxygen ion conducting solid oxide electrolysis cell based on gadolinium-doped cerium oxide as fuel electrode and electrolyte material
D. Ramler (2026), ix, 162 pp
ISBN: 978-3-95806-879-7

Band / Volume 690
Design of Local Multi-Energy Systems: Impact of Coupled Energy Vector Integration and Grid Service Participation
P. S. Glücker (2026), xxviii, 145 pp
ISBN: 978-3-95806-880-3

Band / Volume 691
A Parallel-in-Space Simulator for Accelerating Power System Simulation on Graphics Processing Units
J. Zhang (2026), 112 pp
ISBN: 978-3-95806-882-7

Band / Volume 692
Entwicklung von Reparaturmethoden für einkristalline Bauteile mittels thermischer Spritzverfahren
M. L. Létang (2026), X, 211 pp
ISBN: 978-3-95806-883-4

Band / Volume 693
Assessing the Environmental Implications of Offshore Wind Energy Advancements on the Future German Electricity Sector
A. Benitez (2026), xi, 176 pp
ISBN: 978-3-95806-885-8

Band / Volume 694
Entwicklung von Korrosionsschutzschichten für Protonen-Austausch-Membran-Wasserelektrolyseure
T. Sievert (2026), 201 pp
ISBN: 978-3-95806-888-9

Band / Volume 695
Hierarchical Modeling of Electrocatalytic Reactions from a Local Perspective
X. Zhu (2026), ix, 121 pp
ISBN: 978-3-95806-889-6

Band / Volume 696
Nanocrystalline Silicon Carbide in Transparent Passivating Contact Solar Cells
A. Eberst (2026), xiii, 225 pp
ISBN: 978-3-95806-891-9

Band / Volume 697
Theory of Electronic and Ionic Perturbations at Supported Electrocatalyst Nanoparticles
Y. Zhang (2026), XI, 131 pp
ISBN: 978-3-95806-896-4

Weitere ***Schriften des Verlags im Forschungszentrum Jülich*** unter
http://wwwzb1.fz-juelich.de/verlagextern1/index.asp

Energie & Umwelt / Energy & Environment
Band / Volume 697
ISBN 978-3-95806-896-4

Mitglied der Helmholtz-Gemeinschaft

JÜLICH
Forschungszentrum